TAL TECH

DOCTORAL THESIS

# Desulphurization by Catalytic Oxidation using Functionalized UiO-66-based Metal Organic Frameworks

Bijan Barghi

TALLINNA TEHNIKAÜLIKOOL
TALLINN UNIVERSITY OF TECHNOLOGY
TALLINN 2026

TALLINN UNIVERSITY OF TECHNOLOGY
DOCTORAL THESIS
85/2026

# Desulphurization by Catalytic Oxidation using Functionalized UiO-66-based Metal Organic Frameworks

BIJAN BARGHI

TAL TECH PRESS

TALLINN UNIVERSITY OF TECHNOLOGY
School of Engineering
Department of Materials and Environmental Technology
This dissertation was accepted for the defence of the degree 16/11/2026

**Supervisor**: Professor Allan Niidu
School of Engineering
Tallinn University of Technology
Tallinn, Estonia

**Opponents**: Associate Professor Ken-ichi Otake
Institute for Integrated Cell-Material Sciences
Kyoto University
Kyoto, Japan

Associate Professor Rasmus Palm
Institute of Chemistry
University of Tartu
Tartu, Estonia

**Defence of the thesis**: 16/12/2026, Kohtla-Järve

**Declaration:**
Hereby I declare that this doctoral thesis, my original investigation and achievement, submitted for the doctoral degree at Tallinn University of Technology has not been submitted for doctoral or equivalent academic degree.

Bijan Barghi

---
signature




Copyright: Bijan Barghi, 2026
ISSN 2585-6898 (paperback)
ISBN 978-9916-80-603-6 (paperback)
ISSN 2585-6901 (PDF)
ISBN 978-9916-80-604-3 (PDF)
https://doi.org/10.23658/taltech.85/2026

Barghi, B. (2026). *Desulphurization by Catalytic Oxidation using Functionalized UiO-66-based Metal Organic Frameworks* [TalTech Press]. https://doi.org/10.23658/taltech.85/2026

TALLINNA TEHNIKAÜLIKOOL
DOKTORITÖÖ
85/2026

# Katalüütiline oksüdatiivne väävli eemaldamine kasutades funktsionaliseeritud UiO-66 põhiseid metallorgaanilisi võrestruktuure

BIJAN BARGHI

TAL TECH
KIRJASTUS

# Contents

Contents ..... 5
List of Publications ..... 7
Author's Contribution to the Publications ..... 8
Introduction ..... 9
Abbreviations ..... 11
Terms ..... 12
1 Literature Review ..... 13
1.1 Hydrodesulphurization ..... 13
1.2 Oxidative Desulphurization ..... 14
1.3 Metal Organic Frameworks ..... 15
1.4 Kinetic Study ..... 18
1.5 Response Surface Methodology and Optimization ..... 18
1.6 Photo Oxidative Desulphurization ..... 24
2 Experimental ..... 25
2.1 Materials and Methods ..... 25
2.1.1 Synthesis of Pristine UiO-66 ..... 25
2.1.2 Synthesis of metal- modified UiO-66 derivatives ..... 26
2.1.3 Synthesis of impregnated Metal Doped UiO-66 ..... 27
2.2 Catalyst Tests ..... 27
2.3 Characterization Methods ..... 30
2.4 Design of Experiments ..... 31
2.5 Kinetic Study ..... 32
3 Results and Discussion ..... 33
3.1 Characterization ..... 33
3.1.1 XRD ..... 33
3.1.2 FTIR ..... 34
3.1.3 SEM ..... 37
3.1.4 NMR ..... 39
3.1.5 TGA ..... 40
3.1.6 XPS ..... 41
3.1.7 Nitrogen Adsorption–Desorption Analysis ..... 42
3.2 Effect of Parameters ..... 44
3.3 Parameters Optimization ..... 46
3.4 Kinetic Modeling ..... 47
3.5 Parameters Effects on PODS ..... 48
4 Conclusions ..... 52
List of Figures ..... 53
List of Tables ..... 55
References ..... 56
Acknowledgements ..... 66
Abstract ..... 67
Lühikokkuvõte ..... 69

Appendix ..... 71
Curriculum vitae ..... 109
Elulookirjeldus ..... 110

## List of Publications

The list of author's publications, based on which the thesis has been prepared:

I Barghi, Bijan, Martin Jürisoo, Maria Volokhova, Liis Seinberg, Indrek Reile, Valdek Mikli, and Allan Niidu. "Process optimization for catalytic oxidation of dibenzothiophene over UiO-66-$NH_2$ by using a response surface methodology." ACS omega 7, no. 19 (2022): 16288-16297.

II Barghi, Bijan, Tanel Mõistlik, Anastassia Raag, Maria Volokhova, Indrek Reile, Liis Seinberg, Valdek Mikli, and Allan Niidu. "Deep Oxidative Desulphurization of Planar Compounds Over Functionalized Metal–Organic Framework UiO-66 (Zr): An Optimization Study." ACS omega 9, no. 22 (2024): 23329-23338.

III Barghi, Bijan, Tanel Mõistlik, Deniss Panov, Anastassia Raag, Oliver Järvik, and Allan Niidu. "Kinetic Modelling of Deep Oxidative Desulphurization over Functionalized UiO-66 from a model fuel using Complex Reaction Theory." ACS omega 10, no. 16 (2025): 15947–15958.

## Author's Contribution to the Publications

Contribution to the papers included in this thesis are:

I Conducted the experiments, analysed and interpreted the data, performed the majority of the measurements, and contributed to writing the article.

II Conducted the experiments, analysed and interpreted the data, performed the majority of the measurements, and contributed to writing the article.

III Conducted the experiments, analysed and interpreted the data, performed the majority of the measurements, and contributed to writing the article.

# Introduction

Deep desulphurization is a prominent process for producing ultra-clean sulphur-free fuel for which hydrodesulphurization (HDS) is widely used. However, a significant limitation of this method is the removal of aromatic sulphur-containing compounds. It requires large reactors and highly active catalysts with severe conditions, including high temperatures (300-400 °C) and hydrogen pressure (30-120 bar) [1]. Oxidative Desulphurization (ODS) is a practical approach for removing aromatic sulphur compounds, compared with HDS reaction, it can be conducted under mild operating conditions. The ODS process includes oxidation and extraction steps for sulphur compounds [2].

Metal Organic Frameworks (MOFs) are good candidates as catalysts and adsorbents for ODS reactions, as they contain structurally rigid inorganic secondary building units (SBUs) and flexible, tuneable organic linkers [3]. The porous zirconium terephthalate UiO-66 contributes significantly to both scientific and industrial applications because of its high surface area and exceptional chemical, thermal, and mechanical stability [4-8]. The oxidation of sulphur compounds was carried out using hydrogen peroxide as the oxidant.

In this study, pristine UiO-66(Zr), linker-functionalized UiO-66 derivatives (UiO-66-$NH_2$, UiO-66-OH, and UiO-66-$NO_2$), and metal-modified UiO-66 materials (M–UiO-66, where M denotes the introduced metal) were synthesized by solvothermal methods. Solvothermal synthesis is a procedure in which a solution containing reagents is heated at elevated temperature in an autoclave. It is similar to hydrothermal synthesis but uses non-aqueous solvents instead of water. The characterization of samples was carried out by different techniques, including $^1$H nuclear magnetic resonance ($^1$H NMR) spectroscopy, thermogravimetric analysis (TGA), Fourier transform infrared spectroscopy (FTIR), scanning electron microscope (SEM), microwave plasma atomic emission spectrometers (MP-AES), nitrogen adsorption – desorption analysis (BET) and X-ray diffraction (XRD).

In the first step, this study aims to determine the catalytic activity and stability of ligand-modified UiO-66 with different functional groups (–$NH_2$, –$NO_2$, –OH) in the deep oxidative desulphurization of a model fuel. The heteroaromatic sulphur compounds included in this study were dibenzothiophene (DBT), 2-methylbenzothiazole (2-MB) and 4,6-dimethyldibenzothiophene (4,6-DMDBT) at 1000 ppm level in n-dodecane as the fuel phase. DBT, 2-MB, and 4,6-DMDBT were selected as model sulphur compounds because they were identified among the dominant sulphur-containing constituents of the shale-oil cut considered in this study. Their selection also provides chemically and structurally distinct substrates for evaluating catalytic oxidative desulphurization. n-Dodecane was employed as the fuel phase, as it is a widely accepted surrogate fuel in desulphurisation studies, enabling controlled and reproducible experimental conditions. The reaction conditions and the performance of UiO-66 derivates in oxidative sulphur removal were systematically investigated. To understand the importance of process parameters – reaction temperature, oxidant amount, and catalyst dosage – a quadratic statistical model was developed from which optimal conditions were derived by employing the response surface methodology (RSM) [9]. RSM and Analysis of Variance (ANOVA) were used to evaluate the individual process factors, their interactions, and sulphur-removal responses. The results showed that the extent of oxidation of the aromatic compounds declined following the sequence DBT > 2-MB >> 4,6-DMDBT for all the MOFs. The prominent parameters in the desulphurization process are the electron density on the sulphur atom and the steric hindrance surrounding the sulphur atoms; oxidative

desulphurization generally benefits from greater electron density and lower steric hindrance. Because the electron density on the sulphur atoms of 4,6-dimethyldibenzothiophene and dibenzothiophene is comparable, steric hindrance surrounding the sulphur atom plays a major role in the oxidation. As a result, dibenzothiophene indicated higher conversion over UiO-66 derivatives because there was less steric hindrance around the sulphur atom among the investigated aromatic compounds. This behaviour (electron density vs. steric hindrance) is consistent with prior ODS reactivity discussions for refractory sulphur compounds. Previously, a range of diverse catalysts have been identified for ODS reactions, with limited studies involving functionalized UiO-66. To the best of our knowledge, process-condition optimization across multiple functionalized UiO-66 materials in ODS has not been systematically reported. The findings revealed that at 66.7 °C, 3.0 (mg/mg) of oxidative agent over sulphur and 9.7 (mg/mg) of MOF over sulphur (by weight) achieved the highest removal efficiencies of 98.7% DBT, 93.2% 2-MB, and 69.3% 4,6-DMDBT for UiO-66-$NO_2$ as the catalyst in the model fuel. It was also observed that UiO-66-$NO_2$ had a higher efficiency in deep oxidative desulphurization compared with the other UiO-66 based catalysts used in the current study. UiO-66-$NO_2$ exhibited higher catalytic activity in deep oxidative desulphurization due to the more electron-accepting group in its ligand structure.

Under optimal conditions, UiO-66-$NO_2$ showed acceptable catalytic activity and reusability after four runs, although a gradual loss of activity was observed. The sulphur-removal efficiencies over four consecutive runs indicate that the initial performance was largely retained, with an overall decrease of nearly 10.8%, dropping from 98.7 to 93.3%, 88.0% to 82.1%, and 69.3 to 61.0% for DBT, 2-MB, and 4,6-DMDBT, respectively. Another aim of this study is to create a systematic and straightforward approach for determining basic reaction routes and overall reactions using the theory of complex kinetics for an oxidative desulphurization (ODS) reaction, using solvothermally synthesized metal–organic framework (MOF), UiO-66-$NO_2$ as a catalyst to remove the dibenzothiophene (DBT) from a model fuel at temperatures in the range of 20 - 100 °C. The intermediates are organized in a "matrix of intermediates", which simplifies the combination of elementary reactions to form Overall Reactions. Adsorption, oxidation, and desorption were considered in eleven basic reaction steps that comprised the proposed ODS mechanism. The model's kinetic parameters were optimized using a MATLAB program and described by the reparametrized Arrhenius equation. Markov chain Monte Carlo (MCMC) modelling was also used to investigate the dependability of the estimated parameters and model predictions. The experimental results were in satisfactorily agreement with the model predictions, as Complex Reaction theory was utilized for the first time to investigate the ODS reaction over MOFs.

As the next step, Photocatalytic Oxidation Desulphurization (PODS) was considered for the removal of heterocyclic sulphur compounds from a model fuel at mild temperatures, using air under UV-LED irradiation instead of organic or inorganic oxidants. Metal-doped UiO-66 derivatives (Co, Mn, Cu, Fe, Ti, Ce) were employed for PODS reactions, and it was shown that these modified frameworks can achieve high oxidative sulphur conversion within short reaction times. Metal dopants were introduced during the synthesis of the pristine UiO-66 via a solvothermal route. Among the screened metals, Co-UiO-66 and Ti-UiO-66 demonstrated the highest DBT removal efficiencies of 81% and 88%, respectively, compared to the remaining metal-doped variants Mn-UiO-66, Cu-UiO-66, Fe-UiO-66, and Ce-UiO-66 exhibited less DBT conversions.

## Abbreviations

| | |
|---|---|
| 2-MB | 2-methylbenzothiazole |
| 4,6-DMDBT | 4,6-dimethyldibenzothiophene |
| ANOVA | Analysis of Variance |
| BDC | benzene-1,4-dicarboxylic acid (terephthalic acid) |
| BET | Brunauer–Emmett–Teller specific surface area (from $N_2$ adsorption–desorption data) |
| Cat./Sul. (C/S) | catalyst-to-sulphur ratio |
| CCD | Central Composite Design |
| DBT | dibenzothiophene |
| DBTSO | dibenzothiophene sulfoxide |
| $DBTSO_2$ | dibenzothiophene sulfone |
| FTIR | Fourier-transform infrared spectroscopy |
| $^1H$ NMR | Proton Nuclear Magnetic Resonance spectroscopy |
| HDS | hydrodesulphurization |
| LOF | Lack of Fit |
| LED | light-emitting diode |
| MCMC | Markov chain Monte Carlo |
| MOF | Metal Organic Frameworks |
| MPAES | Microwave plasma atomic emission spectrometry/spectroscopy |
| ODE | Ordinary Differential Equation |
| ODS | Oxidative Desulphurization |
| OR | Overall Reaction |
| Oxd./Sul. (O/S) | oxidant-to-sulphur ratio |
| PODS | Photocatalytic oxidation desulphurization |
| RR | Reaction Route |
| RSM | Response Surface Methodology |
| SBU | Secondary Building Units |
| SEM | Scanning electron microscope |
| TGA | Thermogravimetric analysis |
| UiO-66 | Zr-based MOF; “UiO” refers to the University of Oslo |
| UV | Ultraviolet |
| XRD | X-ray diffraction |

## Terms

| | |
|---|---|
| $X_i$ | coded values of CCD variables |
| $\beta_i, \beta_{ij}$ | CCD coefficients |
| α | axial point in CCD |
| $\varepsilon$ | experimental error |
| $x_i$ | dimensionless coded variable |
| $\Delta X_i$ | change in the actual variable corresponding to one coded unit |
| $N$ | total number of experiments |
| $k$ | independent continuous variables |
| $n_0$ | number of replicated centre-point experiments |
| $\hat{\beta}$ | estimated regression coefficients |
| $e_i$ | difference between an experimentally observed response and the corresponding model-predicted response |
| $SS$ | sum of squares |
| $MS$ | mean square |
| $df$ | degrees of freedom |

# 1 Literature Review

## 1.1 Hydrodesulphurization

One of the primary sources of air pollution is sulphur oxide ($SO_x$) emissions into the atmosphere from the combustion of fossil fuels, which leads to environmental and health problems; therefore, improving deep desulphurisation process is essential for producing ultra-clean sulphur-free fuel [1-3,10].

Hydrodesulphurisation (HDS) is a catalytic chemical process widely employed in the petroleum industry to remove sulphur from fossil fuels. The process involves the reaction of organic sulphur compounds with hydrogen at elevated temperatures and pressures in the presence of a catalyst, typically consisting of cobalt and molybdenum supported on alumina. During HDS, sulphur is converted to hydrogen sulphide ($H_2S$), which is subsequently removed from the treated product. The HDS reaction typically occurs in fixed-bed reactors at temperatures ranging from 300 to 400 °C and pressures between 30 and 130 atmospheres [11].

The effectiveness of HDS varies depending on the type of sulphur compounds present in the feedstock. Aliphatic sulphur compounds, such as thiols, are highly reactive and can be removed completely. However, aromatic sulphur compounds, particularly those containing thiophene rings, pose a greater challenge due to their resonance stabilization. Two primary pathways for desulphurisation are recognized: direct desulphurisation (hydrogenolysis) and hydrogenation followed by hydrogenolysis. For more refractory compounds such as dibenzothiophenes, the hydrogenation route (which involves saturation of aromatic rings prior to sulphur removal) is required. [12-13]. Despite its widespread use in the petroleum industry, hydrodesulphurisation, presents several significant challenges that limit its efficiency in producing ultra-low sulphur fuels. The process is characterized by high hydrogen consumption, particularly when treating heavier feedstocks or aiming for deep desulphurization, which contributes to increased operational costs and resource intensity. The severe operating conditions required for effective HDS, including elevated temperatures and pressures, result in substantial energy requirements and further escalate operational expenses. Moreover, HDS catalysts are prone to deactivation through poisoning by nitrogen compounds and coking, necessitating frequent regeneration or replacement, which affects process continuity and economics. A critical limitation of HDS is its incomplete removal of refractory compounds, especially sterically hindered sulphur species such as 4,6-dimethyldibenzothiophene, which poses a significant challenge in achieving ultra-low sulphur levels mandated by stringent environmental regulations. The process also suffers from limited selectivity, potentially leading to undesired side reactions such as olefin hydrogenation, which can adversely affect fuel properties. Additionally, the generation of hydrogen sulphide ($H_2S$) as a by-product necessitates careful management and conversion to elemental sulphur, typically through the Claus process, adding complexity and environmental considerations to the overall operation. These multifaceted limitations have spurred extensive research into alternative desulphurization technologies, including adsorptive and oxidative methods, which show promise in complementing or potentially replacing conventional HDS in specific applications, driving the industry towards more efficient and environmentally sustainable fuel-production processes [12-13].

## 1.2 Oxidative Desulphurization

Oxidative Desulphurization (ODS) has emerged as a promising alternative to conventional hydrodesulphurization for the removal of recalcitrant aromatic sulphur compounds from fossil fuels. This process offers several advantages over HDS, primarily due to its ability to operate under milder conditions, which translates to reduced energy requirements and operational costs [12-13]. The ODS process typically involves the oxidation of sulphur-containing compounds to their corresponding sulfoxides or sulfones, which can then be more easily separated from the fuel matrix due to their increased polarity. This approach is particularly effective for treating dibenzothiophene and its alkylated derivatives, which are known to be resistant to traditional HDS methods [14]. One of the key benefits of ODS is its potential to significantly reduce capital investments in equipment and hydrogen consumption. Unlike HDS, which requires high-pressure hydrogen and specialized reactors, ODS can be performed at near-ambient pressures and temperatures, with fewer modifications than HDS [15].

In addition to conventional ODS, several related strategies have been investigated. Photocatalytic oxidative desulphurization (PODS) uses light and a photocatalyst to promote oxidation of organosulphur compounds and can operate under comparatively mild conditions [16]. Oxidative–extractive desulphurization (OEDS) combines chemical oxidation with extraction into a selective polar phase, thereby facilitating removal of the more polar sulfoxide/sulfone products from the hydrocarbon phase [17]. These approaches are being developed to improve the efficiency, energy demand, and separability of deep-desulphurization processes.

Thiophene, benzothiophene, dibenzothiophene, and 4,6-dimethyldibenzothiophene are sulphur-containing heterocyclic compounds commonly found in fossil fuels such as crude oil and coal [18]. These compounds are of significant environmental concern due to their contribution to the sulphur oxide ($SO_x$) emissions during fuel combustion, which can lead to acid rain and other environmental issues. The removal of these sulphur compounds is critical for producing ultra-clean fuels that comply with stringent environmental regulations [19]. However, desulphurisation of these compounds is particularly challenging due to their chemical structure and stability. Thiophene, the simplest of these compounds, consists of a five-membered ring with one sulphur atom. Its aromatic nature, due to the delocalization of electrons across the ring, contributes to its stability and resistance to conventional desulphurisation techniques like hydrodesulphurisation [14]. Benzothiophene and dibenzothiophene are more complex structures with additional benzene rings fused to the thiophene ring, further enhancing their stability through increased resonance energy. This resonance stabilization makes breaking the C-S bond energetically demanding, thus requiring more severe conditions for desulphurization. The challenge is exacerbated in 4,6-dimethyldibenzothiophene due to the presence of methyl groups at positions 4 and 6, which introduce steric hindrance that inhibits access to the sulphur atom by catalytic active sites during desulphurisation (Figure 1). Both methyl groups can effectively shield the sulphur centre from desulphurization [18-19]. Traditional HDS processes are often inadequate for these refractory sulphur compounds because they rely on hydrogenation reactions that are less effective when faced with the aromatic stabilization and steric hindrance present in these molecules [20-21]. As a result, alternative desulphurization methods such as oxidative desulphurization (ODS) and adsorptive desulphurization (ADS) have been explored [13,21,22]. ODS involves the oxidation of sulphur compounds into more polar sulfoxides or sulfones, which can then be removed by extraction or adsorption. This

method benefits from milder operating conditions compared to HDS and can be enhanced by using catalysts that facilitate the oxidation process [13]. ADS focuses on selectively adsorbing sulphur compounds onto materials with high surface areas and specific affinities for sulphur species. Despite these advancements, the development of efficient and cost-effective desulphurization technologies remains a significant challenge in the quest for cleaner fuels [21-22]. Oxidative Extractive Desulphurization (OEDS) is a two-step process for removing sulphur compounds from fuels comprising of an oxidation and an extraction step. In the oxidation step, sulphur compounds are converted to their corresponding sulfoxides or sulfones using an oxidizing agent. Subsequently, these oxidized species are extracted from the fuel matrix using a suitable polar solvent, exploiting their increased polarity compared to the original sulphur compounds [13-15]. Among various oxidizing agents, such as hydrogen peroxide, molecular oxygen, and tert-butyl hydroperoxide [23-25], hydrogen peroxide has demonstrated superior efficiency in ODS reactions [26-27]. This preference is attributed to its high active oxygen content, additionally environmental friendliness, and the formation of water as the only by-product are added benefits. A diverse array of catalysts has been investigated for ODS reactions, encompassing porous materials functionalized with titanium [28], metal oxides [29], boron nitride [30], reduced graphene oxide [15], activated carbon [31], zeolites [32], and metal-organic frameworks (MOFs) [33].

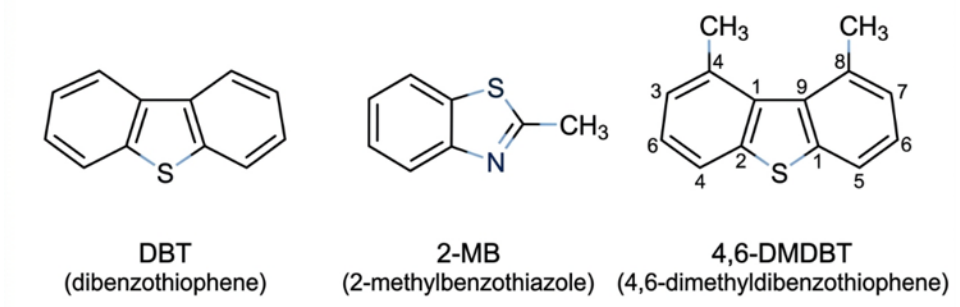



*Figure 1. Molecular structures of the model sulphur compounds employed in this study: dibenzothiophene (DBT), 2-methylbenzothiazole (2-MB), and 4,6-dimethyldibenzothiophene (4,6-DMDBT).*

## 1.3 Metal Organic Frameworks

MOFs have garnered significant attention due to their unique structural properties. These three-dimensional coordination polymers, composed of organic linkers and metal nodes, offer a combination of stability and flexibility [34-35]. MOFs provide opportunities for tailoring catalytic active sites for specific reactions [36-37]. Among the various MOF structures, the porous zirconium terephthalate UiO-66 has emerged as a prominent catalyst for ODS [33-34]. Its popularity stems from its large surface area, tunable porosity, exceptional stability, and reusability. Moreover, the modification of UiO-66(Zr), Figure 2, through the incorporation of functionalized terephthalic acid ligands has proven to be an effective strategy for altering its chemical and physical characteristics [38-40]. UiO-66 is conventionally constructed from hexanuclear metal clusters ($[Zr_6O_4(OH)_4]$) and 1,4-benzenedicarboxylate (BDC) linkers. Doping with transition metals often targets missing-linker defects or involve partial substitution of the $Zr^{4+}$ nodes, leading to changes in physical and chemical properties. These modifications can enhance the Lewis acidity of

the framework, rendering functionalized UiO-66 an attractive option for applications in adsorption, drug delivery, and heterogeneous catalysis [38-40]. Previous studies have demonstrated the efficacy of various MOFs as catalysts for ODS [3-5]. Notably, UiO-66 has been reported to achieve high sulphur removal efficiency within shorter process durations compared to other MOF catalysts [4-5]. The adsorption and oxidation efficiencies of pristine UiO-66 and its amino- and nitro-modified variants have been investigated in previous studies [7,97], providing a foundation for further research and optimization of ODS processes using these materials, as summarized in Table 1 (Publication II).

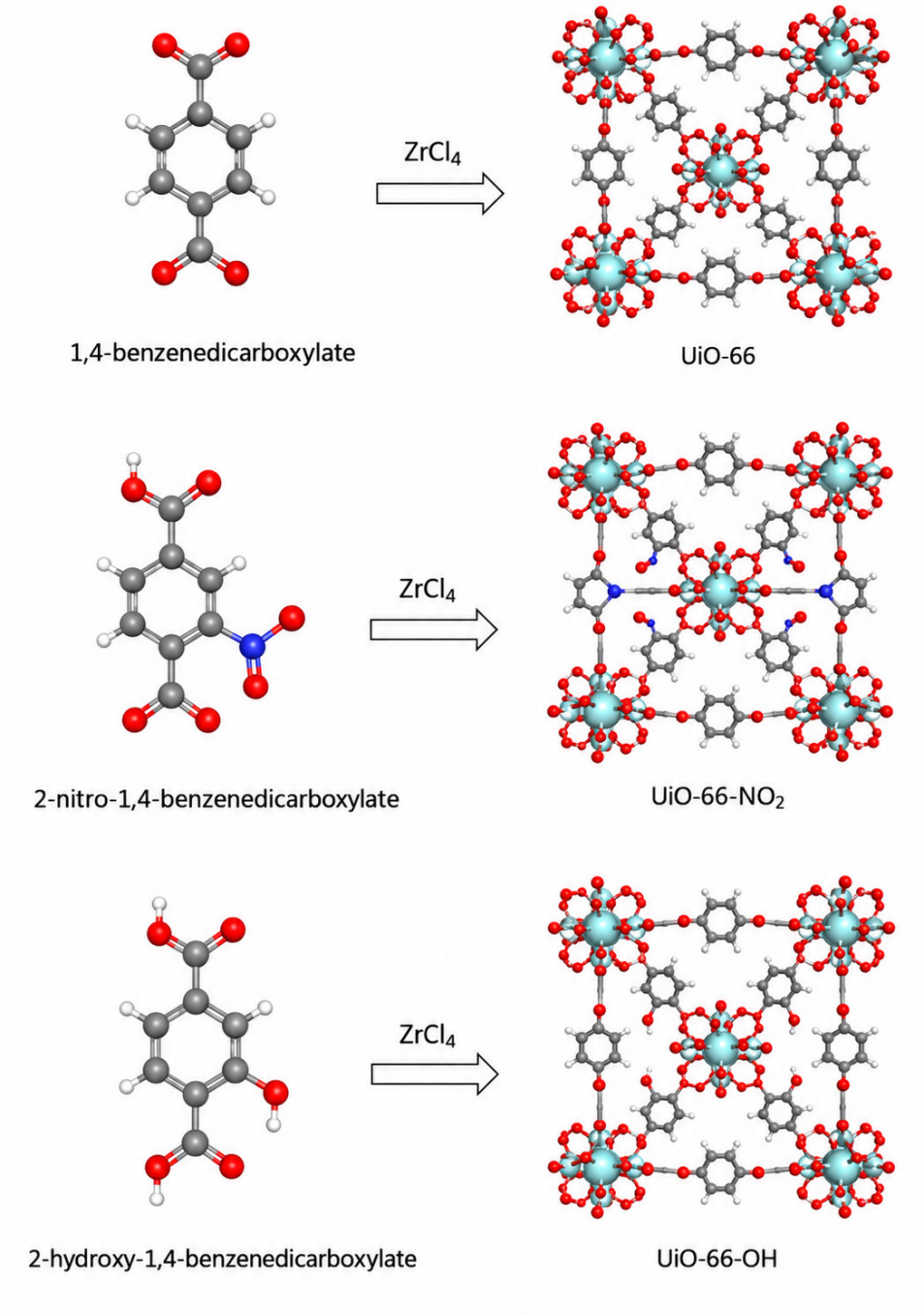



*Figure 2. Schematic showing BDC-based linker functionalization and the corresponding UiO-66 materials investigated in this work: UiO-66 (BDC), UiO-66-$NO_2$ ($NO_2$–BDC), and UiO-66-OH (OH–BDC). The molecular linker structures are chemically explicit; the framework drawing is schematic.*

## 1.4 Kinetic Study

Oxidative desulphurization (ODS) has emerged as a promising technique for fuel desulphurization, offering advantages over traditional methods [10,15]. While numerous studies have reported catalytic data on various catalysts for sulphur oxidation reactions, there is a significant gap in comprehensive kinetic studies [41-45]. Most existing kinetic models have relied on simplified first-order kinetics [45-48] or Langmuir-Hinshelwood and Eley-Rideal mechanisms [49], which may not fully capture the complexity of the ODS process.

The complex reaction methodology [50], employing reaction route networks, provides a more sophisticated approach to understanding ODS kinetics. This method utilizes an intermediate framework matrix to represent stoichiometric relationships between chemical species and elementary reactions [51-52], allowing for a more detailed analysis of multi-step reaction mechanisms. Unlike the concept of a single rate-determining step, which can oversimplify complex mechanisms [53], complex reaction theory considers the interplay between multiple elementary steps, each contributing to the overall reaction rate and product distribution in catalytic systems. Barghi and Karimzadeh [51] exemplified this approach by developing a kinetic model for catalytic cracking of n-butane over HZSM-5, where the process involves parallel elementary reactions, multi-feed inputs, several reaction channels, and a diverse array of products. Their study demonstrated the interplay among primary/secondary cracking routes, monomolecular and bimolecular routes, and olefin/paraffin formation, as well as product desorption. By systematically analyzing these pathways, the authors reduced the complexity of numerous reaction routes to a set of significant overall reactions.

To address the challenges of modelling complex reaction networks, researchers have developed systematic approaches. The theory of stoichiometric numbers for elementary reactions, proposed by Horiuti and Nakamura [54], and the subsequent theory of complex reactions have facilitated the development of kinetic models for multiple mechanisms, particularly on catalyst surfaces. These approaches provide efficient algorithms for estimating rates of complex multistep reactions, acknowledging that a singular rate-limiting step may be absent in such systems [55].

The Markov Chain Monte Carlo (MCMC) method has been employed to model reaction kinetics and estimate parameters, offering a comprehensive picture of parameter uncertainties and dependencies. This Bayesian inference approach is particularly useful for chemical kinetics models described by systems of differential equations representing reaction rates and species concentrations. MCMC has been successfully applied to various kinetic studies, including cell culture processes [56], isobutane dehydrogenation [57], catalytic oxidation [58], and lactose hydrogenation over ruthenium catalysts [59].

## 1.5 Response Surface Methodology and Optimization

Response Surface Methodology (RSM) is a collection of statistical and mathematical techniques for modelling and optimizing responses influenced by several independent variables. Rather than varying one factor at a time, RSM uses a structured design of experiments to estimate simultaneous main effects, interactions between variables, and curvature of the response surface while limiting the total number of experimental runs

[9,60–64]. This feature is particularly advantageous in chemical and catalytic systems, where several operating variables can influence the response simultaneously and the effect of one factor may depend on the level of another factor.

For a response y governed by k independent coded variables $x_i$, a second-order polynomial model is commonly expressed as:

$$y = \beta_0 + \sum_{i=1}^{k} \beta_i x_i + \sum_{i=1}^{k} \beta_{ii} x_i^2 + \sum_{i<j} \beta_{ij} x_i x_j + \varepsilon \quad (1)$$

where $\beta_0$ is the intercept, $\beta_i$ represents the linear coefficients, $\beta_{ii}$ represents the quadratic coefficients, $\beta_{ij}$ represents the interaction coefficients, and $\varepsilon$ accounts for experimental error and other unexplained variation. The corresponding predicted response, $y$, is obtained from the fitted model without the random error term. The linear coefficients describe the direction and magnitude of the individual effects of the factors, whereas the quadratic coefficients describe curvature in the response surface. Interaction coefficients are particularly important because they indicate whether the influence of one process variable depends on the level of another variable [9,64].

Because experimental factors may have different units and numerical ranges, the actual value of each factor, $X_i$, is transformed into a dimensionless coded variable:

$$x_i = \frac{X_i - X_{0,i}}{\Delta X_i} \quad (2)$$

where $X_{0,i}$ represents the value of factor $i$ at the centre of the experimental domain and $\Delta X_i$ is the change in the actual variable corresponding to one coded unit. Coding therefore allows factors such as temperature, oxidant-to-sulphur ratio, and catalyst-to-sulphur ratio to be represented on a comparable numerical scale. This also facilitates estimation and comparison of regression coefficients.

Central Composite Design (CCD) is particularly suitable for fitting second-order response surfaces. A CCD combines factorial points, axial or star points, and replicated centre points. The factorial points are primarily used to estimate linear and interaction effects, the axial points provide the additional information required to estimate quadratic curvature and replicated centre points provide an estimate of pure experimental error and support statistical evaluation of model lack of fit [62–64].

For k independent continuous variables, the total number of experiments in a complete CCD can be written as:

$$N = 2^k + 2k + n_0 \quad (3)$$

where $2^k$ represents the number of factorial experiments, $2k$ represents the number of axial experiments, and $n_0$ represents the number of replicated centre-point experiments. In the three-factor CCD applied in this thesis, eight factorial points and six axial points were combined with three centre-point experiments, resulting in a total of 17 experimental runs:

$$N = 2^3 + 2(3) + 3 = 17 \quad (4)$$

For a rotatable circumscribed CCD, the axial distance α is selected so that experimental points located at equal distances from the design centre have approximately equal prediction variance. For a three-factor design, this parameter is calculated as [64]:

$$\alpha = (2^k)^{1/4} = (2^3)^{1/4} = 1.682 \quad (5)$$

Consequently, the coded levels used in the experimental design are $-\alpha$, −1, 0, +1, and $+\alpha$. The corresponding actual factor levels are obtained by transformation from these coded values. This explains why some factor levels generated by a CCD are non-integer values rather than conventional rounded experimental values. After completion of the experimental runs, the coefficients of the polynomial model are commonly determined using the least-squares method. In matrix notation, the estimated regression coefficient vector can be expressed as:

$$\hat{\beta} = (\mathrm{X}^T\mathrm{X})^{-1}\mathrm{X}^T\mathrm{y} \quad (6)$$

where $\mathrm{X}$ is the experimental design matrix, $\mathrm{y}$ contains the measured responses, and $\hat{\beta}$ contains the estimated regression coefficients. Once the coefficients have been determined, a predicted response $\hat{y}_i$ can be calculated for each experimental condition. The difference between an experimentally observed response and the corresponding model-predicted response is termed the residual:

$$e_i = y_i - \hat{y}_i \quad (7)$$

Residual analysis is an important component of RSM because it evaluates whether the unexplained deviations between experimental and predicted values behave randomly. Ideally, residuals should be approximately normally distributed, have a mean close to zero, and show no systematic relationship with the predicted response, experimental run order, or individual process factors. A systematic residual pattern can indicate that an important model term has been omitted, that the variance is non-constant, or that the selected polynomial does not adequately represent the experimental system [64].

Analysis of Variance (ANOVA) is used to evaluate the statistical significance and adequacy of the fitted polynomial model. ANOVA partitions the total variation in the measured response into components associated with the regression model and with unexplained experimental error. The total sum of squares can be expressed as:

$$SS_{\mathrm{Total}} = SS_{\mathrm{Model}} + SS_{\mathrm{Error}} \quad (8)$$

where $SS_{\mathrm{Total}}$ represents the total variability of the experimental observations around their overall mean, $SS_{\mathrm{Model}}$ represents the variation explained by the fitted regression model, and $SS_{\mathrm{Error}}$ represents the unexplained variation remaining between experimental and predicted values. The sum of squares ($SS$) therefore provides a measure of the amount of response variation associated with each model term. A model term with a relatively large sum of squares explains a greater fraction of the observed response variation than a term with a very small sum of squares, although statistical significance also depends on the experimental error and the associated degrees of freedom.

The degrees of freedom ($df$) describe the number of independent pieces of information available for estimating a source of variation. The mean square associated with each source is calculated by dividing its sum of squares by the corresponding degrees of freedom:

$$MS = \frac{SS}{df} \tag{9}$$

The resulting mean square ($MS$) represents the variance attributed to that particular source. Mean squares are subsequently used to calculate the F-statistic. The F-value evaluates whether the variance explained by a model or individual model term is sufficiently large compared with the unexplained experimental variance. For the overall regression model, it can be expressed as:

$$F_{\text{Model}} = \frac{MS_{\text{Model}}}{MS_{\text{Error}}} \tag{10}$$

A relatively large F-value indicates that the variation explained by the model is large relative to random experimental error. However, the magnitude of the F-value must be considered together with its corresponding probability value rather than interpreted independently.

The p-value represents the probability of obtaining an effect at least as large as that observed if the corresponding model term actually had no statistically detectable effect. A small p-value therefore provides evidence against the null hypothesis. A commonly applied significance criterion is:

$$p < 0.05 \tag{11}$$

corresponding to a 95% confidence level. Thus, terms having $p$ < 0.05 are generally considered statistically significant, whereas terms with $p$ > 0.05 are not considered statistically significant at that confidence level. Nevertheless, statistical significance should always be interpreted together with chemical relevance, experimental uncertainty, and the hierarchical structure of the polynomial model [64].

For example, in the ANOVA of the dibenzothiophene oxidation model employed in this work, reaction temperature A gives an F-value of 20.16 and a p-value of 0.0028, indicating a statistically significant linear temperature effect. More importantly, the quadratic temperature term $A^2$ gives an F-value of 42.00 and a p-value of 0.0003, demonstrating strong curvature of the response with temperature. This observation illustrates why a quadratic RSM model is more appropriate than a simple linear model for describing the investigated process. In comparison, individual terms such as B, C, AC, and BC exhibit considerably larger p-values and therefore do not show statistically significant individual contributions at the 95% confidence level under the investigated conditions.

An additional and particularly important ANOVA parameter is the lack-of-fit (LOF) test. Residual error can be separated into lack-of-fit variation and pure experimental error:

$$SS_{\text{Error}} = SS_{\text{LOF}} + SS_{\text{Pure Error}} \tag{12}$$

Pure error is estimated from replicated experiments performed under identical conditions, particularly replicated centre points. It represents the natural experimental variability that exists even when all operating conditions are nominally unchanged. Lack of fit, in contrast, measures the additional disagreement between the fitted

mathematical model and the experimental observations that cannot be explained by pure experimental variability.

The corresponding lack-of-fit statistic is calculated as:

$$F_{\mathrm{LOF}} = \frac{MS_{\mathrm{LOF}}}{MS_{\mathrm{Pure\ Error}}} \tag{13}$$

Unlike the overall model significance test, a non-significant lack of fit is desirable, because it indicates that the remaining differences between the model and the experimental observations are not significantly greater than the inherent experimental error. Therefore, a lack-of-fit p-value above 0.05 generally supports the adequacy of the selected model. Since this p-value is greater than 0.05, the lack of fit is not statistically significant, supporting the suitability of the quadratic model within the investigated experimental domain.

Another important measure of model quality is the coefficient of determination, $R^2$, which describes the fraction of the total response variation accounted for by the fitted model:

$$R^2 = 1 - \frac{SS_{\mathrm{Error}}}{SS_{\mathrm{Total}}} \tag{14}$$

An $R^2$ value approaching unity indicates that a high proportion of the experimental variation is reproduced by the model. However, $R^2$ should not be used alone to judge model adequacy because adding additional terms can increase $R^2$ even when those terms do not meaningfully improve model performance.

For this reason, the adjusted coefficient of determination, $R^2_{\mathrm{adj}}$, can provide a more conservative assessment by considering both the amount of unexplained variation and the number of model terms:

$$R^2_{\mathrm{adj}} = 1 - \frac{SS_{\mathrm{Error}}/df_{\mathrm{Error}}}{SS_{\mathrm{Total}}/df_{\mathrm{Total}}} \tag{15}$$

Unlike ordinary $R^2$, $R^2_{\mathrm{adj}}$ may decrease when statistically uninformative terms are added to the model. Therefore, agreement between $R^2$, $R^2_{\mathrm{adj}}$, model significance, lack-of-fit results, and residual analysis provides a more reliable assessment of model quality than any single statistical indicator.

Response-surface and contour plots provide a graphical representation of the fitted polynomial and facilitate interpretation of interactions and curvature. A three-dimensional response surface illustrates the predicted response as two factors are varied while the remaining variables are held constant. The corresponding two-dimensional contour plot provides an alternative representation of the same fitted surface. Pronounced curvature indicates quadratic behaviour, whereas changes in contour orientation may reflect interactions between factors. Nevertheless, these graphical representations are primarily interpretative tools; numerical optimization is performed using the fitted polynomial rather than by visually selecting a maximum from the response-surface plot [64].

When more than one response must be optimized simultaneously, an individual desirability function can be assigned to each response. The desirability value $d_i$ varies

from 0 to 1, where 0 represents a completely undesirable response and 1 represents achievement of the specified optimization objective. Individual desirabilities can be combined into an overall desirability:

$$D = \left( \prod_{i=1}^{m} d_i^{w_i} \right)^{1/\sum_{i=1}^{m} w_i} \quad (16)$$

where m represents the number of responses and $w_i$ represents the relative weighting assigned to each response. Maximizing the overall desirability therefore allows several responses to be optimized simultaneously and identifies a compromise operating condition rather than an independent optimum for each individual response [64].

It is also important to distinguish a model-predicted optimum from experimental measurement precision. Because the fitted polynomial is a continuous mathematical function, numerical optimization may predict a value between the discrete conditions tested experimentally. The statistical optimum should therefore be interpreted in conjunction with experimental uncertainty and, where appropriate, confirmation experiments.

RSM should consequently be regarded as an empirical modelling and optimization methodology rather than as a mechanistic kinetic model. A statistically significant interaction or quadratic coefficient identifies a reproducible relationship within the investigated experimental domain but does not by itself establish the molecular origin of that behaviour. Similarly, predictions outside the investigated factor ranges constitute extrapolation and should be treated cautiously. Accordingly, statistical interpretation should be combined with chemical understanding of the ODS process and experimental evidence when drawing mechanistic conclusions [64].

Numerous studies have demonstrated the effectiveness of RSM in various fields. For instance, Bashir et al. [65] utilized RSM for wastewater treatment optimization, while Yolmeh and Jafari [66] applied it in food processing. In the pharmaceutical industry, RSM has been employed to formulate and evaluate sustained-release matrix tablets [67].

The versatility of RSM is further evidenced by its application in diverse areas, such as lithium recovery from highly concentrated solutions [68] and the optimization of catalytic performance in multistage plasma systems [69]. Recent advancements in RSM include the development of enhanced techniques, such as coefficient clipping based on prior knowledge [70] and the incorporation of observational data [71]. These innovations further expand the applicability and robustness of RSM in addressing complex optimization challenges across various scientific and industrial domains. In conclusion, Response Surface Methodology and Central Composite Design continue to be invaluable tools for researchers seeking to optimize process conditions and reactions. Their ability to efficiently explore multivariable spaces, model complex relationships, and identify optimal conditions makes them essential in modern scientific research and industrial applications. As the field evolves, RSM and CCD are likely to play an increasingly important role in advancing our understanding and control of complex systems across diverse disciplines.

## 1.6 Photo Oxidative Desulphurization

Photocatalytic oxidative desulphurization (PODS) has emerged as a promising technique for removing sulphur compounds from fuels, combining the principles of photocatalysis and adsorption to enhance desulphurization efficiency [72]. Semiconductor photocatalysts generate electron–hole pairs after absorption of photons with sufficient energy; subsequent interfacial reactions can form reactive oxygen species that participate in sulphur oxidation [73]. To address $TiO_2$ limited visible light absorption, researchers have explored doping with metals or coupling with other semiconductors. Adsorbents play a crucial role in PODS by concentrating sulphur compounds near the photocatalyst surface, with activated carbon fibres (ACF) [74] and metal-organic frameworks (MOFs) [75-76] showing particular promise due to their high surface area and tunable properties. Oxidizing agents, including hydroxyl radicals generated from $H_2O_2$ or persulfate ions, are essential for the degradation of sulphur compounds [77-78]. The synergistic effect between adsorption and photocatalysis has been demonstrated in various systems, such as $TiO_2$/ACF composites [79-80] and heterojunctions like $Cu_2V_2O_7/Cu_3V_2O_8/g\text{-}C_3N_4$ [81], which enhance visible light absorption and improve charge carrier separation. Despite significant progress, challenges remain in optimizing PODS processes, including mitigating the fast recombination of electron-hole pairs in photocatalysts and developing cost-effective, scalable synthesis methods for advanced materials. Ongoing research focuses on novel materials and process optimization to advance PODS technology towards commercial viability in clean fuel production.

# 2 Experimental

## 2.1 Materials and Methods

Zirconium(IV) chloride ($ZrCl_4$, 98%, Acros), 2-aminoterephthalic acid (99%, Acros), terephthalic acid (99%, Acros), 2-hydroxyterephthalic acid (99%, Acros), nitroterephthalic acid (99%, Acros), 4,4'-biphenyldicarboxylic acid (99%, Acros), hydrochloric acid (HCl, 36%, Honeywell), N,N-dimethylformamide (DMF, 99.5%, Fisher), ethanol ($C_2H_5OH$, 99.9%, Honeywell), acetonitrile (99.9%, Honeywell), n-dodecane (99%, Alfa Aesar), hydrogen peroxide ($H_2O_2$, 30%, Alfa Aesar), dibenzothiophene (98%, Acros Organics), 2-methylbenzothiazole (99%, Acros Organics), and 4,6-dimethyldibenzothiophene (97%, Alfa Aesar) were used as received.

### 2.1.1 Synthesis of Pristine UiO-66

Pristine and linker-functionalized UiO-66 materials were synthesized according to the experimental description specified in Table 1 [82]. $ZrCl_4$, one third of DMF, and concentrated HCl were combined in a 10-dram vial and sonicated for 20 minutes until complete dissolution was achieved. The linker and the remaining two-thirds of DMF were subsequently added, and the mixture was sonicated for an additional 20 minutes before being heated at the activation temperature for 24 hours, as the linker was not fully soluble under these conditions. The solid obtained was filtered and subsequently washed with DMF (15 mL per wash) followed by ethanol (15 mL per wash) three times. All samples were activated by heating to 80 °C under vacuum until a pressure of 600 mbar was attained.

*Table 1. Experimental ingredient amount and condition for the synthesis of UiO-66 derivatives.*

| MOF | Linker (Ligand) | linker (mmol) | $ZrCl_4$ (mmol) | Volume HCl (mL) | Volume DMF (mL) | Solvothermal Synthesis (activation) Temperature (°C) |
|---|---|---|---|---|---|---|
| UiO-66 | Terephthalic acid (BDC) | 0.74 | 0.74 | 1 | 15 | 150 |
| UiO-66-$NH_2$ | 2-aminoterephthalic acid | 0.74 | 0.74 | 1 | 15 | 150 |

| MOF | Linker (Ligand) | linker (mmol) | $ZrCl_4$ (mmol) | Volume HCl (mL) | Volume DMF (mL) | Solvothermal Synthesis (activation) Temperature (°C) |
|---|---|---|---|---|---|---|
| UiO-66-OH | 2-hydroxyterephthalic acid | 0.74 | 0.74 | 1 | 15 | 150 |
| UiO-66-$NO_2$ | nitroterephthalic acid | 0.74 | 0.74 | 1 | 15 | 150 |
| UiO-67 | 4,4'-biphenyldicarboxylic acid (BPDC) | 0.37 | 0.37 | 1 | 15 | 150 |

### 2.1.2 Synthesis of metal- modified UiO-66 derivatives

Metal-modified UiO-66 was prepared by a similar solvothermal method to UiO-66. The only difference is that before the thermal treatment in the solvent, a proper amount of metal agent was dissolved in 10 mL of DMF, and then the agent solution was added to the above precursor solution of the UiO-66 and the mixture solution was stirred for 1 h. The reaction conditions and the reagents are presented in Table 2. The molar ratio of each component (metal reagent:linker:$ZrCl_4$:DMF) is 1:1:1:250 , respectively).

*Table 2. Experimental ingredient amount and condition for the synthesis of metal UiO-66 derivatives.*

| MOF | Linker (Ligand) | Metal reagent | linker (g) | Metal reagent (g) | Mass $ZrCl_4$ (g) | Volume Acetic | Volume DMF (mL) | Activation Temperature (°C) | Activation Time (hr) |
|---|---|---|---|---|---|---|---|---|---|
| Ti-UiO-66 | Terephthalic acid (BDC) | $TiO_2$ | 1.03 | 0.495 | 1.45 | - | 120 | 120 | 24 |

| MOF | Linker (Ligand) | Metal reagent | linker (g) | Metal reagent (g) | Mass $ZrCl_4$ (g) | Volume Acetic | Volume DMF (mL) | Activation Temperature (°C) | Activation Time (hr) |
|---|---|---|---|---|---|---|---|---|---|
| Mn-UiO-66 | Terephthalic acid (BDC) | $MnCl_2 \cdot 4H_2O$ | 1.03 | 1.23 | 1.45 | - | 120 | 120 | 24 |
| Co-UiO-66 | Terephthalic acid (BDC) | $CoCl_2 \cdot 6H_2O$ | 1.03 | 1.48 | 1.45 | - | 120 | 120 | 24 |
| Cu-UiO-66 | Terephthalic acid (BDC) | $Cu(NO_3)_2 \cdot 3H_2O$ | 1.03 | 1.50 | 1.45 | 12 | 120 | 120 | 48 |
| Fe-UiO-66 | Terephthalic acid (BDC) | $FeCl_3 \cdot 6H_2O$ | 1.03 | 1.68 | 1.45 | - | 120 | 120 | 24 |
| Ce-UiO-66 | Terephthalic acid (BDC) | $CeCl_3 \cdot 7H_2O$ | 1.03 | 2.31 | 1.45 | 8 | 120 | 120 | 48 |

### 2.1.3 Synthesis of impregnated Metal Doped UiO-66

Metal/UiO-66 materials prepared by wet impregnation used 0.83 g of UiO-66 and an aqueous solution containing the selected metal precursor. The suspension was sonicated for 120 min and then left to impregnate overnight. The solid was subsequently washed with DMF and ethanol and dried under vacuum at 80 °C.

## 2.2 Catalyst Tests

ODS reactions were performed in a 22 mL closed, chemically resistant capped glass vial (Figure 3), i.e. the reaction was not conducted in an open test tube. The model fuel contained 1000 ppm of each sulphur compound (DBT, 2-MB, and 4,6-DMDBT) in n-dodecane. Acetonitrile (3 mL) was added as the polar phase to obtain a 1:1 volumetric ratio with the fuel phase. The prescribed amount of MOF catalyst was added according to the experimental design, and $H_2O_2$ was introduced after the reactor had reached the target temperature. After reaction, the polar and hydrocarbon phases were separated

and analysed by gas chromatography (Shimadzu QP2010 Plus) to quantify the remaining sulphur compounds.

The PODS activity was evaluated using DBT and 4,6-DMDBT as representative sulphur compounds in the model fuel. These substrates were selected to compare an unhindered dibenzothiophene benchmark (DBT) with a sterically hindered refractory analogue (4,6-DMDBT); 4-MDBT was not part of the defined model-fuel composition used for this PODS screening and was therefore not included. A model fuel containing 500 ppm sulphur in 20 mL of n-octane was introduced into the photoreactor. The system contained 10 mg photocatalyst and 0.3 mL n-dodecane as an internal standard, together with 20 mL deionized water (organic-to-aqueous phase ratio 1:1, v/v). The suspension was stirred at 500 rpm and kept in the dark for 60 min before irradiation to establish adsorption–desorption equilibrium.

The photoreactor was a double-jacketed quartz-glass vessel. Quartz was selected because it transmits the UVC component at 253.7 nm, unlike ordinary soda-lime glass, which strongly attenuates short-wavelength UV radiation. Irradiation was supplied by UV/visible LED sources at 253.7 nm (UVC), 380 nm (UVA), and in the visible range. The reaction temperature was controlled by circulating water through the outer jacket. A fixed lamp-to-reactor geometry was maintained for reproducible irradiation (Figure 4). During irradiation, air was continuously introduced at 25–200 mL $min^{-1}$. Aliquots were withdrawn from the oil phase at predetermined times for analysis.

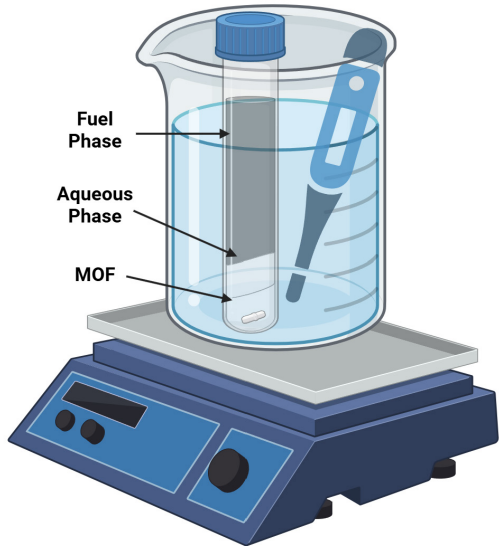



*Figure 3. Schematic of Experimental System used for Oxidative Desulphurization.*

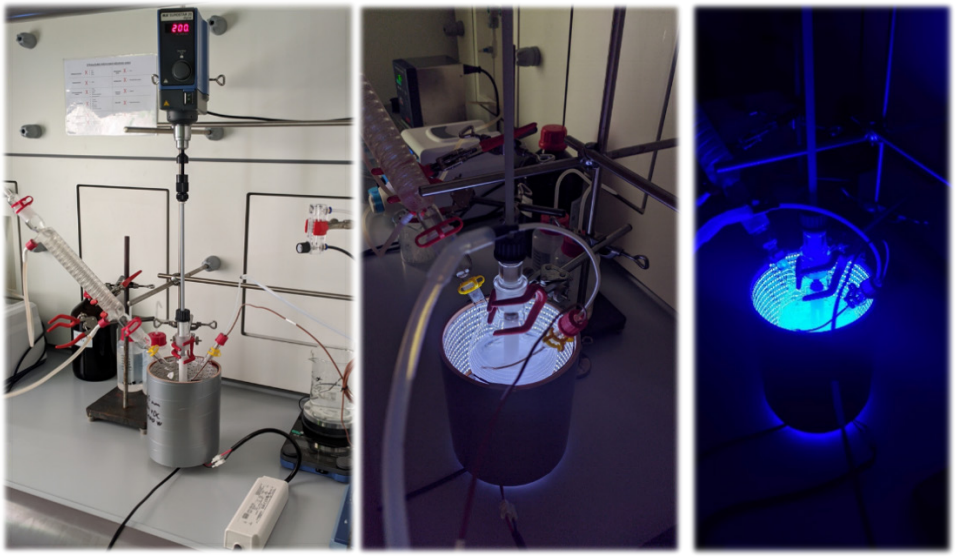


*Figure 4. Photocatalytic reactor set-up using LED strip; The reactor consists of a double-jacket glass vessel through which temperature-controlled water is circulated. A mechanical agitator is positioned at the centre of the reactor to ensure homogeneous mixing. An inlet tube is provided for oxidant (air) introduction into the reaction medium. The LED strip is arranged around the outer jacket to provide uniform irradiation to the reaction mixture.*

## 2.3 Characterization Methods

X-ray powder diffraction (XRD) is an analytical technique used to determine the crystalline structure of materials, and in this study, it was performed using an X'Pert3 Powder diffractometer from Malvern Panalytical. This instrument employs Cu Kα radiation with a wavelength of 0.154 nm, which is optimal for resolving the atomic structure of crystalline materials due to its suitable wavelength for diffraction experiments. The choice of Cu Kα radiation is standard in XRD analysis as it provides a balance between penetration depth and diffraction efficiency, allowing for detailed phase identification and structural analysis. Fourier transform infrared (FT-IR) spectroscopy was conducted using a Nicolet iS50 FTIR spectrometer to identify functional groups present in the samples. The attenuated total reflectance (ATR-FTIR) method was employed, which is advantageous for directly examining solid samples such as UiO-66 derivative metal-organic frameworks (MOFs) without requiring extensive sample preparation. This technique provides insights into the molecular vibrations and chemical bonds within the material, essential for understanding its chemical environment.

Scanning electron microscopy (SEM) was utilized to investigate the surface morphology and microstructural features of the samples. The SEM images were captured using a Zeiss FEG-SEM Ultra-55, which offers high-resolution imaging capabilities for observing the surface texture and particle size distribution of the synthesized MOFs. Thermogravimetric analysis (TGA) was performed on a Mettler-Toledo TGA 1 to assess the thermal stability and composition of the samples by measuring weight changes under controlled temperature conditions. This analysis is vital for determining decomposition temperatures and evaluating the thermal robustness of MOFs.

Elemental composition and purity were assessed using microwave plasma atomic emission spectroscopy (MP-AES) on an Agilent 4200 spectrometer. This technique allows for precise quantification of elemental ratios by analysing the emission spectra produced by microwave-induced plasma, providing critical data on sample purity and stoichiometry. Proton nuclear magnetic resonance ($^1$H NMR) spectroscopy was conducted at 25°C on a 500 MHz Agilent DD2 NMR spectrometer with a 5 mm ID PFG probe head, allowing for detailed investigation of the chemical environment and molecular structure through hydrogen atom interactions.

Nitrogen adsorption–desorption isotherms were measured at 77 K using a Quantachrome Autosorb-iq device after degassing the samples at 408 K for 18 hours under vacuum. This procedure ensures that all physisorbed molecules are removed from the sample surface, allowing accurate measurement of surface area and porosity. The specific surface areas were calculated using Quantachrome AsiQwin 5.23 software based on the Brunauer–Emmett–Teller (BET) method, which is widely used for characterizing porous materials like MOFs due to its ability to provide surface area estimates from gas adsorption data. These comprehensive analytical techniques collectively provide a robust characterization framework necessary for understanding the structural and functional properties of UiO-66 derivative MOFs.

X-ray photoelectron spectroscopy (XPS) analyses were conducted using an Axis Ultra DLD spectrometer (Kratos Analytical) equipped with a monochromatic Al Kα X-ray source (hν = 1486.6 eV). Temperature-programmed desorption of $NH_3$ ($NH_3$-TPD) was performed using a FINESORB-3010 instrument fitted with a thermal conductivity detector. Prior to analysis, the samples were degassed at 300 °C for 2 hours. After cooling to 25 °C, the samples were exposed to a stream of $NH_3$ (5% in Ar) for 1 hour to achieve saturation, followed by purging with Ar (30 mL/min) for 1 hour to eliminate physisorbed

$NH_3$. The TPD profiles were then obtained by heating the samples from 25 °C to 400 °C at a constant ramping rate of 5 °C/min.

## 2.4 Design of Experiments

A central composite design (CCD) was used within Response Surface Methodology (RSM) to model the nonlinear effects of the principal ODS operating variables. CCD combines factorial, axial, and centre points and permits estimation of a full quadratic polynomial with substantially fewer experiments than a complete multi-level factorial design [83]. For the three numerical factors used here, the rotatable axial distance was $\alpha = (2^3)^{1/4} = 1.682$.

The coded factor value was calculated as mentioned in equation 2. The response was fitted to $y = \beta_0 + \sum_{i=1}^{k} \beta_i x_i + \sum_{i=1}^{k} \beta_{ii} x_i^2 + \sum_{i<j} \beta_{ij} x_i x_j + \varepsilon$. Model terms were assessed by ANOVA and F-tests; $p < 0.05$ was used as the conventional threshold for statistical significance. $R^2$ was considered together with residual diagnostics and lack-of-fit when assessing model adequacy.

For numerical optimization, the fitted sulphur-removal responses were transformed into desirability functions. Each individual desirability $d_i$ ranges from 0 to 1, where 0 represents an unacceptable predicted response and 1 represents attainment of the specified optimization goal. When several responses were optimized simultaneously, the overall desirability was treated as a geometric combination of the individual desirabilities. Consequently, the RSM optimum is a model-derived compromise point and should be reported with appropriate experimental precision rather than interpreted as an exact physical set point.

The structure of a CCD comprises three distinct components: a factorial or fractional factorial design, axial points (also known as star points), and center points. The factorial portion allows for the estimation of main effects and interactions, while the axial points facilitate the assessment of curvature in the response surface. Center points, often replicated, enhance the precision of the experiment and enable the evaluation of model lack-of-fit.

One of the key advantages of CCD is its ability to provide a comprehensive understanding of the response surface with relatively fewer experimental runs compared to full three-level factorial designs. This efficiency is particularly beneficial in situations where experimental resources are limited or when dealing with time-consuming or costly processes.

The design rotatability feature ensures uniform prediction variance at all points equidistant from the design center, which is crucial for generating reliable response surface models. This property is achieved by carefully selecting the distance of the axial points from the center, denoted by α, which is typically calculated based on the number of factorial points in the design [83].

CCD offers flexibility in its implementation, with variations such as circumscribed, inscribed, and face-centered designs. These variations allow researchers to adapt the experimental design to specific constraints or requirements of their study. For instance, the face-centered design uses only three levels per factor, which can be advantageous when factor level ranges are restricted.

The oxidative desulphurization efficiency was investigated with the Response Surface Methodology employing the Central Composite Design (CCD). The parameters assessed were reaction temperature ($X_1$), oxidant-to-sulphur mass ratio ($X_2$), MOF mass dosage

($X_3$), and selected MOF ($X_4$). The first three variables are designated at five levels as numerical parameters and the fourth variable as a categorical parameter. The analysis of variance (ANOVA) was performed to evaluate the factors for the fitted quadratic model and the fitness of the polynomial model was evaluated by the coefficient of determination $R^2$ [84]. The F-test assessed the model and parameter significance and the p-value with a specified confidence level was used to verify the model terms. The second-order polynomial equation is given in equation (1). Referring to Central Composite Design, 17 experimental runs were carried out including axial, factorial and central runs. The oxidative sulphur removal reactions were conducted for each MOF. Table 3 gives the actual and coded levels.

*Table 3. Independent test variables at five levels were used in the central composite design for four different MOFs, UiO-66(Zr), UiO-66-OH, UiO-66-$NO_2$ and UiO-66-$NH_2$.*

| Parameter | Code | Units | Coded Variable Levels | | | | |
|---|---|---|---|---|---|---|---|
| | | | (-α) | (-1) | (0) | (+1) | (+α) |
| Temperature | $X_1$ | °C | 20 | 36.21 | 60 | 83.78 | 100 |
| Oxd./Sul. mass ratio | $X_2$ | (mg/mg) | 0.5 | 1.61 | 3.25 | 4.89 | 6 |
| Cat./Sul. mass ratio | $X_3$ | (mg/mg) | 0.5 | 3.44 | 7.75 | 12.06 | 15 |

α: 1.68

## 2.5 Kinetic Study

The oxidative desulphurization (ODS) mechanism was elucidated, encompassing both monomolecular and bimolecular reactions. The product stream comprises water, mono-oxygenated dibenzothiophene (DBTO, i.e., dibenzothiophene sulfoxide), dioxygenated dibenzothiophene ($DBTO_2$, i.e., dibenzothiophene sulfone), and unreacted DBT. The proposed ODS mechanism for DBT over the metal-organic framework (MOF) involves 11 elementary steps, detailing the sequential formation of primary sulfone (dioxygenated sulphur) and sulfoxide (mono-oxygenated sulphur) during the reaction stages [publication III].

The kinetic study was conducted on UiO-66-$NO_2$ using the Complex Reaction methodology. The kinetic rate parameters were determined by minimizing an objective function that compares the model-predicted values with the experimental data. The evaluation of kinetic coefficients in heterogeneous catalytic reactions involves the analysis of nonlinear equations to accurately assess the kinetic behaviour.

# 3 Results and Discussion

## 3.1 Characterization

### 3.1.1 XRD

X-ray diffraction (XRD) analysis was utilized to evaluate the crystal structure and phase purity of the synthesized metal-organic frameworks (MOFs). The diffraction patterns exhibited characteristic peaks corresponding to the Miller indices (111), (200), (220), (400), (600) [85], confirming the successful synthesis of UiO-67, UiO-66 and its derivatives, UiO-66-OH, UiO-66-$NH_2$ and UiO-66-$NO_2$ (Figure 5) and metal doped UiO-66 (Figure 6).

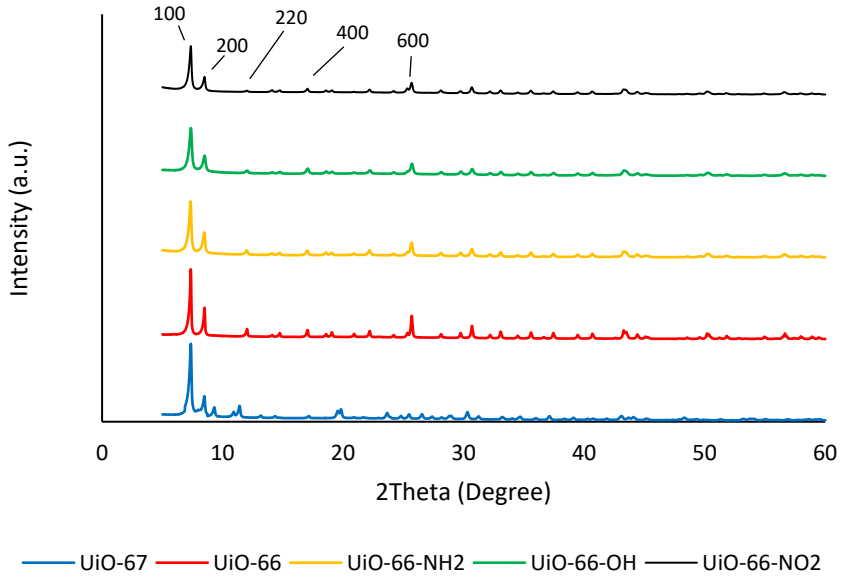



*Figure 5. XRD powder patterns of UiO-67, UiO-66, UiO-66-$NH_2$, UiO-66-OH, and UiO-66-$NO_2$.*

In the case of Co-doped UiO-66, the characteristic diffraction peaks of pure UiO-66 are generally maintained, confirming that cobalt doping does not destroy the overall crystal structure [86-87]. Cu-and Ti-doped UiO-66 generally maintains the characteristic diffraction peaks of the pure phase UiO-66, confirming the structural integrity at low to moderate concentrations. Peak intensity may decrease lightly upon doping, and peaks may shift to higher 2Theta values, suggesting partial substitution of larger $Zr^{4+}$ ions [88]. Ce-based UiO-66 maintains the face-centered cubic structure of UiO-66, with characteristic peaks (e.g., $2\theta \approx 7.2°, 8.3°, 11.7°$) confirming successful synthesis. Both Fe- and Mn-doped UiO-66 retain the characteristic diffraction peaks of the parent UiO-66 framework, confirming that neither Fe nor Mn modification significantly disrupts the crystal structure or crystallinity of the material.

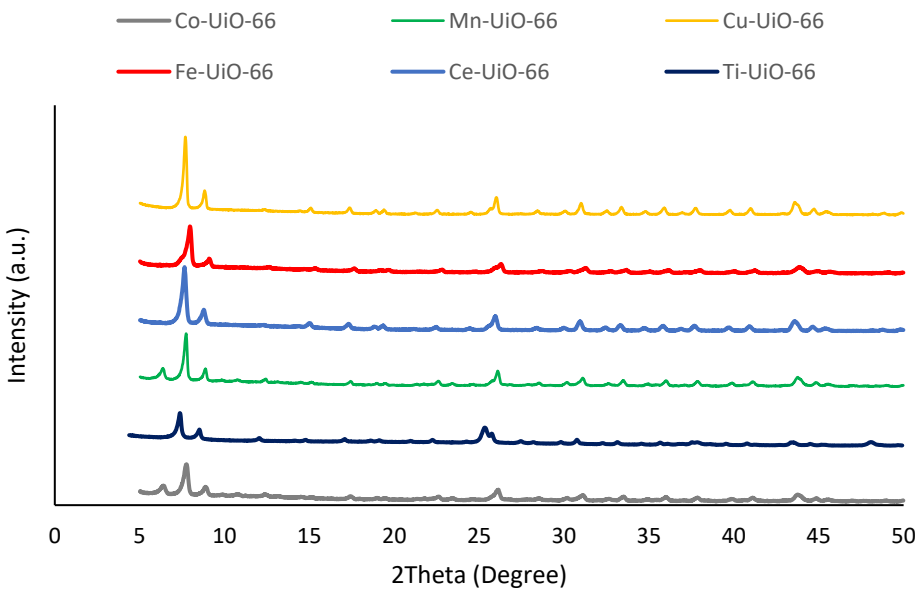



*Figure 6. XRD powder patterns of solvothermal metal doped on UiO-66.*

### 3.1.2 FTIR

Fourier-transform infrared spectroscopy (FTIR) was employed to investigate the chemical composition and bonding characteristics of the synthesized UiO-66 derivatives (Figure 7, Figure 8 and Figure 9). The FTIR spectra revealed consistent vibrational bands across all three MOFs, with notable peaks at ~660 $cm^{-1}$ and ~766 $cm^{-1}$, attributed to C–H and O–H vibrations in the benzene dicarboxylate (BDC) aromatic ring, respectively. Additionally, symmetric and asymmetric O–C–O stretching modes were observed at ~1400 $cm^{-1}$ and ~1570 $cm^{-1}$, respectively [89-90]. These spectroscopic features corroborate the successful incorporation of the organic linkers within the MOF structures. The combined XRD and FTIR analyses provide compelling evidence for the successful synthesis and structural characterization of UiO-66 and its functionalized derivatives, demonstrating the efficacy of the employed synthetic protocols and analytical techniques in MOF research.

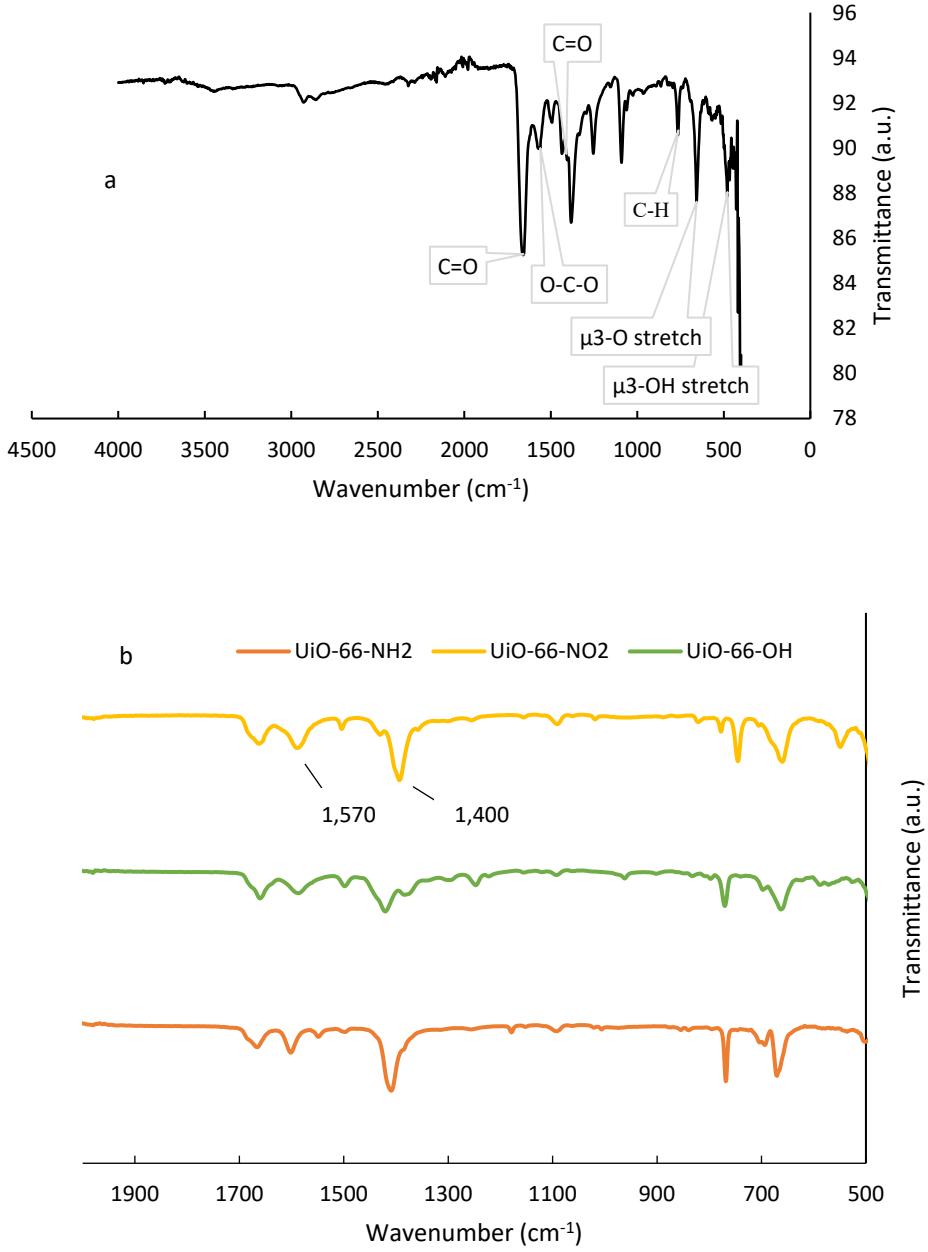



*Figure 7. FTIR spectra of UiO-66 and the linker-functionalized UiO-66-$NH_2$, UiO-66-$NO_2$, and UiO-66-OH materials.*

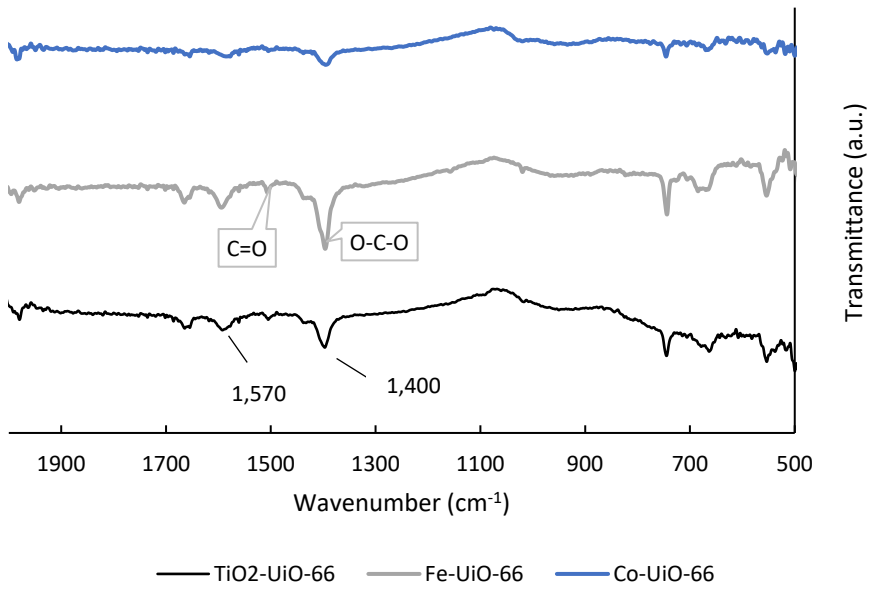



*Figure 8. FTIR spectra of Ti-UiO-66, Fe-UiO-66 and Co-UiO-66.*

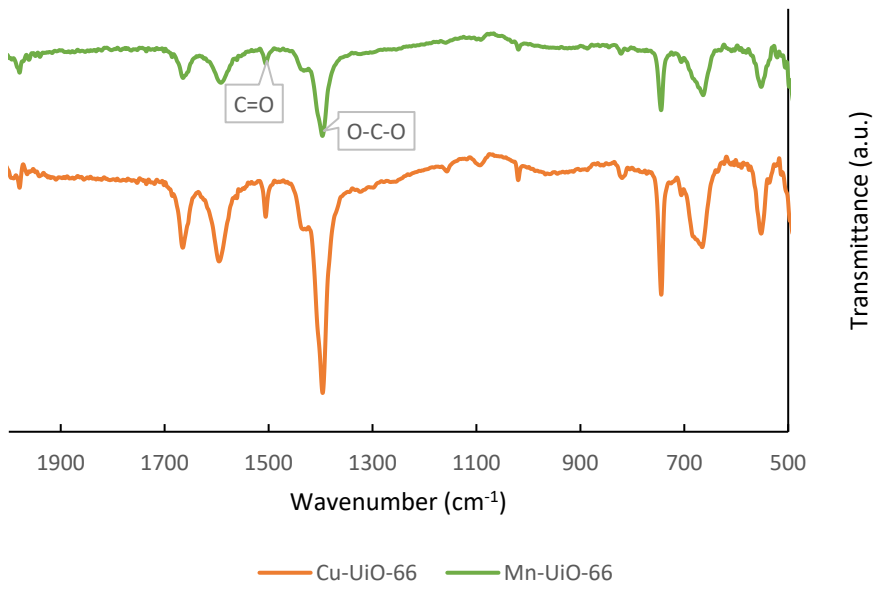
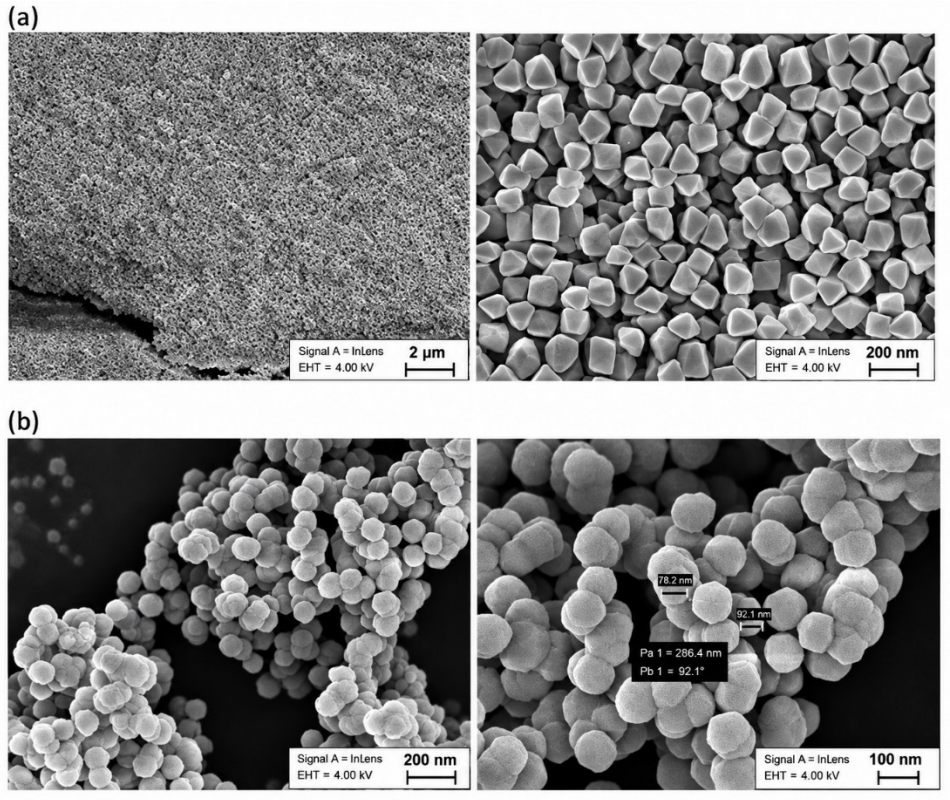



*Figure 9. FTIR spectra of Cu-UiO-66 and Mn-UiO-66.*

The FTIR spectra of Co-doped UiO-66 materials are very similar to those of UiO-66, confirming that the organic linker structure remains intact. A pronounced peak at ~1646 $cm^{-1}$ observed in Co-UiO-66 was more plausibly assigned to adsorbed water (H–O–H bending) and/or residual DMF-related vibrations. It should be noted that Co–O stretching modes are not detectable by FTIR and would require Raman spectroscopy for

unambiguous identification [91]. The FTIR spectra of all remaining metal-doped UiO-66 variants, including Cu-, Ti-, Mn-, Fe-, and Ce-doped materials, closely resemble that of the parent UiO-66, confirming that metal incorporation does not significantly alter the fundamental organic linker structure or the inorganic Zr–O framework, consistent with the XRD findings.

### 3.1.3 SEM



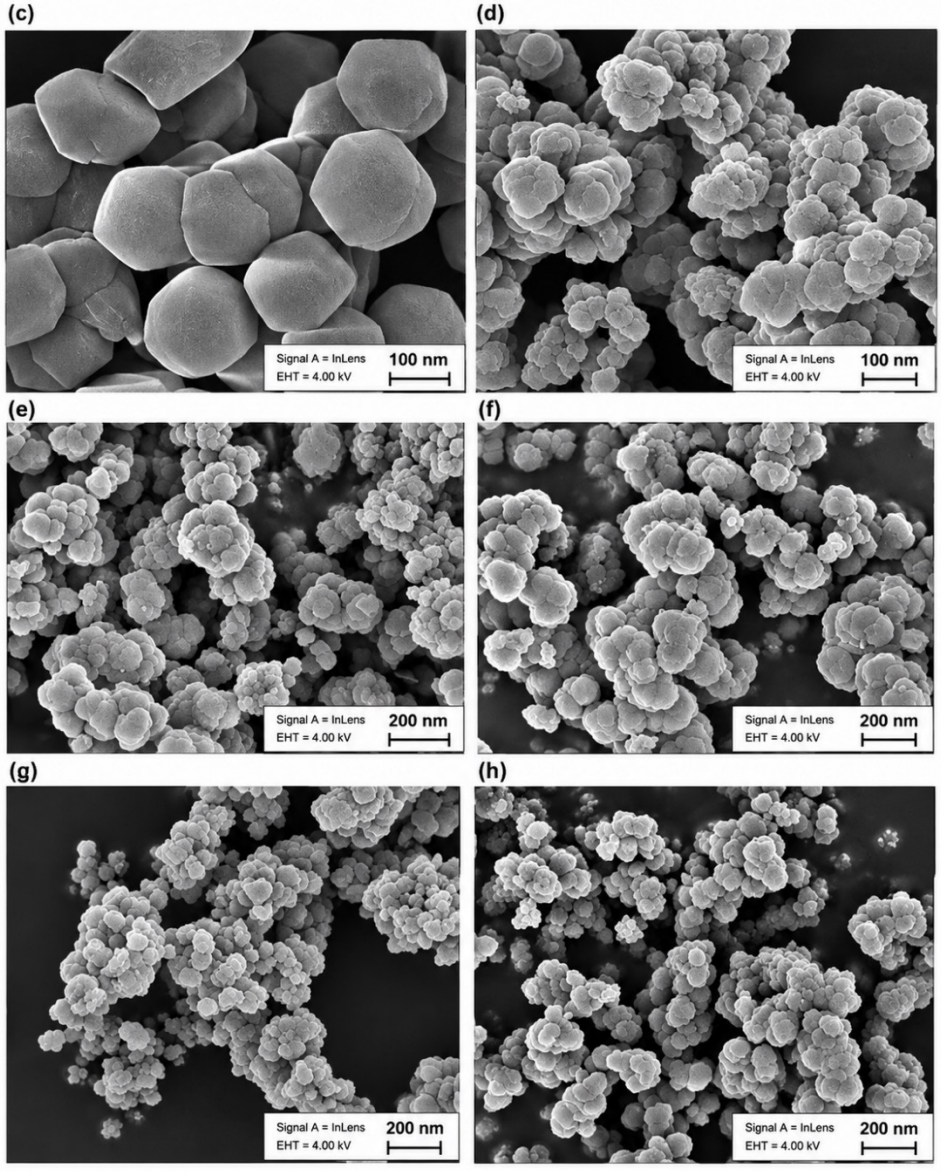



*Figure 10. SEM micrographs arranged as a single aligned high-resolution panel: (a) UiO-66, (b) UiO-66-$NH_2$, (c), UiO-66-OH, (d) UiO-66-$NO_2$, (e) Ce-UiO-66, (f) Ti-UiO-66, (g) Cu-UiO-66, (h) Mn-UiO-66.*

The scanning electron microscopy (SEM) micrographs of the UiO-66 metal-organic framework (MOF), as depicted in Figure 10, reveal a consistent octahedral morphology characteristic of this material. SEM images indicate that the particle size distribution is relatively narrow, with the majority of crystallites falling within the range of 350-360 nm in diameter. In contrast, the UiO-66 derivatives exhibited a more pronounced deviation from the ideal octahedral morphology, as evidenced in Publication I and Publication II. These functionalized variants displayed a higher degree of structural irregularity, while maintaining a particle size distribution ranging from approximately 340 to 370 nm. This

observed morphological heterogeneity can be attributed to the incorporation of functional groups, which may influence the crystal growth kinetics and resultant particle formation.

While pristine UiO-66 typically forms octahedral crystals, Co doping has been reported to reduce the crystal size [92]. As shown in Figure 10, doping with Fe, Mn, Ce, Ti, or Cu generally does not markedly change the particle morphology of UiO-66. For example, Yang et al. confirmed a successful and relatively uniform distribution of Fe, suggesting that Fe is incorporated within the internal metal clusters rather than forming a separate Fe-rich phase [93]

### 3.1.4 NMR

The $^{1}$H NMR spectra of UiO-66 and UiO-66-OH after digestion in NaOD/$D_2O$ are presented in Figure 11. The observed aromatic resonances are consistent with BDC- and hydroxy-substituted BDC-derived species in solution. Since digestion disrupts the MOF framework and the strongly basic NaOD/$D_2O$ medium causes deprotonation and H/D exchange of exchangeable acidic protons, these spectra provide information on the chemical identity of linker-derived species rather than on the three-dimensional structure of the MOF framework [94].

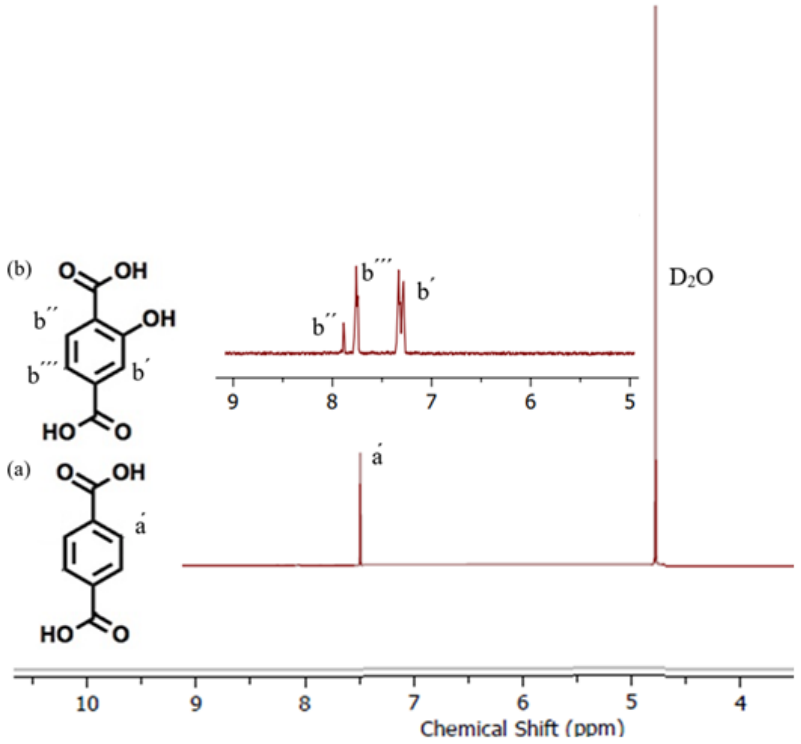



*Figure 11. $^{1}$H NMR spectra of digested (a) UiO-66 and (b) UiO-66-OH in NaOD/$D_2O$. The labelled resonances correspond to aromatic protons of BDC- and hydroxy-substituted BDC-derived species in the digested samples.*

### 3.1.5 TGA

Thermogravimetric analysis (TGA) of the UiO-66 derivatives reveals a multistage decomposition profile characteristic of these metal-organic frameworks (Figures 12 and 13). The initial weight loss of approximately 3–5 wt.%, observed in the temperature range of 45–100 °C, can be attributed to the desorption of physisorbed and weakly bound solvent molecules, primarily water and ethanol, from the porous structure. A subsequent mass reduction of approximately 10–15 wt.% is associated with the elimination of residual *N,N*-dimethylformamide (DMF), which is commonly used as a synthesis solvent and may remain trapped within the MOF cavities; for UiO-66-type materials, solvent release is frequently observed up to approximately 300 °C. The final and most significant mass loss of approximately 40–45 wt.%**,** occurring at around 520 °C, corresponds to the thermal decomposition of the organic linkers and collapse of the framework, ultimately yielding zirconium oxide ($ZrO_2$) as the decomposition product [95].

The stepwise thermal degradation profiles provide information on the thermal stability and composition of the UiO-66 derivatives and further support the characterization of the synthesized functionalized MOFs [Publications I and II].

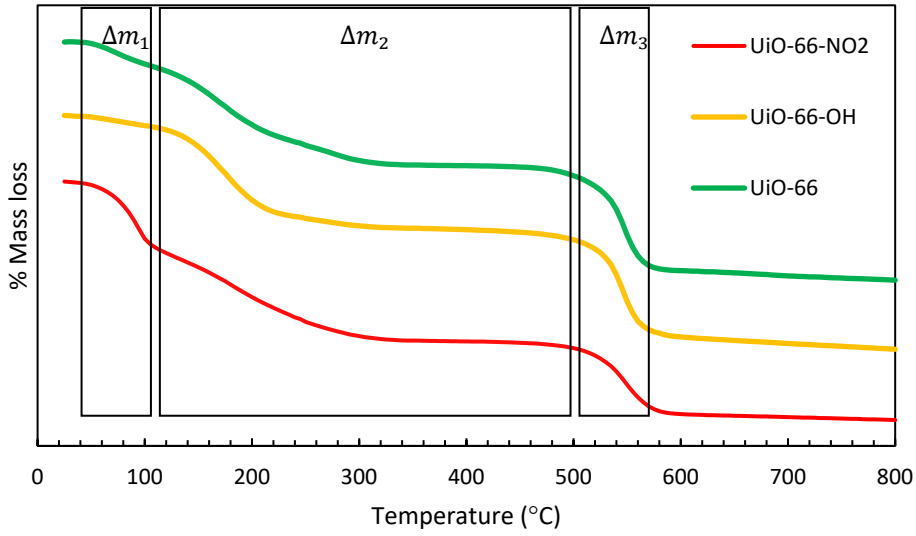



*Figure 12. TGA curves of UiO-66, UiO-66-OH, and UiO-66-$NO_2$, showing the main mass-loss regions associated with removal of adsorbed species ($\Delta m_1$), residual solvent ($\Delta m_2$), and framework decomposition ($\Delta m_3$), $\Delta m_1 \approx 3–5$ wt.%, $\Delta m_2 \approx 10–15$ wt.%, $\Delta m_3 \approx 40–45$ wt.% (Publication II).*

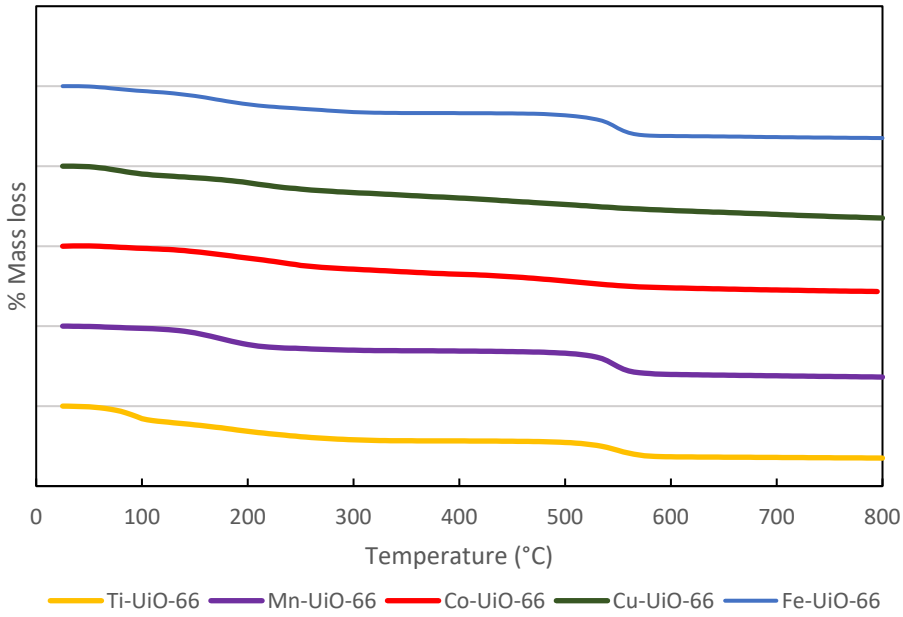



*Figure 13. Thermogravimetric curves of metal-modified UiO-66 samples. Curves are vertically offset for clarity; ordinate values represent mass (%) plus the plotting offset.*

The metal-modified MOFs exhibited thermal stability comparable to that of the parent UiO-66. However, Co-modified UiO-66 showed experimental weight-loss plateaus below the theoretical weight loss of approximately 55 wt.% reported for UiO-66 [92]. Increasing Co content was also associated with a shift of the decomposition region toward lower temperatures, which has been attributed to reduced crystal size and increased defect density [92]. Similarly, the TGA behaviour of Ti-UiO-66 has been reported to be consistent with increased structural defects relative to parent UiO-66, suggesting that $Ti^{4+}$ incorporation may affect the formation of the ordered UiO-66 framework [96]. Nevertheless, because TGA primarily provides information on thermal decomposition and residual mass, these observations should be interpreted as being consistent with changes in defect content rather than as direct evidence of framework defect density.

### 3.1.6 XPS

X-ray photoelectron spectroscopy (XPS) analysis was performed to investigate electron transfer phenomena around zirconium (Zr) centres in UiO-66 and its derivatives. The binding energy (BE) values of the Zr $3d_{5/2}$ core level, which correspond to Zr–O coordination in the UiO-66 framework, are illustrated in Figure 14. The Zr 3d peaks of the functionalized or metal-incorporated UiO-66 samples exhibited slight shifts to lower binding energy compared with pristine UiO-66 (Zr $3d_{5/2}$ = 182.6 eV). These shifts indicate a change in electron density around Zr sites due to electron-donating or electron-withdrawing effects of incorporated metal ions or organic functional groups. Specifically, the introduction of amino ($–NH_2$) groups can enhance electron density around Zr centres, which may lead to a lower BE, whereas electron-withdrawing groups such as nitro ($–NO_2$) often decrease electron density and are frequently associated with higher BE values,

consistent with previous reports [97-98]. These results confirm that electron transfer between the Zr–O nodes and the introduced substituents or dopants plays a significant role in modulating the electronic environment of UiO-66-based frameworks. Upon loading Cu particles, the Zr 3d peaks shift to lower binding energy (to 182.3 eV). This is consistent with charge transfer from Cu species to Zr, where Cu acts as an electron donor to the Zr-oxo secondary building units (SBU) [99]. It was reported that Fe-doped UiO-66 also shows a shift to lower binding energy, reflecting a modified chemical environment induced by specific Fe-O-Zr interactions [100].

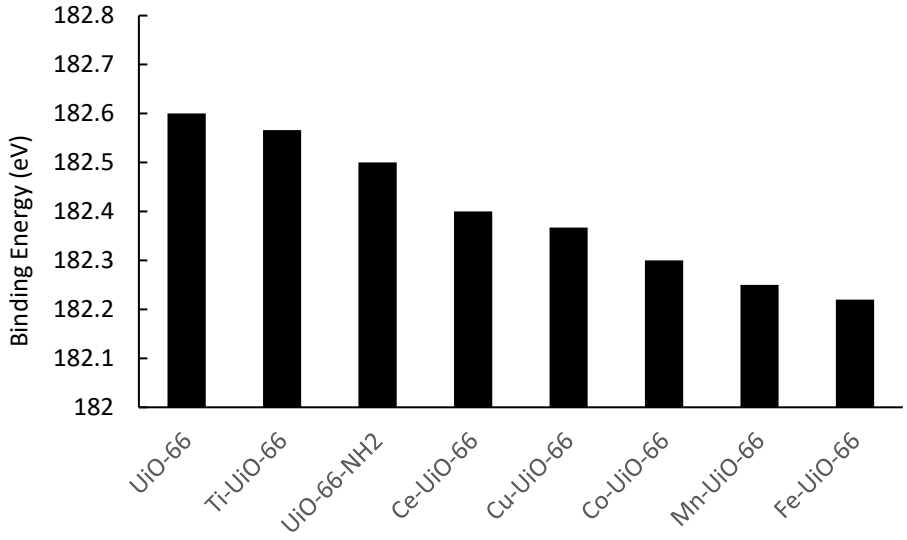



*Figure 14. X-ray photoelectron spectroscopy (XPS) spectra of the Zr 3d region for UiO-66 and its derivatives. The peaks correspond to the spin–orbit doublet of Zr $3d_{5/2}$ and Zr $3d_{3/2}$ components associated with the Zr(IV)–O coordination environment in the UiO-66 framework (typical splitting ≈ 2.4 eV).*

### 3.1.7 Nitrogen Adsorption–Desorption Analysis

Table 4 summarizes the isotherm data and the zirconium content in the MOFs, as quantified by MP-AES. The BET surface area analysis reveals that UiO-66 (1649 $m^2/g$) exhibits a significantly higher surface area compared to its functionalized derivatives, UiO-66-OH (1052 $m^2/g$) and UiO-66-$NO_2$ (976 $m^2/g$). Furthermore, UiO-66-$NO_2$ demonstrates a larger pore width (~1.63 nm) than the other variants. Functionalization reduces surface area and micropore volume due to linker functional groups partially blocking pore windows yet retains the Type I (IUPAC) character. The corresponding nitrogen adsorption-desorption isotherms for pristine UiO-66 and its derivatives are presented in Figure 15. The nitrogen adsorption-desorption isotherm of UiO-66 exhibits a Type I (Langmuir), characteristic of microporous materials. The sharp uptake at low relative pressures ($P/P_0 < 0.05$) shows the steep initial adsorption branch reflecting strong micropore filling due to the high affinity of nitrogen molecules for the uniform, narrow

pores of UiO-66 [90]. The minor uptick in adsorption near saturation pressure (P/P0→1) is attributed to $N_2$ condensation in interparticle spaces (i.e., packing effects of aggregates) or secondary mesoporosity arising from framework defects [101].

Reported trends for metal-modified UiO-66 are variable but generally indicate only modest structural changes. Some studies report that the BET area can decrease (e.g., from 1649 to 802 $m^2/g$), possibly due to Co species occupying free space or pores [86]. Cu loading causes a decrease in BET surface area and micropore content. This reduction is mainly attributed to the CuO nanoparticles partially blocking micropores, a consequence of the impregnation process used [102]. After doping Ti, the BET surface area and micropore volume systematically decreased, possibly due to the loss of well-ordered structure [96]. For Ce introduction, the specific surface area of Ce-UiO-66 is lower than conventional UiO-66, which is attributed to the presence of mesoporous features and structural rearrangement that reduce the overall surface-area density [103]. A lower surface area was reported for Fe-UiO-66, attributed to the occupation of pore spaces within the host framework by $Fe^{3+}$ species [104]. Mn-UiO-66 sample exhibited a decrease in surface area and pore volume, suggesting that manganese particles deposit or block the pores [105].

*Table 4. Zirconium content and textural properties of the synthesized MOFs.*

| MOF | Amount of zirconium (wt%) | BET Surface Area ($m^2/g$) | Total Pore Volume ($cm^3/g$) | Pore Width (nm) |
|---|---|---|---|---|
| UiO-66 | 26.2 | 1649 | 0.61 | 1.11 |
| UiO-66-OH | 25.1 | 1052 | 0.29 | 1.38 |
| UiO-66-$NO_2$ | 24.2 | 976 | 0.43 | 1.63 |
| UiO-66-$NH_2$ | 25.2 | 1009 | 0.43 | 1.19 |
| Ti-UiO-66 | 19.7 | 902 | 0.43 | 2.02 |
| Mn-UiO-66 | 22.6 | 860 | 0.42 | 1.87 |
| Co-UiO-66 | 23.4 | 802 | 0.42 | 2.11 |
| Ce-UiO-66 | 24.8 | 780 | 0.37 | 2.18 |

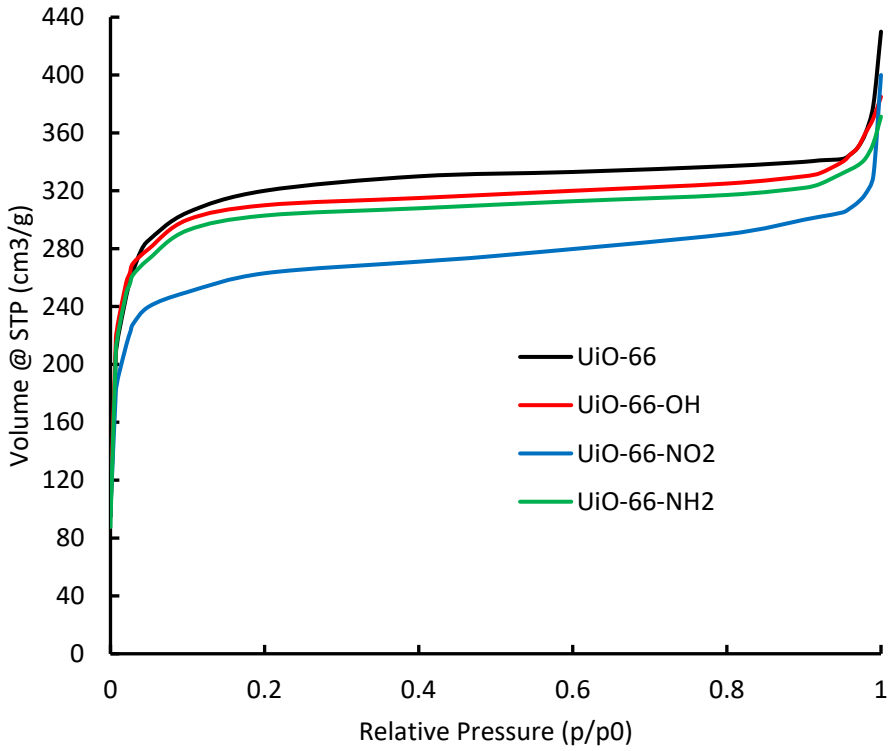



*Figure 15. Nitrogen adsorption–desorption/BET textural analysis of the synthesized UiO-66-based materials.*

## 3.2 Effect of Parameters

Experiments followed the CCD described in Section 2.4. Reaction temperature, O/S mass ratio, and C/S mass ratio were varied systematically for UiO-66, UiO-66-OH, UiO-66-$NO_2$, and UiO-66-$NH_2$. The resulting data, including model-predicted values and experimental findings, are summarized in Table 2 [Publication I] and Table S1 [Publication II]. Additionally, four polynomial equations with coded factors were developed through multiple regression analysis in Publication I and Publication II, to describe the behaviour of dibenzothiophene (DBT), 2-methylbenzothiazole (2-MB), and 4,6-dimethyldibenzothiophene (4,6-DMDBT).

The F-values and coefficient of determination ($R^2$) were evaluated using multiple regression and polynomial model fitness, respectively. A quadratic mathematical model was applied through ANOVA to determine the efficiency of sulphur removal. The F-values indicate a probability of less than 0.01% that the observed F-values resulted from random noise. Furthermore, p-values below 0.05 confirmed the statistical significance of the experimental design models for sulphur removal. The coefficient of determination ($R^2$) values, which were more than 0.90, demonstrated that the model was well-fitted to the experimental data. A comparison between the experimental and model-predicted values, illustrated in Figure 6 [Publication I] and [Publication II] revealed a strong correlation between the predicted and observed sulphur elimination yields. The root-

mean-square deviation between the experimental results and the predicted model was 3.8%.

The normal probability plot of the residuals, as depicted in Figure 7 [Publication I] and Figure S3 [Publication II], confirms the reliability of the model. The linear alignment of the data points for dibenzothiophene (DBT), 2-methylbenzothiazole (2-MB), and 4,6-dimethyldibenzothiophene (4,6-DMDBT) suggests that the residuals follow a normal distribution. This further supports the robustness and validity of the model.

This study was conducted to investigate the influence of individual factors and their interactions using response surface methodology (RSM). The impact of reaction temperature, oxidant-to-sulphur (oxd./sul.) ratio, and catalyst-to-sulphur (cat./sul.) ratio on the efficiency of sulphur removal was systematically analysed for UiO-66, UiO-66-OH, UiO-66-$NO_2$, and UiO-66-$NH_2$. Raising the reaction temperature from 60 °C to an optimum level enhances the sulphur oxidation yield at a specific oxidant-to-sulphur mass ratio; however, further increases beyond that level result in a decline in sulphur oxidation efficiency. Since the oxidative desulphurization (ODS) reaction is reported to be endothermic [106], a temperature increase promotes the rate of sulphur removal by accelerating molecular movement and facilitating the reaction dynamics. However, at elevated temperatures, hydrogen peroxide undergoes decomposition, leading to a reduction in oxidant concentration and, consequently, a decrease in the ODS reaction rate [107]. Thus, the optimal temperature for the process was determined experimentally for each catalytic reaction.

It was observed that, at a specific temperature, the oxidative desulphurization (ODS) efficiency for dibenzothiophene initially improved as the oxidant-to-sulphur mass ratio increased to a certain level but subsequently declined when the ratio increased. While higher oxidant concentrations enhanced the dibenzothiophene oxidation yield, excessive oxidant amounts led to the generation of water molecules through decomposition, which could occupy the surface area of the metal-organic framework (MOF) and hinder the adsorption of dibenzothiophene on active sites. Furthermore, economic and environmental considerations necessitate minimizing oxidant usage. Consequently, the model determined the optimal oxidant-to-sulphur ratio for the ODS reaction.

At catalyst-to-sulphur (C/S) ratios ranging from 0.5 to 12 and temperatures between 60 °C and the optimum level, the maximum efficiency of sulphur oxidative desulphurization (ODS) was achieved, corresponding to nearly complete sulphur removal. This indicates that a C/S ratio of 12 optimally increased the concentration of active sites on the metal-organic framework (MOF), thereby enhancing the sulphur oxidation yield. However, excessive amounts of the MOF resulted in particle agglomeration, a reduction in active sites, and limited surface area availability for adsorbate interaction. These factors negatively impacted reactant mass transfer and ultimately reduced the catalytic efficiency of the MOF in the oxidation process [108-109].

The key factors influencing the desulphurization process are the electron density on sulphur atoms and the steric hindrance surrounding them. Oxidative desulphurization (ODS) is more effective with higher electron density and lower steric hindrance. The sulphur atoms in 4,6-dimethyldibenzothiophene (4,6-DMDBT), dibenzothiophene (DBT), and 2-methylbenzothiazole (2-MB) exhibit electron densities of 5.760, 5.758, and 5.739, respectively [110]. Given the comparable electron densities of 4,6-DMDBT and DBT, steric hindrance around the sulphur atom played a significant role in determining oxidation efficiency. Consequently, DBT demonstrated higher conversion rates with UiO-66 derivatives due to its lower steric hindrance compared to the other aromatic

compounds investigated in this study. The reduced activity observed for 4,6-DMDBT can be attributed to its larger molecular size relative to DBT and 2-MB and methyl groups at positions 4 and 6, which limits its interaction primarily to the external surface of the metal-organic frameworks (MOFs) [111]. As a result, the catalytic activity of UiO-66 and its derivatives followed the order: DBT > 2-MB > 4,6-DMDBT.

## 3.3 Parameters Optimization

The optimal reaction conditions for the removal of sulphur-containing compounds from model fuel (MF) were determined using response surface methodology (RSM) based on a central composite design (CCD) model. The optimal values of the three key parameters, aimed at maximizing sulphur removal efficiency and overall desirability, are summarized in Table 5. When multiple responses are optimized simultaneously; in this study, the removal efficiencies of 2-MB, DBT, and 4,6-DMDBT, the individual desirability function transforms each response into a dimensionless score ranging from 0 to 1, where 0 represents a completely unacceptable response and 1 represents the ideal target value. The overall desirability is then calculated as the geometric mean of all individual desirability scores. A desirability value above 0.8 is generally considered acceptable for process optimization purposes [64]. The optimum operating conditions were determined using the desirability function defined in Equation (16) in Section 1.5, which combines the optimization criteria into an overall desirability value ranging from 0 to 1. A desirability value closer to 1 indicates a more favorable combination of the investigated operating parameters and predicted desulphurization response.

Table 5. Obtained optimal values for UiO-66, UiO-66-OH, UiO-66-$NO_2$ and UiO-66-$NH_2$ in achieving highest sulphur removal, standard uncertainties (u) are u (T) = ±1 °C; u (Oxd./Sul. mass ratio) = ±0.01; u (Cat./Sul. mass ratio) = ±0.01; u (yield) = ±0.01

| Catalyst | Optimum Value | | | 2-MB Removal (%) | DBT Removal (%) | 4.6-DMDBT Removal (%) | Desir-ability |
|---|---|---|---|---|---|---|---|
| | Tempera-ture (°C) | Oxd./ Sul.ratio (-) | Cat./ Sul.ratio (-) | | | | |
| UiO-66 | 67.9 | 3.02 | 9.84 | 89.96 | 95.09 | 66.51 | 0.828 |
| UiO-66-OH | 66.8 | 3.21 | 9.71 | 91.26 | 96.94 | 68.90 | 0.883 |
| UiO-66-$NO_2$ | 66.7 | 2.97 | 9.75 | 93.23 | 98.68 | 69.33 | 0.916 |
| UiO-66-$NH_2$ | 72.6 | 1.62 | 11.03 | - | 89.70 | - | 0.897 |

To evaluate the impact of UiO-66 on dibenzothiophene (DBT) removal efficiency, the catalytic oxidative and extractive removal of DBT was analysed both with and without UiO-66 in the presence of $H_2O_2$ in a model fuel. The results demonstrated that sulphur removal was significantly less efficient in the absence of a catalyst, with a removal efficiency of only 34%, compared to 95% when UiO-66 was used under the same conditions (Table 6; O/S = 3.0 (mg/mg) at 68 °C). Furthermore, the highest DBT removal efficiency achieved was 89.70% when UiO-66-$NH_2$ was employed as the catalyst under

specific conditions (72.6 °C temperature, O/S = 1.62 (mg/mg), and C/S = 11.03 (mg/mg)). However, this efficiency was still lower than that observed with UiO-66 [Publication II].

*Table 6. Catalytic oxidative and extractive removal of dibenzothiophene with and without UiO-66 in the presence of $H_2O_2$ (Publication II).*

| | DBT removal at different temperatures (%) | | | |
|---|---|---|---|---|
| | 36 °C | 60 °C | 68 °C | 84 °C |
| UiO-66 | 75 % | 94 % | 95 % | 91 % |
| No catalyst* | 25 % | 32 % | 34 % | 34 % |

* Reaction Condition: 3 mL of MF, 13.1 µL $H_2O_2$ (Oxd./Sul. = 3.0), 3 mL of polar phase, for 150 min.

The recovery of metal-organic frameworks (MOFs) is a critical factor for their industrial application and economic viability. To evaluate the reusability of the synthesized MOFs, four consecutive catalytic oxidation tests were conducted under optimal conditions. After each experiment, the catalyst was separated from the liquid phase via centrifugation, washed with acetonitrile, and dried at 100 °C for 12 hours under atmospheric pressure before being reused in subsequent reactions. The sulphur removal efficiency showed a slight decline of approximately 10% over the four cycles, indicating that the initial dibenzothiophene (DBT) removal efficiency was largely retained. Similarly, the regeneration of UiO-66 catalyst and its derivates were investigated through four sequential DBT removal experiments under optimal conditions [Publication I and Publication II].

## 3.4 Kinetic Modeling

The system of equations was solved simultaneously using the ODE45 function in MATLAB, a numerical solver designed for ordinary differential equations (ODEs). ODE45 is particularly suitable for solving first-order and time-dependent equations, making it suitable for time-dependent kinetic models. The optimal parameter estimation was achieved by minimizing the root mean square error (RMSE) between the model-predicted and experimentally observed species yields. The optimization process was conducted using the genetic algorithm toolbox available in MATLAB. The activation energy and pre-exponential factor for the reactions were determined by applying the reparametrized Arrhenius equation, which can reduce correlation between Arrhenius parameters during estimation by introducing a reference temperature formulation [Publication III].

The oxidation yield of dibenzothiophene improves with increasing reaction temperature above 20 °C. However, beyond an optimal temperature threshold, the oxidation efficiency declines. This behaviour arises because increasing temperature generally accelerates the ODS kinetics (via higher rate constants and improved mass transfer), whereas excessive temperatures promote hydrogen peroxide decomposition, which reduces oxidant availability and consequently diminishes the reaction rate [Publication III].

The experimental and calculated component yields demonstrated the oxidation of dibenzothiophene to form both sulfoxide (DBTO) and sulfone ($DBTO_2$) derivatives when

reacted in the presence of UiO-66-$NO_2$ catalyst. UiO-66-$NO_2$ was selected for detailed kinetic modelling because it exhibited the highest ODS removal among the linker-functionalized UiO-66 catalysts under optimized conditions.

Comparison between experimental observations and kinetic model predictions showed good agreement for both the dibenzothiophene conversion and oxidized product yields [Publication III]. The optimal kinetic parameters were identified with a root mean square error (RMSE) of 10.5%.

## 3.5 Parameters Effects on PODS

The effect of temperature on photocatalytic oxidative desulphurization (PODS) is a critical parameter influencing the overall efficiency of sulphur removal from the model fuel (Figure 16). Although PODS is primarily light-driven rather than strictly "endothermic," moderate increases in temperature can enhance the apparent reaction rate by improving mass transfer and diffusion of reactants/products and by influencing adsorption–desorption equilibria at the photocatalyst surface. Higher temperatures can also affect the formation, mobility, and surface reactions of reactive oxygen species, thereby accelerating oxidation of refractory sulphur compounds within an optimal temperature window. However, excessively high temperatures may have counteracting effects, including promoting electron–hole recombination and increasing desorption of adsorbed reactants, which can offset gains from faster kinetics and reduce overall PODS efficiency.

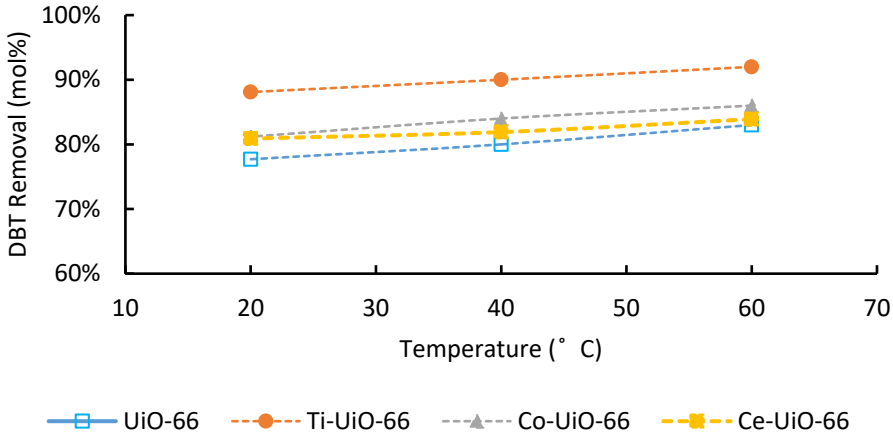



*Figure 16. Effect of reaction temperature on DBT removal over different UiO-66-based catalysts.*

The observed maximum photocatalytic efficiency for dibenzothiophene (DBT) oxidation over the Ti-UiO-66 catalyst under UVA irradiation, as compared to UV-visible irradiation and UVC, is attributed to an optimal synergy between the photon energy of the excitation source and the electronic structure of the metal-organic framework (MOF), which promotes efficient photoexcitation and charge separation while limiting non-productive high-energy pathways.

Among the investigated pristine and metal-modified UiO-66 catalysts, Ti-UiO-66 exhibited the highest DBT removal efficiency and was among the best-performing catalysts for 4,6-DMDBT under the investigated conditions. Therefore, Ti-UiO-66 was

selected as the most promising photocatalyst for the subsequent detailed evaluation of irradiation conditions, reaction time, and airflow rate.

The efficiency of Ti-UiO-66 in PODS was subsequently evaluated under different UV irradiation conditions. Ti-UiO-66 is primarily photoactive in the near-UV region, and UVA wavelengths (315–400 nm; photon energy ≈ 3.1–3.9 eV) can overlap with the absorption edge/band-gap-related excitation of UiO-66-type materials (reported band gaps on the order of ~3.6 eV for UiO-66 derivatives), thereby generating electron–hole pairs required for photocatalysis [112]. Under UVA irradiation, the photon energy is sufficient to activate the Ti-UiO-66 photocatalyst efficiently, promoting the formation of reactive species that drive the oxidative desulphurization of DBT. In contrast, UVC irradiation, while higher in energy, can increase non-selective excitation and thermalization losses and may accelerate charge-carrier recombination and/or surface degradation pathways in some photocatalytic systems, leading to lower overall efficiency. Broad UV–visible irradiation may yield lower DBT removal than UVA if a substantial fraction of the emitted photons lies outside the effective absorption window of Ti-UiO-66 (e.g., in the visible region), reducing the usable photon flux at the catalyst's absorption edge and thus lowering the overall activity relative to targeted UVA illumination.

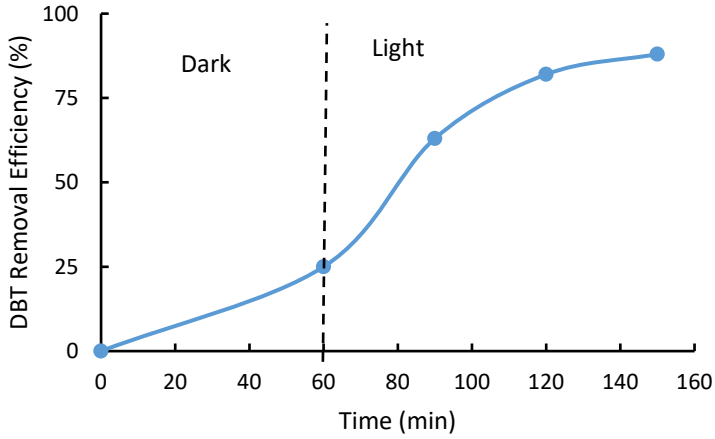



*Figure 17. DBT removal over time for Ti-UiO-66 in the photocatalytic reactor.*

Figure 17 shows the trend of DBT removal over time for Ti-UiO-66 after the suspension was kept in the dark for 60 min to establish adsorption–desorption equilibrium on the photocatalyst surface prior to irradiation. This dark equilibration step is commonly used in photocatalysis to separate adsorption from the subsequent light-driven reaction.

In our investigation of dibenzothiophene (DBT) removal over Ti-UiO-66 in a photocatalytic reactor, the influence of oxidant (air) flow rate on the efficiency of photocatalytic oxidative desulphurization was systematically evaluated. The results demonstrate that increasing the air flow rate enhances DBT removal efficiency up to a threshold value of 150 mL/min (Figure 18).

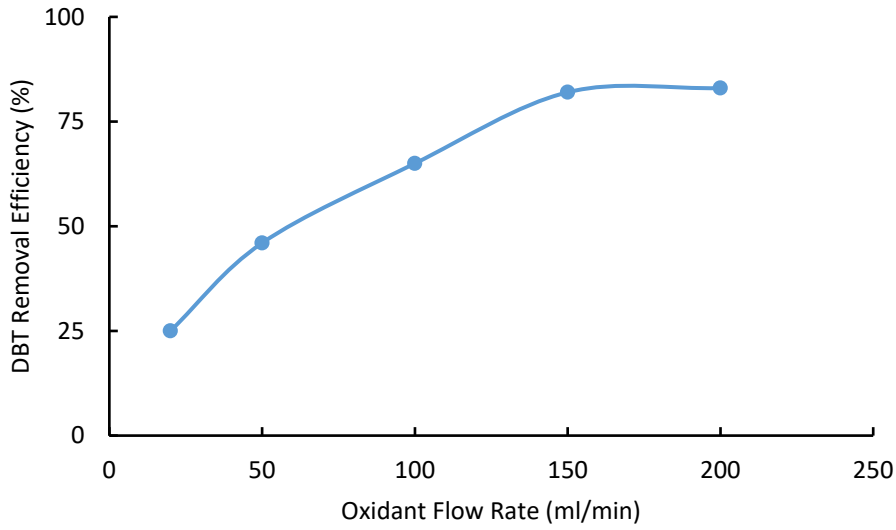
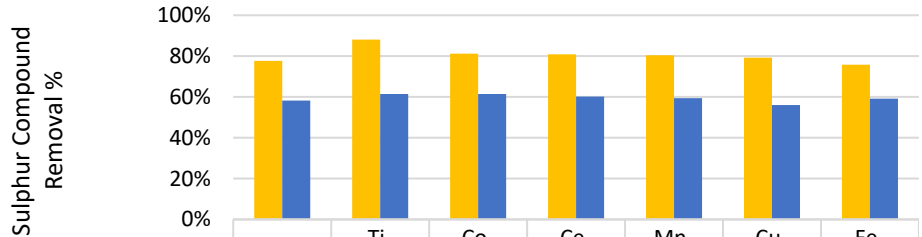



*Figure 18. The effect of oxidant flow rate on DBT removal for Ti-UiO-66 in the photocatalytic reactor.*

This improvement can be attributed to the greater availability of molecular oxygen, which acts as an electron acceptor and facilitates the generation of reactive oxygen species such as superoxide radicals ($O_2\bullet^-$) and hydroxyl radicals (•OH) on the photocatalyst surface. These species are crucial for the oxidative degradation of DBT into more polar, extractable compounds.

However, when the air flow rate exceeded 150 mL/min, no further increase in DBT removal was observed, as the efficiency plateaued between 150 and 200 mL/min. This phenomenon suggests that, beyond a certain point, the photocatalytic system becomes saturated with oxygen, and the overall reaction rate is no longer limited by oxidant availability.




| | UiO-66 | Ti-UiO-66 | Co-UiO-66 | Ce-UiO-66 | Mn-UiO-66 | Cu-UiO-66 | Fe-UiO-66 |
|---|---|---|---|---|---|---|---|
| DBT Removal | 77.7% | 88.1% | 81.2% | 80.9% | 80.4% | 79.2% | 75.8% |
| 4,6 DMDBT Removal | 58.2% | 61.4% | 61.4% | 60.2% | 59.4% | 56.0% | 59.2% |

*Figure 19. Sulphur-compound removal by pristine and metal-modified UiO-66 at the selected air flow rate of 150 mL min$^{-1}$.*

At the selected air-flow rate of 150 mL min$^{-1}$, comparison of pristine and metal-modified UiO-66 materials (Figure 19) showed that Ti-UiO-66 gave the highest removal

of both DBT and 4,6-DMDBT among the screened photocatalysts. Ce-, Co-, Cu-, Fe-, and Mn-modified and pristine UiO-66 materials showed lower removal under the same conditions. Ti incorporation can alter light absorption, charge separation, defect chemistry, and oxygen activation; the present performance trend is consistent with these effects, although assigning a single dominant mechanism would require dedicated photophysical measurements.

In our comparative experiments, oxidative desulphurization (ODS) of DBT using UiO-66-$NO_2$ with $H_2O_2$ as the oxidant showed markedly higher removal than photocatalytic oxidative desulphurization (PODS) using Ti–UiO-66 with air as the oxidant (92% DBT conversion). This performance gap is consistent with fundamental mechanistic differences; in ODS the external $H_2O_2$ can supply highly reactive oxidizing species and can interact with Lewis-acidic Zr sites in UiO-66-type frameworks, enabling rapid oxidation of DBT to sulfoxides/sulfones prior to extraction [113]. By contrast, PODS with Ti-containing UiO-66 must first generate reactive oxygen species from molecular $O_2$ via photo-induced charge separation ($e^-/h^+$). This route is intrinsically limited by (i) the rate of $O_2$ activation, (ii) charge-carrier recombination, and (iii) gas–liquid transport constraints (including finite $O_2$ solubility and mass transfer in hydrocarbon media) [114].

# 4 Conclusions

The current study focused on oxidative desulphurization (ODS) using metal-organic framework (MOF) materials as catalysts. To this end, UiO-66 and its functional derivatives were synthesized via solvothermal methods, chosen for their ability to produce highly crystalline and thermally stable MOF structures under controlled temperature and pressure conditions. Prior to catalytic evaluation, the synthesized materials were thoroughly characterized to confirm successful synthesis and to establish structure-property relationships relevant to their catalytic performance. A comprehensive suite of analytical techniques, including Fourier Transform Infrared Spectroscopy (FTIR), proton Nuclear Magnetic Resonance ($^1$H NMR), X-ray Diffraction (XRD), Scanning Electron Microscopy (SEM), Thermogravimetric Analysis (TGA), Brunauer-Emmett-Teller (BET) surface area analysis, and Microwave Plasma Atomic Emission Spectroscopy (MP-AES), was employed to elucidate the structural and physicochemical properties of the prepared catalysts.

To optimize the oxidative desulphurization (ODS) process, Response Surface Methodology (RSM) and Central Composite Design (CCD) were utilized. These statistical approaches allowed for the systematic evaluation of key reaction parameters, including temperature ($X_1$), oxidant-to-sulphur mass ratio ($X_2$) and MOF-to-sulphur mass ratio ($X_3$), on the ODS efficiency. The statistical analysis yielded F-values and coefficients of determination ($R^2$) that demonstrated a strong correlation between experimental results and model predictions, validating the robustness of the experimental design.

The ODS performance was evaluated using model sulphur compounds, including dibenzothiophene (DBT), 2-methylbenzothiazole (2-MB), and 4,6-dimethyldibenzothiophene (4,6-DMDBT), at 1000 ppm sulphur content in model fuel (MF). Under optimized conditions (66-68 °C, oxidant-to-sulphur ratio of 3.0-3.2, and catalyst-to-sulphur ratio of 9.7-9.8), the sulphur removal efficiencies exceeded 95%, 90%, and 67% for DBT, 2-MB, and 4,6-DMDBT, respectively, across the three MOFs tested.

Among the linker-functionalized UiO-66 materials examined, UiO-66-$NO_2$ showed the highest deep-ODS performance under the investigated conditions. Reuse tests demonstrated gradual but limited activity loss over four cycles. These findings establish a comparative performance trend for the tested catalyst set; they do not by themselves prove a single molecular origin for the activity difference, which likely reflects combined electronic, acid–base, transport, and defect effects.

The complex-reaction kinetic model provided a systematic description of DBT adsorption, sequential oxidation to sulfoxide/sulfone species, and product removal over UiO-66-$NO_2$. Parameter estimation and MCMC analysis quantified kinetic uncertainty and supported agreement between model predictions and the experimental data within the studied temperature range [Publication III].

In PODS screening, Ti-UiO-66 gave the highest removal of DBT and 4,6-DMDBT among the tested pristine and metal-modified UiO-66 materials. Subsequent experiments identified UVA irradiation and an air-flow rate around 150 mL min$^{-1}$ as favourable within the investigated domain. Although peroxide-assisted ODS achieved higher deep-desulphurization performance, the air/UV PODS results demonstrate the feasibility of oxidant-lean photocatalytic sulphur removal and identify Ti-UiO-66 as the most promising material of the screened series.

# List of Figures

Figure 1. Molecular structures of the model sulphur compounds employed in this study: dibenzothiophene (DBT), 2-methylbenzothiazole (2-MB), and 4,6-dimethyldibenzothiophene (4,6-DMDBT). ..... 15
Figure 2. Schematic showing BDC-based linker functionalization and the corresponding UiO-66 materials investigated in this work: UiO-66 (BDC), UiO-66-$NO_2$ ($NO_2$–BDC), and UiO-66-OH (OH–BDC). The molecular linker structures are chemically explicit; the framework drawing is schematic. ..... 17
Figure 3. Schematic of Experimental System used for Oxidative Desulphurization ..... 28
Figure 4. Photocatalytic reactor set-up using LED strip; The reactor consists of a double-jacket glass vessel through which temperature-controlled water is circulated. A mechanical agitator is positioned at the centre of the reactor to ensure homogeneous mixing. An inlet tube is provided for oxidant (air) introduction into the reaction medium. The LED strip is arranged around the outer jacket to provide uniform irradiation to the reaction mixture. ..... 29
Figure 5. XRD powder patterns of UiO-67, UiO-66, UiO-66-$NH_2$, UiO-66-OH, and UiO-66-$NO_2$ ..... 33
Figure 6. XRD powder patterns of solvothermal metal doped on UiO-66 ..... 34
Figure 7. FTIR spectra of UiO-66 and the linker-functionalized UiO-66-$NH_2$, UiO-66-$NO_2$, and UiO-66-OH materials. ..... 35
Figure 8. FTIR spectra of Ti-UiO-66, Fe-UiO-66 and Co-UiO-66. ..... 36
Figure 9. FTIR spectra of Cu-UiO-66 and Mn-UiO-66 ..... 36
Figure 10. SEM micrographs arranged as a single aligned high-resolution panel: (a) UiO-66, (b) UiO-66-$NH_2$ (c), UiO-66-OH, (d) UiO-66-$NO_2$, (e) Ce-UiO-66, (f) Ti-UiO-66, (g) Cu-UiO-66, (h) Mn-UiO-66 ..... 38
Figure 11. $^1$H NMR spectra of digested (a) UiO-66 and (b) UiO-66-OH in NaOD/$D_2O$. The labelled resonances correspond to aromatic protons of BDC- and hydroxy-substituted BDC-derived species in the digested samples. ..... 39
Figure 12. TGA curves of UiO-66, UiO-66-OH, and UiO-66-$NO_2$, showing the main mass-loss regions associated with removal of adsorbed species ($\Delta m_1$), residual solvent ($\Delta m_2$), and framework decomposition ($\Delta m_3$), $\Delta m_1 \approx 3$–5 wt.%, $\Delta m_2 \approx 10$–15 wt.%, $\Delta m_3 \approx 40$–45 wt.% (Publication II). ..... 40
Figure 13. Thermogravimetric curves of metal-modified UiO-66 samples. Curves are vertically offset for clarity; ordinate values represent mass (%) plus the plotting offset. ..... 41
Figure 14. X-ray photoelectron spectroscopy (XPS) spectra of the Zr 3d region for UiO-66 and its derivatives. The peaks correspond to the spin–orbit doublet of Zr $3d_{5/2}$ and Zr $3d_{3/2}$ components associated with the Zr(IV)–O coordination environment in the UiO-66 framework (typical splitting ≈ 2.4 eV) ..... 42
Figure 15. Nitrogen adsorption–desorption/BET textural analysis of the synthesized UiO-66-based materials. ..... 44
Figure 16. Effect of reaction temperature on DBT removal over different UiO-66-based catalysts. ..... 48
Figure 17. DBT removal over time for Ti-UiO-66 in the photocatalytic reactor ..... 49
Figure 18. The effect of oxidant flow rate on DBT removal for Ti-UiO-66 in the photocatalytic reactor ..... 50

Figure 19. Sulphur-compound removal by pristine and metal-modified UiO-66 at the selected air flow rate of 150 mL $min^{-1}$. ..... 50

# List of Tables

Table 1. Experimental ingredient amount and condition for the synthesis of UiO-66 derivatives ..... 25
Table 2. Experimental ingredient amount and condition for the synthesis of metal UiO-66 derivatives ..... 26
Table 3. Independent test variables at five levels were used in the central composite design for four different MOFs, UiO-66(Zr), UiO-66-OH, UiO-66-$NO_2$ and UiO-66-$NH_2$ . 32
Table 4. Zirconium content and textural properties of the synthesized MOFs ..... 43
Table 5. Obtained optimal values for UiO-66, UiO-66-OH, UiO-66-$NO_2$ and UiO-66-$NH_2$ in achieving highest sulphur removal, standard uncertainties (u) are u (T) = ±1 °C; u (Oxd./Sul. mass ratio) = ±0.01; u (Cat./Sul. mass ratio) = ±0.01; u (yield) = ±0.01..... 46
Table 6. Catalytic oxidative and extractive removal of dibenzothiophene with and without UiO-66 in the presence of $H_2O_2$ (Publication II) ..... 47

# References


1. Li, S. S., & Sun, L. B. (2020). Controllable fabrication of cuprous sites in confined spaces for efficient adsorptive desulphurization. Fuel, 259, 116221. https://doi.org/10.1016/j.fuel.2019.116221
2. Karimi, R., & Golmohammadi, B. (2024). Simulation and optimization of heavy fuel oil (HFO) refining platform to low sulphur marine fuel (LS-FO) by oxidative desulphurization. Scientific Reports, 14(1), 29830. https://doi.org/10.1038/s41598-024-81242-z
3. Bhadra, B. N., & Jhung, S. H. (2019). Oxidative desulphurization and denitrogenation of fuels using metal-organic framework-based/-derived catalysts. Applied Catalysis B: Environmental, 259, 118021. https://doi.org/10.1016/j.apcatb.2019.118021
4. Viana, A. M., Ribeiro, S. O., Castro, B. D., Balula, S. S., & Cunha-Silva, L. (2019). Influence of UiO-66 (Zr) preparation strategies in its catalytic efficiency for desulphurization process. Materials, 12(18), 3009. https://doi.org/10.3390/ma12183009
5. Zhang, X., Huang, P., Liu, A., & Zhu, M. (2017). A metal–organic framework for oxidative desulphurization: UIO-66 (Zr) as a catalyst. Fuel, 209, 417-423. https://doi.org/10.1016/j.fuel.2017.08.025
6. Liao, M., Xiao, Y., Pi, X., Zhang, L., Zheng, M., Liu, J., Wu, H. and Guo, J., (2024). Zr-Based Metal–Organic Framework (UiO-66) Doped with Rare-Earth Element (La, Y)-Supported Polyoxometalate Liquid for Oxidative Desulphurization of Dibenzothiophene Oxidation. Energy & Fuels, 38(14), 12555-12568. https://doi.org/10.1021/acs.energyfuels.4c01125
7. Liao, X., Wang, X., Wang, F., Yao, Y., & Lu, S. (2021). Ligand modified metal organic framework UiO-66: A highly efficient and stable catalyst for oxidative desulphurization. Journal of Inorganic and Organometallic Polymers and Materials, 31(2), 756-762. https://doi.org/10.1007/s10904-020-01808-y
8. Yin, J., Fu, W., Zhang, J., Liu, X., Zhang, X., Wang, C., He, J., Jiang, W., Li, H. and Li, H. (2023). UiO-66 (Zr)-based porous ionic liquids for highly efficient extraction coupled catalytic oxidative desulphurization. Chemical Engineering Journal, 470, 144290. https://doi.org/10.1016/j.cej.2023.144290
9. Barghi, B., Niidu, A., & Karimzadeh, R. (2021). The effect of water and zinc loading on LPG catalytic cracking for light olefin production using response surface methodology. Proceedings of the Estonian Academy of Sciences, 70(2), 135–147. https://doi.org/10.3176/proc.2021.2.01
10. Shafiq, I., Shafique, S., Akhter, P., Yang, W., & Hussain, M. (2022). Recent developments in alumina-supported hydrodesulphurization catalysts for the production of sulphur-free refinery products: A technical review. Catalysis Reviews, 64(1), 1–86. https://doi.org/10.1080/01614940.2020.1780824
11. Zhang, Y., Wang, X., Li, H., & Liu, C. (2024). Effective reduction of hydrogen consumption in ultra-deep hydrodesulphurization of diesel: Insights into thermodynamic limitations during hydrotreating. Fuel, 356, 129640. https://doi.org/10.1016/j.fuel.2023.129640

12. Liu, Y., Wang, H., Zhao, J., Liu, Y., & Liu, C. (2019). Ultra-deep desulphurization by reactive adsorption desulphurization on copper-based catalysts. Journal of Energy Chemistry, 29, 8–17. https://doi.org/10.1016/j.jechem.2018.01.016
13. Rajendran, A., Cui, T. Y., Fan, H. X., Yang, Z. F., Feng, J., & Li, W. Y. (2020). A comprehensive review on oxidative desulphurization catalysts targeting clean energy and environment. Journal of Materials Chemistry A, 8(5), 2246–2285. https://doi.org/10.1039/C9TA12555H
14. Kang, L., Liu, H., He, H., & Yang, C. (2018). Oxidative desulphurization of dibenzothiophene using molybdenum catalyst supported on Ti-pillared montmorillonite and separation of sulfones by filtration. Fuel, 234, 1229–1237. https://doi.org/10.1016/j.fuel.2018.07.148
15. Gu, Q., Wen, G., Ding, Y., Wu, K. H., Chen, C., & Su, D. (2017). Reduced graphene oxide: A metal-free catalyst for aerobic oxidative desulphurization. Green Chemistry, 19(4), 1175–1181. https://doi.org/10.1039/C6GC02894B
16. Bagheri, M., Masoomi, M. Y., & Morsali, A. (2017). A MoO3–metal–organic framework composite as a simultaneous photocatalyst and catalyst in the PODS process of light oil. ACS Catalysis, 7(10), 6949–6956. https://doi.org/10.1021/acscatal.7b02581
17. Zhu, W., Huang, W., Li, H., Zhang, M., Jiang, W., Chen, G., & Han, C. (2011). Polyoxometalate-based ionic liquids as catalysts for deep desulphurization of fuels. Fuel Processing Technology, 92(10), 1842–1848. https://doi.org/10.1016/j.fuproc.2011.04.030
18. Miao, G., Huang, D., Ren, X., Li, X., Li, Z., & Xiao, J. (2016). Visible-light induced photocatalytic oxidative desulphurization using BiVO4/C3N4@$SiO_2$ with air/cumene hydroperoxide under ambient conditions. Applied Catalysis B: Environmental, 192, 72–79. https://doi.org/10.1016/j.apcatb.2016.03.033
19. Sadare, O. O., & Daramola, M. O. (2023). Bio-catalytic degradation of dibenzothiophene (DBT) in petroleum distillate (diesel) by Pseudomonas spp. Scientific Reports, 13, 6020. https://doi.org/10.1038/s41598-023-31951-8
20. Grossman, M. J., Lee, M. K., Prince, R. C., Minak-Bernero, V., George, G. N., & Pickering, I. J. (2001). Deep desulphurization of extensively hydrodesulphurized middle distillate oil by Rhodococcus sp. strain ECRD-1. Applied and Environmental Microbiology, 67(4), 1949–1952. https://doi.org/10.1128/AEM.67.4.1949-1952.2001
21. Lee, K. X., & Valla, J. A. (2019). Adsorptive desulphurization of liquid hydrocarbons using zeolite-based sorbents: A comprehensive review. Reaction Chemistry & Engineering, 4(8), 1357–1386. https://doi.org/10.1039/C9RE00036A
22. Boshagh, F., Rahmani, M., & Zhu, W. (2022). Recent advances and challenges in developing technological methods assisting oxidative desulphurization of liquid fuels: A review. Energy & Fuels, 36(21), 12961–12985. https://doi.org/10.1021/acs.energyfuels.2c02387
23. Gao, Y., Gao, R., Zhang, G., Zheng, Y., & Zhao, J. (2018). Oxidative desulphurization of model fuel in the presence of molecular oxygen over polyoxometalate-based catalysts supported on carbon nanotubes. Fuel, 224, 261–270. https://doi.org/10.1016/j.fuel.2018.03.034
24. Mokhtar, W. N. A. W., Bakar, W. A. W. A., Ali, R., & Kadir, A. A. A. (2015). Optimization of oxidative desulphurization of Malaysian Euro II diesel fuel utilizing

tert-butyl hydroperoxide–dimethylformamide system. Fuel, 161, 26–33. https://doi.org/10.1016/j.fuel.2015.08.031
25. Jiang, X., Li, H., Zhu, W., He, L., Shu, H., & Lu, J. (2009). Deep desulphurization of fuels catalyzed by surfactant-type decatungstates using $H_2O_2$ as oxidant. Fuel, 88(3), 431–436. https://doi.org/10.1016/j.fuel.2008.11.010
26. Zheng, H. Q., Zeng, Y. N., Chen, J., Lin, R. G., Zhuang, W. E., Cao, R., & Lin, Z. J. (2019). Zr-based metal–organic frameworks with intrinsic peroxidase-like activity for ultradeep oxidative desulphurization: Mechanism of $H_2O_2$ decomposition. Inorganic Chemistry, 58(10), 6983–6992. https://doi.org/10.1021/acs.inorgchem.9b00604
27. Hao, L., Hurlock, M. J., Ding, G., & Zhang, Q. (2020). Metal–organic frameworks towards desulphurization of fuels. Topics in Current Chemistry, 378(1), 175–202. https://doi.org/10.1007/s41061-020-0280-1
28. Leng, K., Sun, Y., Zhang, X., Yu, M., & Xu, W. (2016). Ti-modified hierarchical mordenite as highly active catalyst for oxidative desulphurization of dibenzothiophene. Fuel, 174, 9–16. https://doi.org/10.1016/j.fuel.2016.01.070
29. Shi, Y., Liu, G., Zhang, B., & Zhang, X. (2016). Oxidation of refractory sulphur compounds with molecular oxygen over a Ce–Mo–O catalyst. Green Chemistry, 18(19), 5273–5279. https://doi.org/10.1039/C6GC01357K
30. Wu, P., Zhu, W., Chao, Y., Zhang, J., Zhang, P., Zhu, H., & Dai, S. (2016). A template-free solvent-mediated synthesis of high surface area boron nitride nanosheets for aerobic oxidative desulphurization. Chemical Communications, 52(1), 144–147. https://doi.org/10.1039/C5CC07830J
31. Jung, B. K., & Jhung, S. H. (2015). Adsorptive removal of benzothiophene from model fuel, using modified activated carbons, in presence of diethylether. Fuel, 145, 249–255. https://doi.org/10.1016/j.fuel.2014.12.088
32. Serrano, D. P., Sanz, R., Pizarro, P., Moreno, I., & Medina, S. (2014). Hierarchical TS-1 zeolite as an efficient catalyst for oxidative desulphurization of hydrocarbon fractions. Applied Catalysis B: Environmental, 146, 35–42. https://doi.org/10.1016/j.apcatb.2013.05.025
33. Piscopo, C. G., Granadeiro, C. M., Balula, S. S., & Bošković, D. (2020). Metal-organic framework-based catalysts for oxidative desulphurization. ChemCatChem, 12(19), 4721–4731. https://doi.org/10.1002/cctc.202000688
34. Bhadra, B. N., & Jhung, S. H. (2019). Oxidative desulphurization and denitrogenation of fuels using metal-organic framework-based/-derived catalysts. Applied Catalysis B: Environmental, 259, 118021. https://doi.org/10.1016/j.apcatb.2019.118021
35. Smolders, S., Willhammar, T., Krajnc, A., Sentosun, K., Wharmby, M. T., Lomachenko, K. A., Bals, S., Mali, G., Roeffaers, M. B. J., De Vos, D. E., & Bueken, B. (2019). A titanium(IV)-based metal–organic framework featuring defect-rich Ti-O sheets as an oxidative desulphurization catalyst. Angewandte Chemie International Edition, 58(27), 9160–9165. https://doi.org/10.1002/anie.201904347
36. Lawson, H. D., Walton, S. P., & Chan, C. (2021). Metal–organic frameworks for drug delivery: A design perspective. ACS Applied Materials & Interfaces, 13(6), 7004–7020. https://doi.org/10.1021/acsami.1c01089
37. Sun, Y., Wang, L., Amer, W. A., Yu, H., Ji, J., Huang, L., Shan, J., & Tong, R. (2013). Hydrogen storage in metal-organic frameworks. Journal of Inorganic and

Organometallic Polymers and Materials, 23(2), 270–285. https://doi.org/10.1007/s10904-012-9779-4

38. Leelasree, T., Selamneni, V., Akshaya, T., Sahatiya, P., & Aggarwal, H. (2020). MOF based flexible, low-cost chemiresistive device as a respiration sensor for sleep apnea diagnosis. Journal of Materials Chemistry B, 8(45), 10182–10191. https://doi.org/10.1039/D0TB01748E
39. Liu, M., Wu, J., & Hou, H. (2019). Metal–organic framework (MOF)-based materials as heterogeneous catalysts for C–H bond activation. Chemistry – A European Journal, 25(12), 2935–2948. https://doi.org/10.1002/chem.201804149
40. Poonia, K., Patial, S., Raizada, P., Ahamad, T., Khan, A. A. P., Le, Q. V., Nguyen, V. H., Hussain, C. M., & Singh, P. (2023). Recent advances in metal-organic framework (MOF)-based hierarchical composites for water treatment by adsorptional photocatalysis: A review. Environmental Research, 222, 115349. https://doi.org/10.1016/j.envres.2023.115349
41. Wu, T., Prasetya, N., & Li, K. (2020). Recent advances in aluminium-based metal-organic frameworks (MOF) and its membrane applications. Journal of Membrane Science, 615, 118493. https://doi.org/10.1016/j.memsci.2020.118493
42. Wu, H., Yildirim, T., & Zhou, W. (2013). Exceptional mechanical stability of highly porous zirconium metal–organic framework UiO-66 and its important implications. The Journal of Physical Chemistry Letters, 4(6), 925–930. https://doi.org/10.1021/jz4002345
43. Bozbiyik, B., Duerinck, T., Lannoeye, J., De Vos, D. E., Baron, G. V., & Denayer, J. F. (2014). Adsorption and separation of n-hexane and cyclohexane on the UiO-66 metal–organic framework. Microporous and Mesoporous Materials, 183, 143–149. https://doi.org/10.1016/j.micromeso.2013.07.035
44. Kandiah, M., Nilsen, M. H., Usseglio, S., Jakobsen, S., Olsbye, U., Tilset, M., Larabi, C., Quadrelli, E. A., Bonino, F., & Lillerud, K. P. (2010). Synthesis and stability of tagged UiO-66 Zr-MOFs. Chemistry of Materials, 22(24), 6632–6640. https://doi.org/10.1021/cm102601v
45. Safa, M. A., Bouresli, R., Al-Majren, R., Al-Shamary, T., & Ma, X. (2019). Oxidative desulphurization kinetics of refractory sulphur compounds in hydrotreated middle distillates. Fuel, 239, 24–31. https://doi.org/10.1016/j.fuel.2018.10.141
46. Kayedi, N., Samimi, A., Bajgirani, M. A., & Bozorgian, A. (2021). Enhanced oxidative desulphurization of model fuel: A comprehensive experimental study. South African Journal of Chemical Engineering, 35, 153–160. https://doi.org/10.1016/j.sajce.2020.09.001
47. De Filippis, P., & Scarsella, M. (2003). Oxidative desulphurization: Oxidation reactivity of sulphur compounds in different organic matrixes. Energy & Fuels, 17(6), 1452–1455. https://doi.org/10.1021/ef0202539
48. Zhao, D., Sun, Z., Li, F., Liu, R., & Shan, H. (2008). Oxidative desulphurization of thiophene catalyzed by (C4H9)4NBr·2C6H11NO coordinated ionic liquid. Energy & Fuels, 22(5), 3065–3069. https://doi.org/10.1021/ef800162w
49. Wei, S., He, H., Cheng, Y., Yang, C., Zeng, G., & Qiu, L. (2016). Performances, kinetics and mechanisms of catalytic oxidative desulphurization from oils. RSC Advances, 6(103), 103253–103266. https://doi.org/10.1039/C6RA22358C
50. Murzin, D. Y., & Salmi, T. (2005). Catalytic kinetics. Elsevier. https://doi.org/10.1016/B978-0-444-63753-6.00004-X

51. Barghi, B., & Karimzadeh, R. (2015). Kinetic modeling based on complex reaction theory for n-butane catalytic cracking over HZSM-5. Reaction Kinetics, Mechanisms and Catalysis, 116(2), 507–521. https://doi.org/10.1007/s11144-015-0918-0
52. Barghi, B., & Karimzadeh, R. (2017). Modeling of ZnZSM-5 deactivation during liquefied petroleum gas catalytic cracking in the presence of steam. Reaction Kinetics, Mechanisms and Catalysis, 120(2), 753–769. https://doi.org/10.1007/s11144-016-1126-2
53. Dhir, S., Uppaluri, R., & Purkait, M. K. (2009). Oxidative desulphurization: Kinetic modelling. Journal of Hazardous Materials, 161(2–3), 1360–1368. https://doi.org/10.1016/j.jhazmat.2008.04.099
54. Horiuti, J., & Nakamura, T. (1957). Stoichiometric number and the theory of steady reaction. Zeitschrift für Physikalische Chemie, 11(5–6), 358–378. https://doi.org/10.1524/zpch.1957.11.5_6.358
55. Murzin, D. (2020). Requiem for the rate-determining step in complex heterogeneous catalytic reactions? Reactions, 1(1), 37–46. https://doi.org/10.3390/reactions1010004
56. Xing, Z., Bishop, N., Leister, K., & Li, Z. J. (2010). Modeling kinetics of a large-scale fed-batch CHO cell culture by Markov chain Monte Carlo method. Biotechnology Progress, 26(1), 208–216. https://doi.org/10.1002/btpr.284
57. Matveyeva, A. N., Wärnå, J., Pakhomov, N. A., & Murzin, D. (2020). Kinetic modeling of isobutane dehydrogenation over Ga2O3/Al2O3 catalyst. Chemical Engineering Journal, 381, 122741. https://doi.org/10.1016/j.cej.2019.122741
58. Murzin, D. Y., Saleem, F., Warnå, J., & Salmi, T. (2020). Kinetic modelling of heterogeneous catalytic oxidation of furfural with hydrogen peroxide to succinic acid. Chemical Engineering Journal, 382, 122811. https://doi.org/10.1016/j.cej.2019.122811
59. Doluda, V. Y., Wärnå, J., Aho, A., Bykov, A., Sidorov, A., Sulman, E. M., Bronstein, L. M., Salmi, T., & Murzin, D. (2013). Kinetics of lactose hydrogenation over ruthenium nanoparticles in hypercrosslinked polystyrene. Industrial & Engineering Chemistry Research, 52(39), 14066–14075. https://doi.org/10.1021/ie401778y
60. Jiang, Q., Yan, X., & Huang, B. (2019). Data-driven batch-end quality modeling and monitoring based on optimized sparse partial least squares. IEEE Transactions on Industrial Electronics, 67(5), 4098–4107. https://doi.org/10.1109/TIE.2019.2916394
61. Shah, A. S., Nasir, H., Fayaz, M., Lajis, A., & Shah, A. (2019). A review on energy consumption optimization techniques in IoT based smart building environments. Information, 10(3), 108. https://doi.org/10.3390/info10030108
62. Gregor, M., Perichta, P., & Džubáková, M. (2023). Design of simulation experiments using central composite design. Acta Simulatio, 9(2), 21–25. https://doi.org/10.22306/asim.v9i2.99
63. Ferreira, S. L. C., Bruns, R. E., Ferreira, H. S., Matos, G. D., David, J. M., Brandão, G. C., da Silva, E. G. P., Portugal, L. A., dos Reis, P. S., Souza, A. S., & dos Santos, W. N. L. (2007). Box-Behnken design: An alternative for the optimization of analytical methods. Analytica Chimica Acta, 597(2), 179–186. https://doi.org/10.1016/j.aca.2007.07.011

64. Bezerra, M. A., Santelli, R. E., Oliveira, E. P., Villar, L. S., & Escaleira, L. A. (2008). Response surface methodology (RSM) as a tool for optimization in analytical chemistry. Talanta, 76(5), 965–977. https://doi.org/10.1016/j.talanta.2008.05.019
65. Bashir, M. J. K., Aziz, H. A., Yusoff, M. S., & Adlan, M. N. (2015). Wastewater treatment processes optimization using response surface methodology (RSM) compared with conventional methods: Review and comparative study. *Middle-East Journal of Scientific Research, 23*(2), 244–252. https://doi.org/10.5829/idosi.mejsr.2015.23.02.9316
66. Yolmeh, M., & Jafari, S. M. (2017). Applications of response surface methodology in the food industry processes. Food and Bioprocess Technology, 10(3), 413–433. https://doi.org/10.1007/s11947-016-1855-2
67. Shah, N., & Mishra, P. (2013). Oil production optimization: A mathematical model. Journal of Petroleum Exploration and Production Technology, 3(1), 37–42. https://doi.org/10.1007/s13202-012-0043-9
68. Hamzaoui, O., Georger, J. F., Monnet, X., Ksouri, H., Maizel, J., Richard, C., & Teboul, J. L. (2008). Effects of changes in vascular tone on the agreement between pulse contour and transpulmonary thermodilution cardiac output measurements within an up to 6-hour calibration-free period. Critical Care Medicine, 36(2), 434–440. https://doi.org/10.1097/01.CCM.0000300278.02037.1D
69. Jiang, W., Zhang, Y., Wang, L., Liu, Y., & Li, H. (2023). Optimization of the esterification of oleic acid and ethanol in a fixed bed membrane reactor by response surface method. Fuel, 342, 127867. https://doi.org/10.1016/j.fuel.2023.127867
70. Kim, J., Kim, D. G., & Ryu, K. H. (2023). Enhancing response surface methodology through coefficient clipping based on prior knowledge. Processes, 11(12), 3392. https://doi.org/10.3390/pr11123392
71. Vijayanand, M., Elayaperumal, A., Senthilkumar, M., & Parthiban, A. (2022). Process modeling and intuitive search-based optimization of average surface roughness in citrate stabilized electroless nickel-boron coatings. JOM, 74(2), 563–573. https://doi.org/10.1007/s11837-021-05072-4
72. Mahmoud, R. M. A., El-Sheshtawy, H. S., El-Hosainy, H. M., & El-Kemary, M. (2023). Sonochemical synthesis of heterostructured ZnO/Bi2O3 for photocatalytic desulphurization. Scientific Reports, 13(1), 19391. https://doi.org/10.1038/s41598-023-46344-0
73. Hamza, Z. A., Dawood, J. J., & Jabbar, M. A. (2024). Ag/Mo doping for enhanced photocatalytic activity of titanium (IV) dioxide during fuel desulphurization. Molecules, 29(19), 4603. https://doi.org/10.3390/molecules29194603
74. Li, C. J., Wang, J. L., Li, Y., & Yu, G. (2015). Study on desulphurization and denitrification by modified activated carbon fibers with visible-light photocatalysis. Journal of Fuel Chemistry and Technology, 43(12), 1516–1522. https://doi.org/10.1016/S1872-5813(16)60002-3
75. Ahmed, I., & Jhung, S. H. (2016). Adsorptive desulphurization and denitrogenation using metal-organic frameworks. Journal of Hazardous Materials, 301, 259–276. https://doi.org/10.1016/j.jhazmat.2015.08.045
76. Chen, Z., Ling, L., Wang, B., Fan, L., & Li, R. (2016). Adsorptive desulphurization with metal-organic frameworks: A density functional theory investigation. Applied Surface Science, 387, 483–490. https://doi.org/10.1016/j.apsusc.2016.06.040

77. Park, J., Kim, H., Lee, J., & Kim, J. (2024). Radical-mediated oxidative desulphurization of dibenzothiophene in a chromophore-enhanced photocatalytic system. Journal of Photochemistry and Photobiology A: Chemistry, 456, 115854. https://doi.org/10.1016/j.jphotochem.2024.115854
78. Albayrak, A. T., & Tavman, A. (2022). Sono-oxidative desulphurization of fuels using heterogeneous and homogeneous catalysts: A comprehensive review. Ultrasonics Sonochemistry, 83, 105845. https://doi.org/10.1016/j.ultsonch. 2022.105845
79. Bi, Y., Zhang, X., Wang, Y., & Li, J. (2021). Synergistic effect of adsorption and photocatalysis for the degradation of toluene by $TiO_2$ loaded on ACF modified by Zn(CH3COO)2. Environmental Science and Pollution Research, 28(40), 57398–57411. https://doi.org/10.1007/s11356-021-14624-9
80. Nguyen, T. N., Nguyen, T. T., Nguyen, T. A., & Tran, V. T. (2020). A novel photocatalyst composite of magnesium aminoclay and $TiO_2$ immobilized into activated carbon fibre (ACF) matrix for pollutant removal. Journal of Nanoscience and Nanotechnology, 20(11), 6844–6849. https://doi.org/10.1166/jnn.2020.18844
81. Feng, J., Li, X., Zhang, Y., Wang, P., & Liu, Q. (2022). The synergistic effect of adsorption-photocatalysis for removal of organic pollutants on mesoporous Cu2V2O7/Cu3V2O8/g-C3N4 heterojunction. International Journal of Molecular Sciences, 23(22), 14264. https://doi.org/10.3390/ijms232214264
82. Katz, M. J., Brown, Z. J., Colón, Y. J., Siu, P. W., Scheidt, K. A., Snurr, R. Q., Hupp, J. T., & Farha, O. K. (2013). A facile synthesis of UiO-66, UiO-67 and their derivatives. Chemical Communications, 49(82), 9449–9451. https://doi.org/10.1039/ C3CC46105J
83. Bezerra, M. A., Santelli, R. E., Oliveira, E. P., Villar, L. S., & Escaleira, L. A. (2008). Response surface methodology (RSM) as a tool for optimization in analytical chemistry. Talanta, 76(5), 965–977. https://doi.org/10.1016/j.talanta.2008.05.019
84. Barghi, B., Niidu, A., & Karimzadeh, R. (2021). The effect of water and zinc loading on LPG catalytic cracking for light olefin production using response surface methodology. Proceedings of the Estonian Academy of Sciences, 70(2), 135–147. https://doi.org/10.3176/proc.2021.2.01
85. Cavka, J. H., Jakobsen, S., Olsbye, U., Guillou, N., Lamberti, C., Bordiga, S., & Lillerud, K. P. (2008). A new zirconium inorganic building brick forming metal organic frameworks with exceptional stability. Journal of the American Chemical Society, 130(42), 13850–13851. https://doi.org/10.1021/ja8057953
86. Ma, L., Feng, X., Cai, F., Sun, C., & Ding, H. (2022). Cobalt-doped UiO-66 nanoparticle as a photo-assisted Fenton-like catalyst for the degradation of rhodamine B. Colloids and Surfaces A: Physicochemical and Engineering Aspects, 643, 128734. https://doi.org/10.1016/j.colsurfa.2022.128734
87. Ahmed, M., Al-Hadeethi, Y. M., Alshahrie, A., Kutbee, A. T., Al-Hossainy, A. F., & Shaaban, E. R. (2022). The role of cobalt to control the synthesis of nanoscale Co/UiO-66 composite for photocatalysis. Journal of the American Ceramic Society, 105(12), 7043-7052. https://doi.org/10.1111/jace.18672
88. Beshtar, M., Larimi, A., Asgharinezhad, A. A., & Khorasheh, F. (2024). Ultra-deep photocatalytic oxidative desulphurization of model fuel using Ti-UiO-66 (Zr) metal–organic framework. Catalysis Letters, 154(6), 2633-2647. https://doi.org/ 10.1007/s10562-023-04506-9

89. Vermoortele, F., Vandichel, M., Van de Voorde, B., Ameloot, R., Waroquier, M., Van Speybroeck, V., & De Vos, D. E. (2012). Electronic effects of linker substitution on Lewis's acid catalysis with metal–organic frameworks. Angewandte Chemie International Edition, 51(20), 4887–4890. https://doi.org/10.1002/anie.201108565
90. Vo, T. K., Nguyen, V. C., Song, M. G., Kim, D., Yoo, K. S., Park, B. J., & Kim, J. (2020). Facile synthesis of bimetallic Ni-M (M = Co, Cu, Zn) MOF-derived catalysts and their performance in the oxidative desulphurization process. Journal of Industrial and Engineering Chemistry, 86, 178–185. https://doi.org/10.1016/j.jiec.2020.03.001
91. Pan, M., Gao, R., Liang, S., Hu, X., Xie, M., Chen, W., & Wang, S. (2025). Oxygen vacancies-rich bimetallic Zr/Co-UiO-66 materials for bifunctional adsorption-photodegradation of tetracycline antibiotics in water. Chemical Engineering Journal, 164397. https://doi.org/10.1016/j.cej.2025.164397
92. Ahmed, M., Al-Hadeethi, Y. M., Alshahrie, A., Kutbee, A. T., Al-Hossainy, A. F., & Shaaban, E. R. (2022). The role of cobalt to control the synthesis of nanoscale Co/UiO-66 composite for photocatalysis. Journal of the American Ceramic Society, 105(12), 7043-7052. https://doi.org/10.1111/jace.18672
93. Yang, Y., Hu, X., Wang, G., Han, J., Zhang, Q., Liu, W., ... & Zhou, Z. (2024). Two better than one: enhanced photo-assisted Li-O2 batteries with bimetallic Fe-UiO-66 metal-organic framework photocathodes. Advanced Functional Materials, 34(24), 2315354. https://doi.org/10.1002/adfm.202315354
94. Kim, J. Y., Kang, J., Cha, S., Kim, H., Kim, D., Kang, H., Choi, I., & Kim, M. (2024). Recent advances in metal-organic framework-based nanomaterials for photocatalytic desulphurization. Nanomaterials, 14(1), 110. https://doi.org/10.3390/nano14010110
95. Yang, Q., Zhang, H. Y., Wang, L., Zhang, Y., & Zhao, J. (2018). Metal-organic frameworks for oxidative desulphurization: A review. ACS Omega, 3(4), 4199–4212. https://doi.org/10.1021/acsomega.8b00157
96. Han, Y., Liu, M., Li, K., Sun, Q., Zhang, W., Song, C., ... & Guo, X. (2017). In situ synthesis of titanium doped hybrid metal–organic framework UiO-66 with enhanced adsorption capacity for organic dyes. Inorganic Chemistry Frontiers, 4(11), 1870-1880. https://doi.org/10.1039/C7QI00437K
97. Ye, G., Qi, H., Zhou, W., Xu, W., & Sun, Y. (2019). Green and scalable synthesis of nitro- and amino-functionalized UiO-66 (Zr) and the effect of functional groups on the oxidative desulphurization performance. Inorganic Chemistry Frontiers, 6(5), 1267–1274. https://doi.org/10.1039/C9QI00172G
98. Wang, Y. L., Zhang, S., Zhao, Y. F., Bedia, J., Rodriguez, J. J., & Belver, C. (2021). UiO-66-based metal organic frameworks for the photodegradation of acetaminophen under simulated solar irradiation. Journal of Environmental Chemical Engineering, 9(5), 106087. https://doi.org/10.1016/j.jece.2021.106087
99. Pan, Y., Jiang, S., Xiong, W., Liu, D., Li, M., He, B., ... & Luo, D. (2020). Supported CuO catalysts on metal-organic framework (Cu-UiO-66) for efficient catalytic wet peroxide oxidation of 4-chlorophenol in wastewater. Microporous and Mesoporous Materials, 291, 109703. https://doi.org/10.1016/j.micromeso.2019.109703
100. Mingyue, Q., Yilong, H., Dan, Z., Zhu, L., Xu, J., Hang, Z., ... & Chang, S. (2025). Polyethyleneimine-grafted Fe-UiO-66-NH2 composite for highly efficient adsorption of anionic dyes. Colloids and Surfaces A: Physicochemical and Engineering Aspects, 138354. https://doi.org/10.1016/j.colsurfa.2025.138354

101. Chowdhury, S., Sharma, P., Kundu, K., Das, P. P., Rathi, P., & Siril, P. F. (2022). Systematic Thiol Decoration in a Redox-Active UiO-66-(SH)2 Metal–Organic Framework: A Case Study under Oxidative and Reductive Conditions. https://doi.org/10.1021/acs.inorgchem.2c04233
102. Marcos, F. C. F., Costa, M. J. F., Catuzo, G. L., de Moraes, D. A., de Oliveira Junior, M., Mastelaro, V. R., ... & Assaf, E. M. (2023). Supported Cu catalysts on UiO-66 toward enhanced methanol selectivity by CO2 hydrogenation: Effect of Cu loading. Journal of Catalysis, 427, 115104. https://doi.org/10.1016/j.jcat.2023.115104
103. Chu, L., Wang, Z., Zhao, T., Yang, M., & Wang, G. (2025). Defective hierarchical porous Ce-UiO-66 excites phosphotungstic acid for superior low-temperature oxidative desulphurization. Journal of Hazardous Materials, 138762. https://doi.org/10.1016/j.jhazmat.2025.138762
104. Bui, T. M. N., Vo, T. K., Phuong, N. H. Y., Nguyen, V. H., Nguyen, V. C., Nguyen, Q. H., & Dang, N. T. T. (2025). Fe (III)-incorporated UiO-66 (Zr)–NH2 frameworks: Microwave-assisted scalable production and their enhanced photo-Fenton degradation catalytic activities. Separation and Purification Technology, 355, 129723. https://doi.org/10.1016/j.seppur.2024.129723
105. Manh, T. D., Nguyen, V. T., Duyen, V. T., Nga, N. T. T., Man, N. Q., Thoa, P. T. H., ... & Khieu, D. Q. (2023). Differential pulse voltammetry determination of acetaminophen and codeine in pharmaceutical formulations using a Mn/UiO-66 modified glassy carbon electrode. Journal of Nanoparticle Research, 25(9), 185. https://doi.org/10.1007/s11051-023-05839-7
106. Abbaslou, R. M. M., Tavassoli, A., Soltan, J., & Dalai, A. K. (2009). Iron catalysts supported on carbon nanotubes for Fischer–Tropsch synthesis: Effect of catalytic site position. Applied Catalysis A: General, 367(1–2), 47–52. https://doi.org/10.1016/j.apcata.2009.07.025
107. Akbari, A., Omidkhah, M., & Towfighi, D. J. (2014). Optimization of operating conditions in oxidation of dibenzothiophene in the light hydrocarbon model. Chemical Industry and Chemical Engineering Quarterly, 20(3), 315–323. https://doi.org/10.2298/CICEQ121210013A
108. Saleh, T. A. (2018). Simultaneous adsorptive desulphurization of diesel fuel over bimetallic nanoparticles loaded on activated carbon. Journal of Cleaner Production, 172, 2123–2132. https://doi.org/10.1016/j.jclepro.2017.11.208
109. Fox, B. R., Brinich, B. L., Male, J. L., Hubbard, R. L., Siddiqui, M. N., Saleh, T. A., & Tyler, D. R. (2015). Enhanced oxidative desulphurization in a film-shear reactor. Fuel, 156, 142–147. https://doi.org/10.1016/j.fuel.2015.04.028
110. Ghahramaninezhad, M., Pakdel, F., & Shahrak, M. N. (2019). Boosting oxidative desulphurization of model fuel by POM-grafting ZIF-8 as a novel and efficient catalyst. Polyhedron, 170, 364–372. https://doi.org/10.1016/j.poly.2019.05.058
111. Wang, X. S., Li, L., Liang, J., Huang, Y. B., & Cao, R. (2017). Boosting oxidative desulphurization of model and real gasoline over phosphotungstic acid encapsulated in metal–organic frameworks: The window size matters. ChemCatChem, 9(6), 971–979. https://doi.org/10.1002/cctc.201601450
112. Beshtar, M., Larimi, A., Asgharinezhad, A. A., & Khorasheh, F. (2024). Ultra-deep photocatalytic oxidative desulphurization of model fuel using Ti-UiO-66 (Zr) metal–organic framework. Catalysis Letters, 154 (6), 2633 - 2647. http://dx.doi.org/10.1007/s10562-023-04506-9

113. Luo, H., Gu, Y., Liu, D., & Sun, Y. (2021). Advances in oxidative desulphurization of fuel oils over mofs-based heterogeneous catalysts. Catalysts, 11(12), 1557. https://doi.org/10.3390/catal11121557
114. Zhang, W., Li, X., Wang, H., Song, Y., Zhang, S., & Li, C. (2017). Deep desulphurization of model oil by photocatalytic air oxidation and adsorption using Ti (1− x) M x O2 (M= Zr, Ce). Korean Journal of Chemical Engineering, 34(12), 3132-3141. https://doi.org/10.1007/s11814-017-0229-4

## Acknowledgements

First and foremost, I would like to express my deepest gratitude to my supervisor, Professor Allan Niidu, for his unwavering support, expert guidance, and invaluable insights throughout my PhD journey. His mentorship and encouragement were instrumental in shaping this research.

I am also profoundly grateful to my colleagues, laboratory assistants, and fellow researchers at the Põlevkivi Kompetentsikeskus, Virumaa College, and the Department of Chemical and Materials Technology for their collaboration and constructive feedback, which made this endeavour both productive and enjoyable.

Finally, I owe my heartfelt thanks to my family for their unconditional love, patience, and encouragement throughout my academic pursuits and life's challenges. Without their steadfast support, this achievement would not have been possible.

## Abstract

## Desulphurization by Catalytic Oxidation using Functionalized UiO-66-based Metal Organic Frameworks

This study investigates the catalytic performance and durability of ligand-modified UiO-66 metal-organic frameworks (MOFs) with varying functional groups ($–NO_2$, –OH, $–NH_2$) in deep oxidative desulphurization (ODS) of a model fuel (MF). The research focuses on the removal of aromatic sulphur compounds, specifically dibenzothiophene (DBT), 2-methylbenzothiazole (2-MB), and 4,6-dimethyldibenzothiophene (4,6-DMDBT), dispersed in n-dodecane as a fuel phase surrogate. A comprehensive characterization of the synthesized functionalized MOFs was conducted using a suite of analytical techniques. X-ray powder diffraction (XRD) was employed for crystalline structure analysis, while Fourier transform infrared (FTIR) spectroscopy facilitated functional group identification. Proton Nuclear Magnetic Resonance ($^1$H NMR) was used to confirm that the organic linker precursors remained chemically unaltered following the synthesis procedure, and scanning electron microscopy (SEM) allowed for morphological examination. Thermogravimetric analysis (TGA) assessed thermal stability, nitrogen adsorption-desorption analysis determined surface area and porosity, and microwave plasma-atomic emission spectrometry (MP-AES) revealed elemental composition. The experimental design and optimization of the desulphurization reaction were executed using the Central Composite Design methodology. Response Surface Methodology (RSM) and Analysis of Variance (ANOVA) were employed to evaluate the individual process factors, their interactions, and the corresponding sulphur removal efficiencies. The oxidation susceptibility of the aromatic sulphur compounds followed the order DBT > 2-MB >> 4,6-DMDBT across all MOF catalysts tested. Optimal conditions for maximum desulphurization efficiency were identified as a temperature of 66.7 °C, an oxidant to sulphur mass ratio of 3.0 (mg/mg), and a MOF to sulphur ratio of 9.7 (by weight). Under these conditions, UiO-66-$NO_2$ demonstrated superior catalytic activity, achieving removal efficiencies of 98.7% for DBT, 93.2% for 2-MB, and 69.3% for 4,6-DMDBT. The nitro-functionalized UiO-66 (UiO-66-$NO_2$) exhibited higher efficiency in deep oxidative desulphurization compared to other UiO-66-based catalysts examined in this study. This enhanced performance can be attributed to the electron-withdrawing nature of the nitro group, which may increase the Lewis acidity of the metal centers, thereby promoting the oxidation of sulphur compounds. All MOFs demonstrated acceptable catalytic activity and reusability over four consecutive reaction cycles under optimal conditions. However, a gradual decrease in activity was observed, likely due to factors such as catalyst deactivation or structural changes during repeated use. This research contributes to the development of efficient and sustainable catalysts for deep desulphurization processes, addressing the growing demand for ultra-low sulphur fuels in the context of stringent environmental regulations.

This study also presents a novel and systematic approach to elucidate the fundamental reaction pathways and overall mechanisms of oxidative desulphurization (ODS) using the theory of complex kinetics. The research focuses on the removal of dibenzothiophene (DBT) from a model fuel system, employing a solvothermally synthesized Metal Organic Framework (MOF), specifically UiO-66-$NO_2$, as the catalyst. The investigation spans a temperature range of 20-100 °C, providing comprehensive insights into the temperature-

dependent kinetics of the ODS process. Central to this methodology is the construction of a "matrix of intermediates," which facilitates the organization and analysis of elementary reactions, ultimately leading to the identification of overall reaction pathways. The proposed ODS mechanism encompasses eleven fundamental reaction steps, incorporating adsorption, oxidation, and desorption processes, thus providing a holistic representation of the catalytic cycle. The kinetic parameters of the model were optimized using MATLAB software and described using the reparametrized Arrhenius equation, allowing for a more accurate representation of temperature-dependent rate constants. To further validate the reliability of the estimated parameters and model predictions, Markov chain Monte Carlo (MCMC) modeling was employed, offering a robust statistical framework for parameter estimation and uncertainty quantification. Notably, this study marks the first application of Complex Reaction theory to investigate the ODS reaction over MOFs, representing a significant advancement in the field. The experimental results demonstrated satisfactory agreement with the model predictions, underscoring the efficacy of this approach in elucidating complex reaction mechanisms. This research not only contributes to the fundamental understanding of ODS kinetics but also provides a valuable framework for future investigations into catalytic desulphurization processes. The insights gained from this study have potential implications for the design and optimization of more efficient desulphurization catalysts and processes, addressing the ongoing challenge of producing ultra-low sulphur fuels in an environmentally sustainable manner.

# Lühikokkuvõte

## Katalüütiline oksüdatiivne väävli eemaldamine kasutades funktsionaliseeritud UiO-66 põhiseid metallorgaanilisi võrestruktuure

Käesolev töö uurib modifitseeritud ligandidega ja dopeeritud UiO-66 metallorgaaniliste võrestruktuuride (MOF-ide) katalüütilist tõhusust ja vastupidavust väävli oksüdatiivses eemaldamises mudelkütustest. Uurimus keskendub aromaatsete väävliühendite, täpsemalt dibensotiofeeni (DBT), 2-metüülbensotiasooli (2-MB) ja 4,6-dimetüüldibensotiofeeni (4,6-DMDBT) eemaldamisele, mis on lahustatud n-dodekaanis mudelkütusena.

Sünteesitud funktsionaliseeritud MOF-ide põhjalik iseloomustamine viidi läbi kasutades mitmeid analüütilisi meetodeid. Röntgenpulberdifraktsiooni (XRD) kasutati kristallilise struktuuri analüüsiks, samas kui Fourier' teisendusega infrapunaspektroskoopia (FTIR) võimaldas funktsionaalrühmade tuvastamist. Prooton tuumamagnetresonantsspektroskoopia ($^1$H NMR) andis ülevaate molekulaarstruktuurist ja skaneeriv elektronmikroskoopia (SEM) võimaldas uurida morfoloogiat. Termogravimeetriline analüüs (TGA) hindas termilist stabiilsust, lämmastiku adsorptsioonidesorptsiooni analüüs määras eripinna ja poorsuse ning mikrolaine-plasma aatomemissioonspektromeetria (MP-AES) tuvastas elementkoostise.

Väävlitustamisreaktsiooni katseplaani koostamiseks ja optimeerimiseks kasutati tsentraalse komposiitdisaini metoodikat. Vastuspinna metoodikat (RSM) ja dispersioonanalüüsi (ANOVA) kasutati üksikute protsessiparameetrite, nende vastastikuste mõjude ja vastavate väävli eemaldamise efektiivsuste hindamiseks.

Aromaatsete väävliühendite oksüdatsiooniefektiivsus järgis järjekorda DBT > 2-MB >> 4,6-DMDBT kõigi testitud MOF katalüsaatorite puhul. Optimaalsed tingimused maksimaalse väävlitustamise efektiivsuse saavutamiseks määrati kui temperatuur 66,7 °C, oksüdeeriva aine ja väävli suhe 3,0 (ekvivalentides) ning MOF-i ja väävli suhe 9,7 (massi järgi).

Nende tingimuste juures näitas UiO-66-$NO_2$ parimat katalüütilist aktiivsust, saavutades eemaldamise efektiivsused 98,68% DBT, 93,23% 2-MB ja 69,32% 4,6-DMDBT puhul. Nitro-funktsionaliseeritud UiO-66 (UiO-66-$NO_2$) näitas kõrgemat efektiivsust sügavas oksüdatiivses väävlitustamises võrreldes teiste selles uuringus uuritud UiO-66-põhiste katalüsaatoritega. Seda paremat toimivust saab omistada nitrorühma elektronaktseptoorsele iseloomule, mis võib suurendada metallitsentrite Lewise happelisust, soodustades seeläbi väävliühendite oksüdatsiooni.

Kõik MOF-id näitasid aktsepteeritavat katalüütilist aktiivsust ja taaskasutatavust nelja järjestikuse reaktsioonitsükli jooksul optimaalsetes tingimustes. Siiski täheldati järkjärgulist aktiivsuse vähenemist, tõenäoliselt katalüsaatori deaktiveerumise või struktuursete muutuste tõttu korduva kasutamise käigus.

See uuring esitab ka uudse ja süstemaatilise lähenemisviisi oksüdatiivse väävlitustamise (ODS) põhiliste reaktsiooniteede ja üldiste mehhanismide selgitamiseks, kasutades komplekskineetika teooriat. Uurimus keskendub dibensotiofeeni (DBT) eemaldamisele mudel-kütusesüsteemist, kasutades katalüsaatorina solvotermiliselt sünteesitud metallorgaanilist võrgustikku (MOF), täpsemalt UiO-66-$NO_2$. Uuring hõlmab

temperatuurivahemikku 20-100 °C, pakkudes põhjalikku ülevaadet ODS protsessi temperatuurist sõltuvast kineetikast.

Selle metoodika keskmes on "vaheühendite maatriksi" koostamine, mis hõlbustab elementaarreaktsioonide organiseerimist ja analüüsi, viies lõpuks üldiste reaktsiooniteede tuvastamiseni. Pakutud ODS mehhanism hõlmab ühteteist põhilist reaktsioonietappi, mis hõlmavad adsorptsiooni-, oksüdatsiooni- ja desorptsiooni-protsesse, pakkudes seega terviklikku ülevaadet katalüütilisest tsüklist.

Mudeli kineetilised parameetrid optimeeriti MATLAB tarkvara abil ja kirjeldati kasutades reparametriseeritud Arrheniuse võrrandit, võimaldades täpsemat temperatuurist sõltuvate kiiruskonstantide esitust. Hinnatud parameetrite ja mudeli ennustuste usaldusväärsuse täiendavaks valideerimiseks kasutati Markovi ahela Monte Carlo (MCMC) modelleerimist, et hinnata kvantitatiivselt protsessi parameetreid ja nende mõõtemääramatusi.

Märkimisväärselt tähistab see uuring kompleksreaktsioonide teooria esimest rakendust ODS reaktsiooni uurimiseks MOF-ide peal, kujutades endast olulist edasiminekut selles valdkonnas. Eksperimentaalsed tulemused näitasid rahuldavat kooskõla mudeli ennustustega, rõhutades selle lähenemisviisi tõhusust keerukate reaktsioonimehhanismide selgitamisel.

See uurimus ei panusta mitte ainult ODS kineetika fundamentaalsesse mõistmisse, vaid pakub ka väärtuslikku raamistikku tulevasteks uuringuteks katalüütiliste väävlitustamisprotsesside valdkonnas. Sellest uuringust saadud teadmistel on potentsiaalsed mõjud tõhusamate väävlitustamiskatalüsaatorite ja -protsesside kavandamisele ja optimeerimisele, vastates jätkuvale väljakutsele toota ülimadala väävlisisaldusega kütuseid keskkonnanõuete kontekstis.

# Appendix

**Publication I**

**Barghi, B**., Jürisoo, M., Volokhova, M., Seinberg, L., Reile, I., Mikli, V. and Niidu, A., 2022. Process optimization for catalytic oxidation of dibenzothiophene over UiO-66-$NH_2$ by using a response surface methodology. ACS Omega, 7(19), pp.16288-16297.

ACS OMEGA

http://pubs.acs.org/journal/acsodf

Article

# Process Optimization for Catalytic Oxidation of Dibenzothiophene over UiO-66-$NH_2$ by Using a Response Surface Methodology

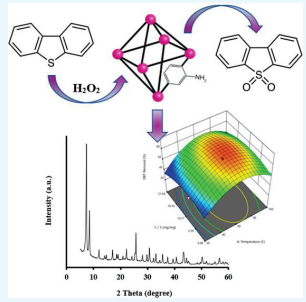
Bijan Barghi,* Martin Jürisoo, Maria Volokhova, Liis Seinberg, Indrek Reile, Valdek Mikli, and Allan Niidu

Cite This: *ACS Omega* 2022, 7, 16288−16297

Read Online

ACCESS | Metrics & More | Article Recommendations

**ABSTRACT:** This research investigates the catalytic performance of a metal−organic framework (MOF) with a functionalized ligand—UiO-66-$NH_2$—in the oxidative desulfurization of dibenzothiophene (DBT) in *n*-dodecane as a model fuel mixture (MFM). The solvothermally prepared catalyst was characterized by XRD, FTIR, $^1$H NMR, SEM, TGA, and MP-AES analyses. A response surface methodology was employed for the experiment design and variable optimization using central composite design (CCD). The effects of reaction conditions on DBT removal efficiency, including temperature ($X_1$), oxidant agent over sulfur (O/S) mass ratio ($X_2$), and catalyst over sulfur (C/S) mass ratio ($X_3$), were assessed. Optimal process conditions for sulfur removal were obtained when the temperature, O/S mass ratio, and C/S mass ratio were 72.6 °C, 1.62 mg/mg, and 12.1 mg/mg, respectively. Under these conditions, 89.7% of DBT was removed from the reaction mixture with a composite desirability score of 0.938. From the results, the temperature has the most significant effect on the oxidative desulfurization reaction. The model *F* values gave evidence that the quadratic model was well-fitted. The reusability of the MOF catalyst in the ODS reaction was tested and demonstrated a gradual loss of activity over four runs.




## 1. INTRODUCTION

Currently, the implementation by most countries of strict regulations for fossil fuels for environmental protection purposes has prompted a growing interest in investigations to improve deep desulfurization methodologies.[1−3] Hydrodesulfurization (HDS) is one of the most efficient methods in removing sulfur compounds;[4,5] nonetheless, it is less effective for removing planar sulfur-containing compounds, e.g., benzothiophene and dibenzothiophene. It requires large reactors and highly active catalysts with severe operating conditions, including high temperature and hydrogen pressure.[6,7] Hence, alternative approaches are required to achieve deep desulfurization, including selective adsorption, alkylative desulfurization, biodesulfurization, and oxidative desulfurization (ODS).[8] ODS is a green and promising process for removing planar sulfur compounds that can be carried out under ambient conditions while avoiding the use of hydrogen.[9] In an ODS reaction, when sulfur-containing compounds are oxidized, the sulfur removal efficiency of the catalysts is enhanced.[10,11] ODS converts sulfur compounds into high-polarity sulfoxides and sulfones that can be extracted by a polar solvent afterward. ODS reactions can be operated under mild operating conditions in the liquid phase.

Various oxidizing agents such as *tert*-butyl hydroperoxide, hydrogen peroxide, and oxygen have been addressed in prior studies.[12−14] However, hydrogen peroxide is the more favorable agent because of its commercial availability, selectivity, and environmental issues.[15−18] Employing an appropriate catalyst improves the activity of oxidants in the ODS process, of which metal−organic frameworks (MOFs) are good candidates that contain structurally rigid inorganic secondary building units (SBUs) and flexible and tunable organic linkers.[19−22] Among the hybrid MOFs, UiO-66(Zr) derivatives are impressively contributing to both scientific and industrial applications. It has been outlined that pristine UiO-66 can achieve more than 90% oxidative sulfur conversion in a short reaction time;[23−25] moreover, other functional groups (−$NH_2$, −OH) could also significantly influence the chemical activity and it has been mentioned that they can provide a strong affinity for sulfur oxidation.[26−29]

Presently, various MOFs have been recognized for ODS reactions, while there have been only a few reports on using amino-functionalized UiO-66. The performance of UiO-66-$NH_2$ was investigated for thiophene removal from *n*-octane at 40 °C with a certain amount of an MOF,[30] dibenzothiophene

Received: October 25, 2021
Accepted: March 29, 2022
Published: May 2, 2022



Downloaded from pubs.acs.org/acsodf/article-pdf/7/19/16288/10276166/ao1c05965.pdf by TALLINN TECHNICAL UNIV user on 25 September 2026

ACS Publications

© 2022 The Authors. Published by American Chemical Society



https://doi.org/10.1021/acsomega.1c05965
*ACS Omega* 2022, 7, 16288−16297

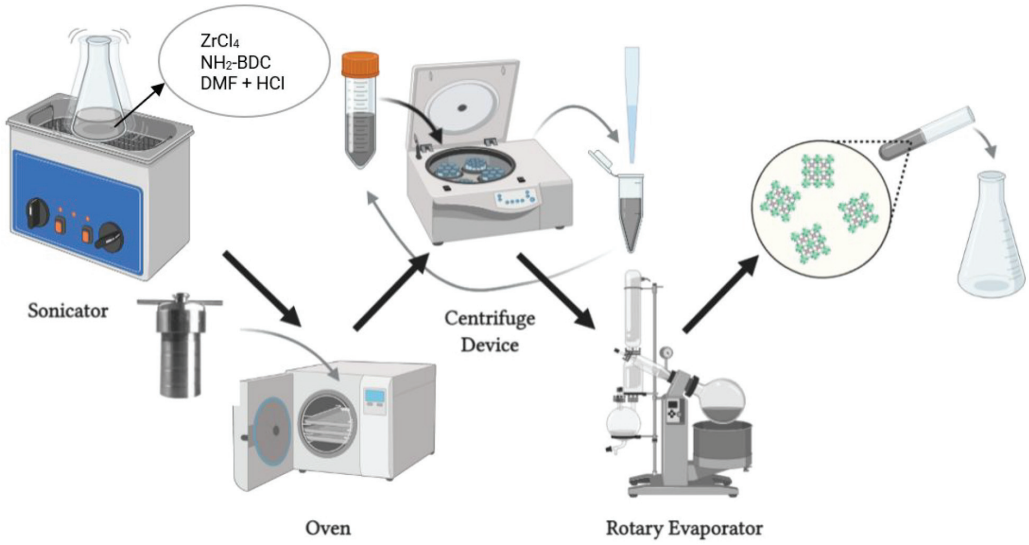



**Figure 1.** Schematic of the solvothermal synthesis of UiO-66-$NH_2$ (created with BioRender.com).

removal from *n*-octane at 70%°C with an $H_2O_2$/sulfur ratio of 4,[31] and DBT and 4,6-dimethyldibenzothiophene removal at 60 °C with an $H_2O_2$/sulfur ratio of 6 and 0.184 mmol of catalyst.[32] Thus, far, there have been no reports on statistical optimization of operation conditions and MOF amounts.

In this study, amino-functionalized (−$NH_2$) UiO-66(Zr) was synthesized by a solvothermal method for the ODS reaction. The characterization of samples was carried out by different techniques, including XRD, FTIR, $^1$H NMR, SEM, TGA, and MP-AES. The effect of the reaction conditions and the performance of UiO-66-$NH_2$ in DBT oxidative removal were systematically investigated, leading to the development of optimal operational conditions. To understand the importance of process parameters—temperature, oxidant amount, and catalyst dosage—a quadratic statistical model was developed from which optimal conditions were derived by employing a response surface methodology (RSM).

## 2. EXPERIMENTAL SECTION

**2.1. Materials.** Zirconium(IV) chloride (ZrCl4, 98%, Acros), 2-aminoterephthalic acid (99%, Acros), hydrochloric acid (HCl, 36%, Honeywell), *N*,*N*-dimethylformamide (DMF, 99.5%, Fisher), ethanol ($C_2H_5OH$, 99.9%, Honeywell), acetonitrile (99.9%, Honeywell), *n*-dodecane (99%, Alfa Aesar), hydrogen peroxide ($H_2O_2$, 30%, Alfa Aesar), and dibenzothiophene (98%, Acros) were used as received.

**2.2. Synthesis of UiO-66-$NH_2$.** The UiO-66-$NH_2$ MOF was prepared as previously reported.[33] Briefly, 1 g of $ZrCl_4$ and 1.07 g of 2-aminoterephthalic acid ($NH_2$-BDC) were dissolved in a mixture of 120 mL of *N*,*N*-dimethylformamide (DMF) and 8 mL of concentrated HCl with sonication for 30 min. The obtained solution was placed in an oven at 80 °C for 24 h. After it was cooled to room temperature, the product was washed three times with DMF and three times with ethanol to remove all residual solvent. Then the sample was dried by heating to 80 °C under vacuum until a pressure of 600 mbar was reached. The synthesis procedure is depicted in Figure 1.

**2.3. Characterization Methods.** X-ray powder diffraction (XRD) patterns were measured on a Rigaku Ultima IV or Panalytic Powder3 diffractometer with a 1D strip detector and Cu K$\alpha$ radiation ($\lambda$ = 0,154 nm), a beam voltage of 45 kV, and a beam current of 40 mA. Patterns were collected in the range 5° < 2$\theta$ < 50° with a 0.05° step size at a scanning rate of 1°/min. The functional moieties of the samples were characterized by Fourier transform infrared spectroscopy (Thermo Scientific Nicolet iS50 FTIR Spectrometric Analyzer) in the wavelength range of 400−4000 $cm^{-1}$. Scanning electron microscopy (SEM) images and surface elemental compositions of selected materials using EDS were obtained on a Zeiss FEG-SEM Ultra-55 instrument. The thermal stability of materials was tested by a simultaneous thermal analyzer (Mettler-Toledo TGA 1) in the temperature range 25−800 °C and at a heating rate of 10 °C $min^{-1}$. Microwave plasma atomic emission spectroscopy (MP-AES) with an Agilent 4200 microwave plasma atomic emission spectrometer was used to determine the purity of a sample and elemental ratios. Proton NMR spectroscopy of digested MOF samples was carried out on a 500 MHz Agilent DD2 instrument. The NMR spectrometer was equipped with a 5 mm 1D PFG probe head at 25 °C sample temperature. NMR analysis was used to determine the bulk purity of a MOF by digesting 1−2 mg of a sample in 5−10 drops of NaOD, sonicating the mixture until the sample was well dispersed, and then adding an appropriate amount of $D_2O$ (650 uL).

**2.4. Oxidative Desulfurization Process.** Catalytic oxidative desulfurization of dibenzothiophene was carried out in a 6 dram reactor. For the polar phase 6 mL of acetonitrile and for the fuel phase (MFM) 6 mL of a solution of *n*-dodecane with 1000 ppm of dibenzothiophene were placed in a reactor, and by following the design of the experiment, the desired amount of the MOF as a catalyst was placed in the reactor. The glass batch reactor was equipped with a thermometer, magnetic stirrer, and an oil bath for temperature control. Upon heating of the reactor (20−100 °C), a specified amount of hydrogen peroxide was added at atmospheric pressure. The ODS reaction started after stirring the solution

Downloaded from pubs.acs.org/acsodf/article-pdf/7/19/16288/10276166/ao1c05965.pdf by TALLINN TECHNICAL UNIV user on 25 September 2026


https://doi.org/10.1021/acsomega.1c05965
*ACS Omega* 2022, 7, 16288−16297

(600 rpm) to decrease the limitation of mass transfer. According to the experiment design, the effects of three main variables, including reaction temperature, the mass ratio of oxidant to the total amount of sulfur, and MOF dosage, were examined. After completion of the reaction (150 min), samples from the fuel phase were taken and finally analyzed by a Shimadzu QP2010 plus gas chromatograph−mass spectrometer to obtain the DBT conversion. In this study, sulfones and sulfoxides were not analyzed. Equation 1 presents the calculation of efficiency of dibenzothiophene removal as the response of the design of experiments

$$\text{sulfur removal}\ (\%) = (C_0 - C_t)/C_0 \quad (1)$$

where $C_0$ and $C_t$ refer to initial and final DBT (sulfur) concentrations in MFM, respectively.

**2.5. Response Surface Methodology.** To examine the effect of the designated variables on the output response, a central composite design (CCD) with a quadratic model was employed.[34] In this method, independent variables are coded at five levels: the central point is represented by 0, −1 and +1 are factorial points, and finally, $+\alpha$ and $-\alpha$ levels refer to axial points. An analysis of variance (ANOVA) was applied to statistically analyze the measured factors and their responses.[35] The coefficient of determination ($R^2$) was used to measure the variation between experimental and predicted responses in the quadratic model. The statistical significance of the proposed model was investigated by $p$ and $F$ values. The actual values of coded levels and the range of factors are given in Table 1. The

**Table 1. Independent Test Variables at Five Levels Used for Central Composite Design**

| | | | coded variable level | | | | |
|---|---|---|---|---|---|---|---|
| factor | unit | code | ($-\alpha^a$) | (−1) | (0) | (+1) | ($+\alpha^a$) |
| temp | °C | $X_1$ | 20 | 36.21 | 60 | 83.78 | 100 |
| O/S ratio | | $X_2$ | 0.5 | 1.61 | 3.25 | 4.89 | 6 |
| C/S ratio | | $X_3$ | 0.5 | 3.44 | 7.75 | 12.06 | 15 |

$^a\alpha$ = 1.68.

mathematical equation of the quadratic model is expressed in eq 2

$$Y = \beta_0 + \sum_{i=1}^{3} \beta_i X_i + \sum_{i=1}^{3} \sum_{j=1}^{3} \beta_{ij} X_i X_j + \varepsilon \quad (2)$$

where $X_i$ and $X_j$ are the coded values of variables, $Y$ is output response, $\beta_0$, $\beta_i$, and $\beta_{ij}$ indicate polynomial coefficients for the constant, linear and, interaction terms, respectively, and $\varepsilon$ is the random error of the model. The actual number of experiments ($N$) is determined be eq 3

$$N = 2^k + 2k + n_0 \quad (3)$$

where $k$ is the number of independent factors, $2^k$ is the number of experiments for the factorial points, $2k$ is the number of experiments for the axial points, and $n_0$ is the number of repetitions for the central points. On the basis of the CCD method, 17 test runs were performed for ODS reaction optimization. The CCD model was conducted using Design-Expert version 12 software.

## 3. RESULTS AND DISCUSSION

**3.1. Characterization.** As illustrated in Figure 2a, XRD was used to evaluate the structure, crystallinity, and phase purity of UiO-66-$NH_2$. The diffraction of this sample depicted the XRD patterns of the as-synthesized UiO-66-$NH_2$, which were identical to those of the reported XRD patterns and confirmed that UiO-66-$NH_2$ had been successfully prepared.[36,37] As shown in Figure 2a, the zirconium−benzene carboxylate units form an orthorombic crystal lattice with *Immm* space group, and the major diffraction peaks were characterized using a database (ICDD-JCPDS: 964132916). Also, it was confirmed that the sample does not have any byproducts.

FT-IR bands of the sample are presented in Figure 2b. For UiO-66-$NH_2$, the IR band at 1658 $cm^{-1}$ was assigned to the C═O vibrations, indicating that DMF resides in the pores. The characteristic bands of O−C−O asymmetric stretching (at 1571 $cm^{-1}$) and symmetric stretching of terephthalic acid (1387 $cm^{-1}$) were also observed. In addition, spectral bands at 1491, 766, and 662 $cm^{-1}$ were attributed to the vibration of C═C bonds of aromatic rings, and −OH and C−H vibrations in $H_2BDC$, respectively. Meanwhile, the peak at 1438 $cm^{-1}$ could be ascribed to the N−H bending and C−N stretching vibrations.[38,39] Moreover, the IR spectrum of the sample

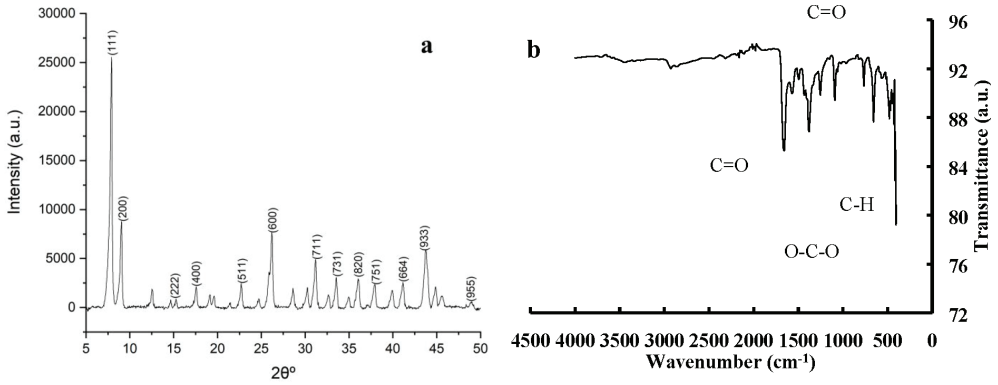



**Figure 2.** XRD powder pattern (a) and FT-IR spectrum (b) of UiO-66-$NH_2$.

Downloaded from pubs.acs.org/acsodf/article-pdf/7/19/16288/10276166/ao1c05965.pdf by TALLINN TECHNICAL UNIV user on 25 September 2026



https://doi.org/10.1021/acsomega.1c05965
ACS Omega 2022, 7, 16288−16297

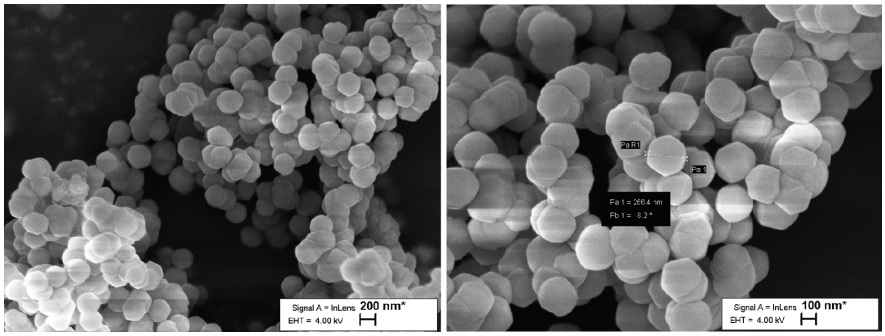



**Figure 3.** Typical SEM images of UiO-66-$NH_2$.

demonstrated one small absorption peak at 3631 $cm^{-1}$; this peak was ascribed to the $-NH_2$ group.[40]

From the SEM picture (Figure 3), the UiO-66-$NH_2$ samples were shown to exhibit a uniform octagonal morphology. On the basis of the images, the particle sizes generally converged at around 260 nm.

Figure 4 presents an $^1H$ NMR analysis for the synthesized UiO-66-$NH_2$ after digestion in an NaOD/$D_2O$ solution. The

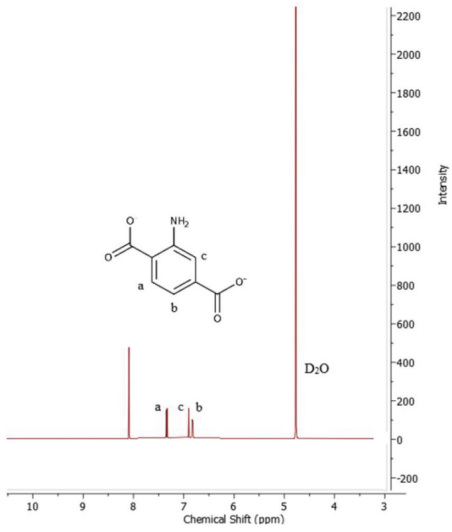



**Figure 4.** $^1H$ NMR spectrum of the prepared UiO-66-$NH_2$.

spectrum of UiO-66-$NH_2$ presents signals at 6.84, 6.90, and 7.35 ppm that were assigned to the benzene ring structure of the amino terephthalic acid in the MOF.[41]

A thermogravimetric analysis (TGA) curve of UiO-66-$NH_2$ is shown in Figure 5. The TGA curve demonstrated a three-step weight loss. The initial mass loss at 45−130 °C was assigned to the removal of ethanol and water; the second mass loss was from removal of DMF coordinated to Zr−O. The third step in weight loss after 500 °C was due to dehydroxylation of the zirconium oxo clusters and framework decomposition.[42] A quantitative analysis (MP-AES) of UiO-66-$NH_2$ showed that the zirconium composition was 25.1% of the MOF.

**3.2. Statistical Analysis.** Experiments were carried out according to the specified experimental design based on a central composite design procedure. The designated parameters, including the reaction temperature, the oxidant to sulfur mass ratio (O/S), and the catalyst to sulfur mass ratio (C/S), were studied at the designated reaction time. Accordingly, independent factors, predicted values, and experimental responses are given in Table 2. The equation in terms of actual factors as a quadratic model is obtained as shown in eq 4:

$$\begin{aligned}\text{DBT removal (wt \%)} &= -25.99 + 2.56X_1 + 11.13X_2 + 2.30X_3 - 0.09X_1X_2 \\ &\quad + 0.006X_1X_3 - 0.25X_2X_3 - 0.017{X_1}^2 - 0.52{X_2}^2 \\ &\quad - 0.10{X_3}^2 \end{aligned} \tag{4}$$

The fitness of the quadratic model was evaluated by the coefficient of determination ($R^2$), and its multiple regression model was investigated by an $F$ test. An analysis of variance (ANOVA) was performed for the fitted quadratic polynomial model of DBT removal. As demonstrated in Table 3, the model $F$ value of 7.79 implies that there is only a 0.65% chance that such a large $F$ value could occur due to noise. Also, the model $P$ value of less than 0.05 showed that the model is statistically significant. The $F$ value for the lack of fit (6.46) means that it is not significant relative to the pure error. There is a 13.96% chance that a lack of fit $F$ value this large could occur due to noise; thus, it is not significant. A nonsignificant lack of fit means the model is correctly fitted to the data and corroborated by the coefficient of determination value ($R^2$ = 0.914), indicating that the predicted mathematical model was well-fitted to the experimental data.

A comparison of the observed and predicted responses is illustrated in Figure 6; the plot depicts the reliability of the model, which implies that the DBT removal correlation has high accuracy within the investigated range of variables (eq 4). Figure 7 proves the reliability of the predicted model by normal percent probability plot of the residuals. The straight line of the graph obviously demonstrates that the residuals show a normal distribution.

This research was conducted to determine the effect of individual parameters and their interactions by using the benefit of the design of experiment (DOE). The significance of each of the three independent parameters (temperature, O/S mass ratio, and C/S mass ratio) on DBT removal efficiency

Downloaded from pubs.acs.org/acsodf/article-pdf/7/19/16288/10276166/ao1c05965.pdf by TALLINN TECHNICAL UNIV user on 25 September 2026



https://doi.org/10.1021/acsomega.1c05965
ACS Omega 2022, 7, 16288−16297

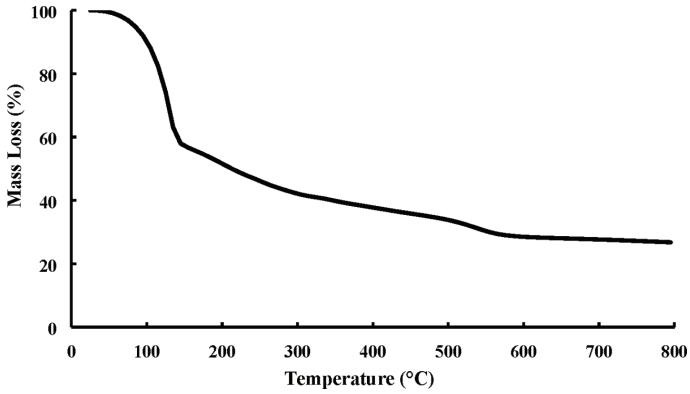



**Figure 5.** TGA curve of pristine UiO-66-$NH_2$ ($N_2$ atmosphere, heating rate 10 °C/min).

**Table 2. Central Composite Design Arrangement and Predicted and Experimental Responses**

| | | | | | DBT removal efficiency (%) | |
|---|---|---|---|---|---|---|
| run no. | point type | $X_1$ (°C) | $X_2$ (mg/mg) | $X_3$ (mg/mg) | predicted | experimental |
| 1 | center | 60.00 | 3.25 | 7.75 | 87.41 | 89.02 |
| 2 | axial | 36.22 | 4.89 | 3.44 | 73.44 | 73.14 |
| 3 | axial | 83.78 | 4.89 | 12.06 | 77.97 | 77.81 |
| 4 | factorial | 60.00 | 0.50 | 7.75 | 82.62 | 78.86 |
| 5 | axial | 83.78 | 1.61 | 12.06 | 87.58 | 92.63 |
| 6 | factorial | 100.00 | 3.25 | 7.75 | 70.29 | 67.60 |
| 7 | axial | 83.78 | 1.61 | 3.44 | 79.83 | 79.31 |
| 8 | factorial | 60.00 | 3.25 | 0.50 | 79.80 | 77.27 |
| 9 | center | 60.00 | 3.25 | 7.75 | 87.41 | 85.18 |
| 10 | axial | 36.22 | 4.89 | 12.06 | 71.74 | 77.03 |
| 11 | factorial | 60.00 | 6.00 | 7.75 | 84.40 | 81.43 |
| 12 | axial | 36.22 | 1.61 | 3.44 | 61.71 | 66.62 |
| 13 | axial | 83.78 | 4.89 | 3.44 | 77.24 | 81.26 |
| 14 | center | 60.00 | 3.25 | 7.75 | 87.41 | 89.18 |
| 15 | factorial | 20.00 | 3.25 | 7.75 | 49.81 | 45.77 |
| 16 | factorial | 60.00 | 3.25 | 15.00 | 84.89 | 80.70 |
| 17 | axial | 36.22 | 1.61 | 12.06 | 67.03 | 67.77 |

**Table 3. ANOVA for Polynomial Model of Dibenzothiophene Oxidation Yield[a]**

| source | sum of squares | degree of freedom | mean square | *F* value | *P* value |
|---|---|---|---|---|---|
| *A*: temp (°C) | 506.24 | 1 | 506.24 | 20.16 | 0.0028 |
| *B*: O/S (mg/mg) | 3.84 | 1 | 3.84 | 0.1527 | 0.7076 |
| *C*: C/S (mg/mg) | 31.27 | 1 | 31.27 | 1.25 | 0.3013 |
| *AB* | 102.53 | 1 | 102.53 | 4.08 | 0.0831 |
| *AC* | 2.92 | 1 | 2.92 | 0.1162 | 0.7432 |
| *BC* | 24.64 | 1 | 24.64 | 0.9809 | 0.3550 |
| $A^2$ | 1054.84 | 1 | 1054.84 | 42.00 | 0.0003 |
| $B^2$ | 21.46 | 1 | 21.46 | 0.8543 | 0.3861 |
| $C^2$ | 36.09 | 1 | 36.09 | 1.44 | 0.2696 |
| model | 1760.22 | 9 | 195.58 | 7.79 | 0.0065 |
| lack of fit | 165.56 | 5 | 33.11 | 6.46 | 0.1396 |
| error | 10.26 | 2 | 5.13 | | |

[a] $R^2$ = 91.37%; adjusted $R^2$ = 89.27%.

was specified by indicating the 3D surface plots and response contours (Figures 8 and 9). Figure 8 depicts response surface plots between the oxidation temperature reaction and the oxidant to sulfur mass ratio on the ODS of dibenzothiophene, which demonstrates that both factors have noticeable effects on the removal efficiency of DBT. It was observed that at a certain temperature, as the oxidant/sulfur mass ratio increases to 1.7, first the dibenzothiophene ODS efficiency is enhanced and afterward is decreased by oxidant/sulfur ratio ≥8 and higher. However, the dibenzothiophene oxidation yield

Downloaded from pubs.acs.org/acsodf/article-pdf/7/19/16288/10276166/ao1c05965.pdf by TALLINN TECHNICAL UNIV user on 25 September 2026



https://doi.org/10.1021/acsomega.1c05965
ACS Omega 2022, 7, 16288−16297

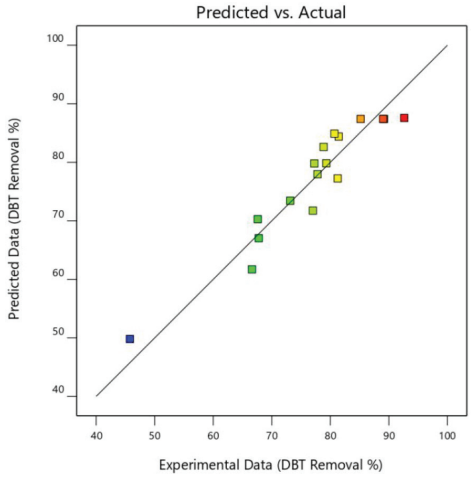



**Figure 6.** experimental and predicted removal yield of dibenzothiophene.

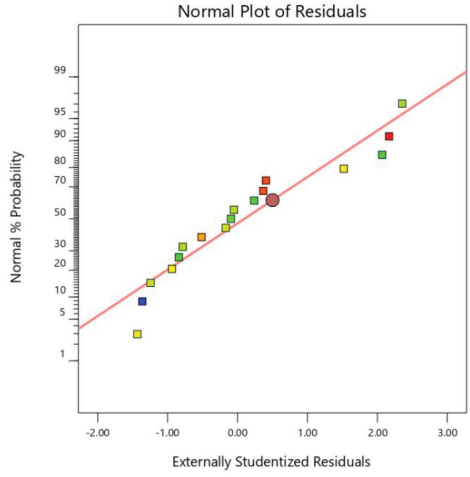



**Figure 7.** Normal percent probability versus Studentized residuals plot for the model.

increased in the presence of greater amounts of oxidants;[43,44] greater amounts of oxidants generate water molecules due to decomposition, which may occupy the MOF surface area and diminish the adsorption of dibenzothiophene on active sites. In addition, economic and environmental issues to decrease the utilization of oxidants should always be considered. Thus, the model calculated the optimal amount O/S = 1.62 mg/mg for the ODS reaction.

Increasing the temperature of the reaction from 60 to 72 °C induces an enhanced dibenzothiophene oxidation yield for a certain oxidant/sulfur mass ratio; however, temperature increases above 72 °C reduced the dibenzothiophene oxidation efficiency. As the oxidative desulfurization reaction is endothermic,[45] temperature enhancement is favors the dibenzothiophene removal process rate as well as increases the molecular movement of reaction components. On the other hand, increasing the temperature leads to oxygen peroxide decomposition; consequently, as the oxidant concentration is decreased, the ODS reaction rate is reduced.[46] Therefore, the optimal temperature can be considered to be 72 °C.

Figure 9 demonstrates the binary interaction of reaction temperature and C/S ratio. Obviously, at C/S ratios of 0.5−12 and temperatures of 60−72 °C, the maximum efficiency of dibenzothiophene ODS was attained that is pertinent to nearly complete removal, indicating that a catalyst/sulfur (C/S) ratio of 12 increased the concentration of MOF active sites at a proper level, which led to a greater dibenzothiophene oxidation yield. However, excess amounts of the MOF lead to agglomeration and active site reduction, limit the surface area with the absorbate, and negatively affect the mass transfer of reactants, and finally the efficiency of MOF catalytic activity for the oxidation process is decreased.[47]

**3.3. Determination of Optimal Conditions.** The central composite design technique has been employed to determine the optimal conditions of UiO-66-$NH_2$ MOF preparation for the oxidative dibenzothiophene removal to be maximized from MFM. Table 4 displays the optimal conditions for maximum DBT removal with a desirability value of 0.938 for the determined values of the three independent factors.

Table 5 shows the effect of UiO-66-$NH_2$ on oxidative desulfurization performance with and without catalyst. It was studied by keeping the O/S ratio 1.6, stirrer speed constant at 600 rpm, 6 mL of model fuel, 6 mL of acetonitrile, 1000 ppm of DBT, for 150 min at 36.2, 60.0, 72.6, and 83.8 °C temperatures. In the case of without catalyst (just extraction effect), the sulfur removal was about 43%, 55%, 56% and 56% less than reaction condition in the presence of the catalyst.

**3.4. Proposed Mechanism.** Figure 10 shows a plausible mechanism for the dibenzothiophene catalytic oxidative reaction. Metal cluster units of the UiO-66-$NH_2$ structure $[Zr_6O_4(OH)_4]$ are connected to 12 rings of amino terephthalic acid; accordingly, the MOF is able to strengthen the electrophilicity property of the oxidant with high electron-withdrawing capability and a reduced number of $Zr^{\delta+}$ sites. These active sites are able to increase the electrophilicity of the $H_2O_2$ in sulfur removal.[17] In the first step of the mechanism, the Zr−OH sites were protonated and then dehydrated to form unsaturated Zr sites. The unsaturated Zr sites serving as Lewis acids react with oxygen peroxide to generate peroxometallic Zr complexes in an oxidation reaction.[15] Zr ions on the MOF surface coordinated with the sulfur adsorb on the Lewis acid sites,[24] where their existence has been proven in UiO-66 and its derivatives in previous studies.[15,48,49] It has also been reported that UiO-66-$NH_2$ has many more Lewis acid sites in comparison to UiO-66.[49] The reaction between a Zr−O ion and an oxygen of the peroxide leads to hydroxyl radicals formation; accordingly, $^{\bullet}OH$ radicals have high oxidizability and electrophilicity as active oxygen species. During the electrophilic oxidation, two protons of the dibenzothiophene sulfur atom shift when the atom nucleophilically attacks the oxidative agent, and then a sulfoxide intermediate forms when the oxygen atom is transferred to the planar sulfur molecule. The generated sulfoxide forms a hydrogen bond with the active sites of ZrOH, decreasing the electronic density of the sulfur atom in the sulfoxide and thus activating it for the next nucleophilic attack by the oxidizing agent, finally leading to sulfone formation.[15,50] The ODS reaction can also occur without catalyst, but with less removal

Downloaded from pubs.acs.org/acsodf/article-pdf/7/19/16288/10276166/ao1c05965.pdf by TALLINN TECHNICAL UNIV user on 25 September 2026


https://doi.org/10.1021/acsomega.1c05965
ACS Omega 2022, 7, 16288−16297

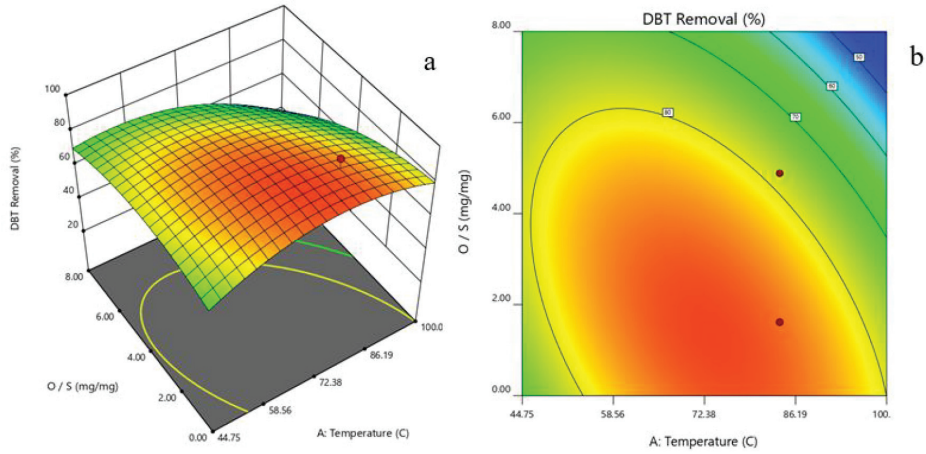



**Figure 8.** Response surface three-dimensional (a) and two-dimensional contour plots (b) indicating the effect of the reaction temperature versus oxidant/sulfur mass ratio on the dibenzothiophene oxidation efficiency. $X_3$ = 12 mg of MOF/mg of sulfur.

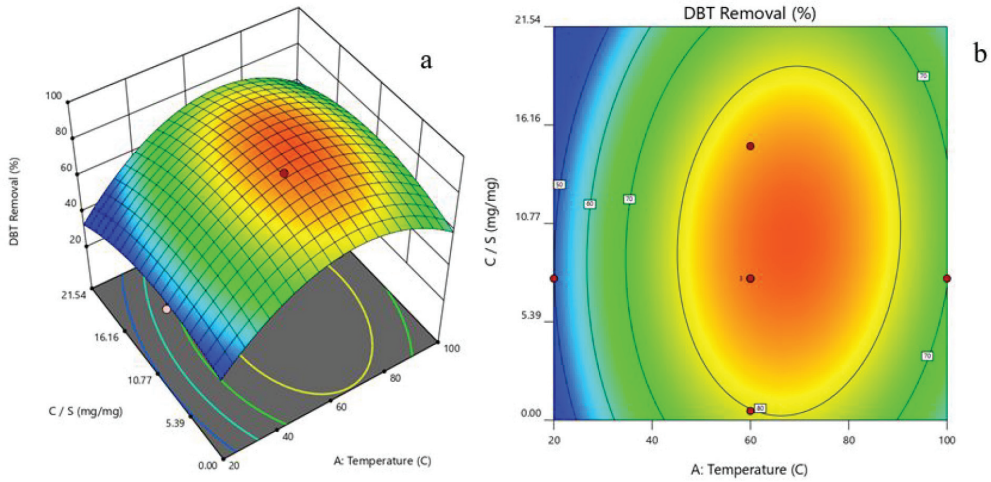



**Figure 9.** Response surface three-dimensional (a) and two-dimensional contour plots (b) indicating the effect of the reaction temperature versus catalyst/sulfur mass ratio on the dibenzothiophene oxidation efficiency. $X_2$ = 1.6 mg of oxidant/mg of sulfur.

**Table 4. Predicted Value Obtained for DBT Removal under Optimum Conditions**

| independent factor | | dibenzothiophene removal efficiency (%) | desirability (%) |
|---|---|---|---|
| *A*: temp (°C) | 72.6 | 89.7 | 93.8 |
| *B*: O/S ratio | 1.62 | | |
| *C*: C/S ratio | 11.03 | | |

**Table 5. DBT Removal with and without UiO-66-$NH_2$ in the Presence of $H_2O_2$**

| | DBT removal at different temperatures (%) | | | |
|---|---|---|---|---|
| | 36.2 °C | 60.0 °C | 72.6 °C | 83.8 °C |
| UiO-66-$NH_2$ (13.5 mg) | 68.2 | 87.0 | 89.7 | 89.6 |
| no catalyst | 25.1 | 32.1 | 33.7 | 33.6 |

efficiency. The benefit of the UiO-66-$NH_2$ MOF as a catalyst not only is due to the high activation of peroxide hydrogen inner bonds through the formation of $O^{\bullet-}{}_2$ and $^{\bullet}OH$ radicals but also the MOF mechanical stability for reuse in the ODS reaction results in a higher sulfur removal efficiency.[51]

When oxygen peroxide is employed as an oxidation agent, the catalytic activity of UiO-66-$NH_2$ depends on its ability to decompose $H_2O_2$ into $O^{\bullet-}{}_2$ and $^{\bullet}OH$ radicals (oxygen species).[52] The UiO-66 structure includes open metal nodes occupied by hydroxide or water as a terminal ligand to form Zr−OH and Zr−$OH_2$. Introduction of an amino group (−$NH_2$) as an electron-donating group in the terephthalic acid linker can enhance the decomposition of hydrogen peroxide, thus initiating the proton donation to Zr sites.[26] Furthermore, the adsorption of sulfur compounds is affiliated



https://doi.org/10.1021/acsomega.1c05965
ACS Omega 2022, 7, 16288−16297

Downloaded from pubs.acs.org/acsodf/article-pdf/7/19/16288/10276166/ao1c05965.pdf by TALLINN TECHNICAL UNIV user on 25 September 2026

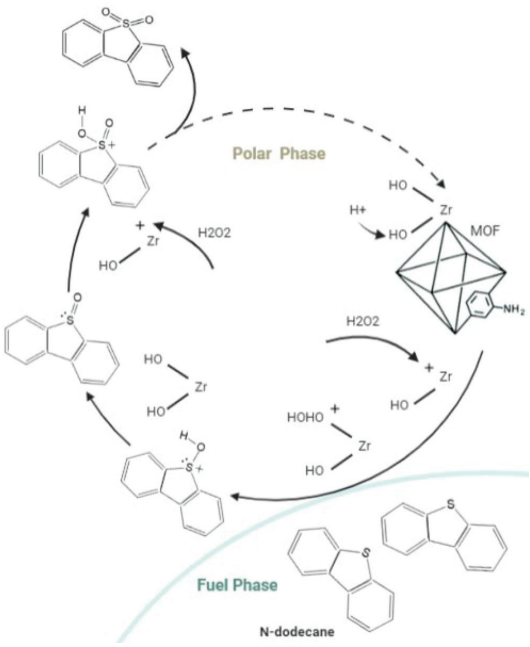



**Figure 10.** Plausible mechanism for the dibenzothiophene ODS reaction in the presence of the UiO-66-$NH_2$ MOF and $H_2O_2$ (created with BioRender.com).

with the H atom bonding. Dibenzothiophene with electron pairs around the sulfur atom is a H acceptor; consequently, an amino group in UiO-66 as a H-donor species improves the adsorption performance.[26,53]

### 3.5. Reusability of Spent Metal Organic Framework.

Catalyst reusability is a desirable property with regard to industrial utilization and economic evaluation. The regeneration of UiO-66-$NH_2$ catalysts was examined by performing four multiple DBT removal experiments at 72.6 °C under the optimal conditions. After each experiment, the MOF was separated from the oil phase and recovered by centrifugation. To eliminate the remaining sulfur, the used MOF was washed three times with acetonitrile and then dried at 100 °C in an oven for 12 h; the MOF was then utilized in a subsequent DBT removal reaction. Figure 11 illustrates the dibenzothiophene ODS yield, which was maintained at the initial level with a slight decreasing trend (about 8.5%) after four sequential cycles, decreasing from 90.08% to 82.45%. The gradual decrease in the MOF performance for the fourth cycle might be due to the fouling of MOF pores and decreasing number of active sites. Within the oxidative catalytic reaction, the formation of sulfone and sulfoxide may lead to MOF catalytic deactivation during $\pi$-complexation, so that washing and heating through the recovery process is not convenient to simply remove the poisonous agents.[54]

## 4. CONCLUSION

Functionalized UiO-66(Zr) was successfully synthesized through ligand substitution by a solvothermal methodology. The structure and phase purity of the MOF catalyst were confirmed by multiple characterization techniques. The effect

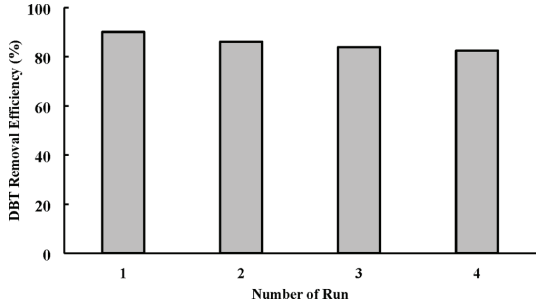



**Figure 11.** Reusability of the UiO-66-$NH_2$ catalyst in dibenzothiophene removal efficiency. Conditions: 6 mL of model fuel, 13.5 mg of MOF (C/S = 11.03), O/S = 1.6, 6 mL of acetonitrile, 150 min, 72.6 °C.

of the reaction conditions on dibenzothiophene ODS was examined, including the reaction temperature, oxidation agent/sulfur mass ratio, and catalyst/sulfur mass ratio, using the RSM-CCD technique. According to the values of the design point of desulfurization yields, the experimental results were fitted at an acceptable level to the predicted data with an appropriate $R^2$ value (about 5% error). The sulfur removal efficiency could reach 89.7% for 72.6 °C, an O/S ratio of 1.62, and a C/S ratio of 11.03 for DBT MFM (1000 ppm of S content), which was guaranteed by a desirability value of 0.938. According to the results, the temperature has the greatest effect on DBT removal; however, it seems that thermal decomposition of oxygen peroxide led to increasing oxidant usage and decreasing DBT removal at temperatures higher than 72.6 °C. Additionally, the DBT removal efficiency of the regenerated catalyst demonstrated that the employed MOF has acceptable reusability and retains its activity after four runs with about an 8.5% drop in the conversion of DBT.

## AUTHOR INFORMATION

### Corresponding Author

**Bijan Barghi** − *Virumaa College, School of Engineering, Tallinn University of Technology, 30322 Kohtla-Järve, Estonia*; orcid.org/0000-0001-9577-3302; Email: bijan.barghi@taltech.ee

### Authors

**Martin Jürisoo** − *Virumaa College, School of Engineering, Tallinn University of Technology, 30322 Kohtla-Järve, Estonia*

**Maria Volokhova** − *National Institute of Chemical Physics and Biophysics, 12618 Tallinn, Estonia*

**Liis Seinberg** − *National Institute of Chemical Physics and Biophysics, 12618 Tallinn, Estonia*

**Indrek Reile** − *National Institute of Chemical Physics and Biophysics, 12618 Tallinn, Estonia*; orcid.org/0000-0003-3278-7947

**Valdek Mikli** − *Department of Chemistry and Materials Technology, School of Engineering, Tallinn University of Technology, 19086 Tallinn, Estonia*

**Allan Niidu** − *Virumaa College, School of Engineering, Tallinn University of Technology, 30322 Kohtla-Järve, Estonia*; orcid.org/0000-0003-3406-9869

Complete contact information is available at: https://pubs.acs.org/10.1021/acsomega.1c05965

Downloaded from pubs.acs.org/acsodf/article-pdf/7/19/16288/10276166/ao1c05965.pdf by TALLINN TECHNICAL UNIV user on 25 September 2026

## Notes

The authors declare no competing financial interest.

## ■ ACKNOWLEDGMENTS

The authors appreciate the support of the Faculty of Engineering, Virumaa College of Tallinn University of Technology, and are thankful to Stat-Ease, Minneapolis, MN, USA, for providing the Design-Expert 12 Package. The authors acknowledge financial support from the Estonian Research Council (grant nos. PSG11 and PRG4) and from SA Archimedes of the European Regional Development Fund (project no. TK134).

## ■ REFERENCES

(1) Huang, C.; Chen, B.; Zhang, J.; Liu, Z.; Li, Y. Desulfurization of gasoline by extraction with new ionic liquidss. *Energy Fuels* **2004**, *18*, 1862−1864.
(2) Toutov, A. A.; Salata, M.; Fedorov, A.; Yang, Y.-F.; Liang, Y.; Cariou, R.; Betz, K. N.; Couzijn, E. P. A.; Shabaker, J. W.; Houk, K. N.; Grubbs, R. H. A potassium tert-butoxide and hydrosilane system for ultra-deep desulfurization of fuels. *Nat. Eng.* **2017**, 1−7.
(3) Li, S. S.; Li, Y. X.; Jin, M. M.; Miao, K. J.; Gu, M. X.; Liu, X. Q.; Sun, L. B. Controllable fabrication of cuprous sites in confined spaces for efficient adsorptive desulfurization. *Fuel* **2020**, *259*, 116221.
(4) Muhammad, Y.; Rashid, H. U.; Subhan, S.; Rahman, A. U.; Sahibzada, M.; Tong, Z. Boosting the hydrodesulfurization of dibenzothiophene efficiency of Mn decorated (Co/Ni)-Mo/$Al_2O_3$ catalysts at mild temperature and pressure by coupling with phosphonium based ionic liquids. *Chem. Eng. J.* **2019**, *375*, 121957.
(5) Shafiq, I.; Shafique, S.; Akhter, P.; Yang, W.; Hussain, M. Recent developments in alumina supported hydrodesulfurization catalysts for the production of sulfur-free refinery products: A technical review. *Catal. Rev.* **2022**, *64*, 1−86.
(6) Liu, Y.; Wang, H.; Zhao, J.; Liu, Y.; Liu, C. Ultra-deep desulfurization by reactive adsorption desulfurization on copper-based catalysts. *Energy Chem. J.* **2019**, *29*, 8−16.
(7) Rajendran, A.; Cui, T. Y.; Fan, H. X.; Yang, Z. F.; Feng, J.; Li, W. Y. A comprehensive review on oxidative desulfurization catalysts targeting clean energy and environment. *J. Mater. Chem. A A* **2020**, *8*, 2246−2285.
(8) Kang, L.; Liu, H.; He, H.; Yang, C. Oxidative desulfurization of dibenzothiophene using molybdenum catalyst supported on Ti-pillared montmorillonite and separation of sulfones by filtration. *Fuel* **2018**, *234*, 1229−1237.
(9) Gu, Q.; Wen, G.; Ding, Y.; Wu, K. H.; Chen, C.; Su, D. Reduced graphene oxide: a metal-free catalyst for aerobic oxidative desulfurization. *Green Chem.* **2017**, *19*, 1175−1181.
(10) Yu, X.; Han, P.; Li, Y. Oxidative desulfurization of dibenzothiophene catalyzed by $\alpha$-$MnO_2$ nanosheets on palygorskite using hydrogen peroxide as oxidant. *RSC Adv.* **2018**, *8*, 17938−17943.
(11) Jiang, Z.; Hongying, L. Ü.; Zhang, Y.; Can, L. I. Oxidative desulfurization of fuel oilss. *Chin. J. Catal.* **2011**, *32*, 707−715.
(12) Gao, Y.; Gao, R.; Zhang, G.; Zheng, Y.; Zhao, J. Oxidative desulfurization of model fuel in the presence of molecular oxygen over polyoxometalate based catalysts supported on carbon nanotubes. *Fuel* **2018**, *224*, 261−270.
(13) Mokhtar, W. N. A. W.; Bakar, W. A. W. A.; Ali, R.; Kadir, A. A. A. Optimization of oxidative desulfurization of Malaysian Euro II diesel fuel utilizing tert-butyl hydroperoxide-dimethylformamide system. *Fuel* **2015**, *161*, 26−33.
(14) Jiang, X.; Li, H.; Zhu, W.; He, L.; Shu, H.; Lu, J. Deep desulfurization of fuels catalyzed by surfactant-type decatungstates using $H_2O_2$ as oxidant. *Fuel* **2009**, *88*, 431−436.
(15) Zheng, H. Q.; Zeng, Y. N.; Chen, J.; Lin, R. G.; Zhuang, W. E.; Cao, R.; Lin, Z. J. Zr-based metal-organic frameworks with intrinsic peroxidase-like activity for ultradeep oxidative desulfurization: mechanism of $H_2O_2$ decomposition. *Inorg. Chem.* **2019**, *58*, 6983−6992.
(16) Yu, G.; Lu, S.; Chen, H.; Zhu, Z. Oxidative desulfurization of diesel fuels with hydrogen peroxide in the presence of activated carbon and formic acid. *Energy Fuels* **2005**, *19*, 447−452.
(17) Hao, L.; Hurlock, M. J.; Ding, G.; Zhang, Q. Metal-organic frameworks towards desulfurization of fuels. *Met. Org. Framework* **2020**, *378*, 175−202.
(18) Chandra Srivastava, V. An evaluation of desulfurization technologies for sulfur removal from liquid fuels. *RSC Adv.* **2012**, *2*, 759−783.
(19) Bhadra, B. N.; Jhung, S. H. Oxidative desulfurization and denitrogenation of fuels using metal-organic framework-based/-derived catalysts. *Appl. Catal. B: Environ.* **2019**, *259*, 118021.
(20) Howarth, A. J.; Peters, A. W.; Vermeulen, N. A.; Wang, T. C.; Hupp, J. T.; Farha, O. K. Best practices for the synthesis, activation, and characterization of metal-organic frameworks. *Chem. Mater.* **2017**, *29*, 26−39.
(21) Smolders, S.; Willhammar, T.; Krajnc, A.; Sentosun, K.; Wharmby, M. T.; Lomachenko, K. A.; Bals, S.; Mali, G.; Roeffaers, M. B.; De Vos, D. E.; Bueken, B. A Titanium (IV)-Based Metal-Organic Framework Featuring Defect-Rich Ti-O Sheets as an Oxidative Desulfurization Catalyst. *Angew. Chem.* **2019**, *131*, 9258−9263.
(22) Gascon, J.; Corma, A.; Kapteijn, F.; Llabres i Xamena, F. X. Metal organic framework catalysis: quo vadis? *Acs Catal.* **2014**, *4*, 361−378.
(23) Ye, G.; Qi, H.; Li, X.; Leng, K.; Sun, Y.; Xu, W. Enhancement of oxidative desulfurization performance over UiO-66 (Zr) by titanium ion exchange. *ChemPhysChem* **2017**, *18*, 1903−1908.
(24) Zhang, X.; Huang, P.; Liu, A.; Zhu, M. A metal-organic framework for oxidative desulfurization: UIO-66 (Zr) as a catalyst. *Fuel* **2017**, *209*, 417−423.
(25) Viana, A. M.; Ribeiro, S. O.; Castro, B. D.; Balula, S. S.; Cunha-Silva, L. Influence of UiO-66 (Zr) preparation strategies in its catalytic efficiency for desulfurization process. *Mater.* **2019**, *12*, 3009.
(26) Zhang, X. F.; Wang, Z.; Feng, Y.; Zhong, Y.; Liao, J.; Wang, Y.; Yao, J. Adsorptive desulfurization from the model fuels by functionalized UiO-66 (Zr). *Fuel* **2018**, *234*, 256−262.
(27) Peterson, G. W.; Mahle, J. J.; DeCoste, J. B.; Gordon, W. O.; Rossin, J. A. Extraordinary $NO_2$ Removal by the Metal-Organic Framework UiO-66-$NH_2$. *Angew. Chem.* **2016**, *128*, 6343−6346.
(28) Zhang, J.; Hu, Y.; Qin, J.; Yang, Z.; Fu, M. $TiO_2$-UiO-66-$NH_2$ nanocomposites as efficient photocatalysts for the oxidation of VOCs. *Chem. Eng. J.* **2020**, *385*, 123814.
(29) Ye, G.; Qi, H.; Zhou, W.; Xu, W.; Sun, Y. Green and scalable synthesis of nitro-and amino-functionalized UiO-66 (Zr) and the effect of functional groups on the oxidative desulfurization performance. *Inorg. Chem. Front.* **2019**, *6*, 1267−1274.
(30) Wu, F.; Cao, Y.; Liu, H.; Zhang, X. High-performance UiO-66-$NH_2$ tubular membranes by zirconia-induced synthesis for desulfurization of model gasoline via pervaporation. *J. Membr. Sci.* **2018**, *556*, 54−65.
(31) Liao, X.; Wang, X.; Wang, F.; Yao, Y.; Lu, S. Ligand Modified Metal Organic Framework UiO-66: A Highly Efficient and Stable Catalyst for Oxidative Desulfurization. *J. Inorg. Organom. Polym. Mater.* **2021**, *31*, 756−762.
(32) Li, Z.; Liao, F.; Jiang, F.; Liu, B.; Ban, S.; Chen, G.; Sun, C.; Xiao, P.; Sun, Y. Capture of $H_2S$ and $SO_2$ from trace sulfur containing gas mixture by functionalized UiO-66 (Zr) materials: A molecular simulation study. *Fluid Phase Equilib.* **2016**, *427*, 259−267.
(33) Katz, M. J.; Brown, Z. J.; Colón, Y. J.; Siu, P. W.; Scheidt, K. A.; Snurr, R. Q.; Hupp, J. T.; Farha, O. K. A facile synthesis of UiO-66, UiO-67 and their derivatives. *Chem. Commun.* **2013**, *49*, 9449−9451.
(34) Barghi, B.; Niidu, A.; Karimzadeh, R. The effect of water and zinc loading on LPG catalytic cracking for light olefin production using Response Surface Methodology. *Proc. Est. Acad. Sci.* **2021**, *70*, 135−147.

Downloaded from pubs.acs.org/acsodf/article-pdf/7/19/16288/10276166/ao1c05965.pdf by TALLINN TECHNICAL UNIV user on 25 September 2026

(35) Bezerra, M. A.; Santelli, R. E.; Oliveira, E. P.; Villar, L. S.; Escaleira, L. A. Response surface methodology (RSM) as a tool for optimization in analytical chemistry. *Talanta* **2008**, *76*, 965−977.
(36) Zlotea, C.; Phanon, D.; Mazaj, M.; Heurtaux, D.; Guillerm, V.; Serre, C.; Horcajada, P.; Devic, T.; Magnier, E.; Cuevas, F.; Ferey, G.; Llewellyn, P. L.; Latroche, M. Effect of $NH_2$ and $CF_3$ functionalization on the hydrogen sorption properties of MOFs. *Dalton Trans.* **2011**, *40*, 4879−4881.
(37) Sadeghi, S.; Jafarzadeh, M.; Abbasi, A. R.; Daasbjerg, K. Incorporation of CuO NPs into modified UiO-66-$NH_2$ metal-organic frameworks (MOFs) with melamine for catalytic C-O coupling in the Ullmann condensation. *New J. Chem.* **2017**, *41*, 12014−12027.
(38) Vermoortele, F.; Ameloot, R.; Vimont, A.; Serre, C.; De Vos, D. An amino-modified Zr-terephthalate metal-organic framework as an acid-base catalyst for cross-aldol condensation. *Chem. Commun.* **2011**, *47*, 1521−1523.
(39) Vermoortele, F.; Vandichel, M.; Van de Voorde, B.; Ameloot, R.; Waroquier, M.; Van Speybroeck, V.; De Vos, D. E. Electronic effects of linker substitution on Lewis acid catalysis with metal-organic frameworks. *Angew. Chem., Int. Ed.* **2012**, *51*, 4887−4890.
(40) Shearer, G. C.; Forselv, S.; Chavan, S.; Bordiga, S.; Mathisen, K.; Bjørgen, M.; Svelle, S.; Lillerud, K. P. In situ infrared spectroscopic and gravimetric characterisation of the solvent removal and dehydroxylation of the metal organic frameworks UiO-66 and UiO-67. *Top. Catal.* **2013**, *56*, 770−782.
(41) Zhu, J.; Wu, L.; Bu, Z.; Jie, S.; Li, B. G. Polyethyleneimine-modified UiO-66-$NH_2$ (Zr) metal-organic frameworks: preparation and enhanced $CO_2$ selective adsorption. *ACS Omega* **2019**, *4*, 3188−3197.
(42) Fang, Y.; Zhang, L.; Zhao, Q.; Wang, X.; Jia, X. Application of acid-promoted UiO-66-$NH_2$ MOFs in the treatment of wastewater containing methylene blue. *Chem. Pap.* **2019**, *73*, 1401−1411.
(43) Saleh, T. A. Simultaneous adsorptive desulfurization of diesel fuel over bimetallic nanoparticles loaded on activated carbon. *J. Clean. Prod.* **2018**, *172*, 2123−2132.
(44) Fox, B. R.; Brinich, B. L.; Male, J. L.; Hubbard, R. L.; Siddiqui, M. N.; Saleh, T. A.; Tyler, D. R. Enhanced oxidative desulfurization in a film-shear reactor. *Fuel* **2015**, *156*, 142−147.
(45) Abbaslou, R. M. M.; Tavassoli, A.; Soltan, J.; Dalai, A. K. Iron catalysts supported on carbon nanotubes for Fischer−Tropsch synthesis: Effect of catalytic site position. *Appl. Catal., A* **2009**, *367*, 47−52.
(46) Akbari, A.; Omidkhah, M.; Towfighi, D. J. Optimization of operating conditions in oxidation of dibenzothiophene in the light hydrocarbon model. *Chem. Ind. Chem. Eng. Quart.* **2014**, *20*, 315−323.
(47) Cao, Y.; Wang, H.; Ding, R.; Wang, L.; Liu, Z.; Lv, B. Highly efficient oxidative desulfurization of dibenzothiophene using Ni modified $MoO_3$ catalyst. *Appl. Catal., A* **2020**, *589*, 117308.
(48) Di Giuseppe, A.; Crucianelli, M.; De Angelis, F.; Crestini, C.; Saladino, R. Efficient oxidation of thiophene derivatives with homogeneous and heterogeneous MTO/$H_2O_2$ systems: a novel approach for, oxidative desulfurization (ODS) of diesel fuel. *Appl. Catal., B:* **2009**, *89*, 239−245.
(49) Wei, S.; He, H.; Cheng, Y.; Yang, C.; Zeng, G.; Qiu, L. Performances, kinetics and mechanisms of catalytic oxidative desulfurization from oils. *RSC Adv.* **2016**, *6*, 103253−103269.
(50) Wang, D.; Liu, N.; Zhang, J.; Zhao, X.; Zhang, W.; Zhang, M. Oxidative desulfurization using ordered mesoporous silicas as catalysts. *J. Mol. Catal. A: Chem.* **2014**, *393*, 47−55.
(51) Ren, X.; Liu, Z.; Dong, L.; Miao, G.; Liao, N.; Li, Z.; Xiao, J. Dynamic catalytic adsorptive desulfurization of real diesel over ultra-stable and low-cost silica gel-supported $TiO_2$. *AIChE J.* **2018**, *64*, 2146−2159.
(52) Ji, P.; Drake, T.; Murakami, A.; Oliveres, P.; Skone, J. H.; Lin, W. Tuning Lewis acidity of metal-organic frameworks via perfluorination of bridging ligands: spectroscopic, theoretical, and catalytic studies. *J. Am. Chem. Soc.* **2018**, *140*, 10553−10561.
(53) Ahmed, I.; Jhung, S. H. Effective adsorptive removal of indole from model fuel using a metal-organic framework functionalized with amino groups. *J. Hazard. Mater.* **2015**, *283*, 544−550.
(54) Chakarova, K.; Strauss, I.; Mihaylov, M.; Drenchev, N.; Hadjiivanov, K. Evolution of acid and basic sites in UiO-66 and UiO-66-$NH_2$ metal-organic frameworks: FTIR study by probe molecules. *Microporous Mesoporous Mater.* **2019**, *281*, 110−122.

Downloaded from pubs.acs.org/acsodf/article-pdf/7/19/16288/10276166/ao1c05965.pdf by TALLINN TECHNICAL UNIV user on 25 September 2026


https://doi.org/10.1021/acsomega.1c05965
*ACS Omega* 2022, 7, 16288−16297

**Publication II**

**Barghi, B**., Mõistlik, T., Raag, A., Volokhova, M., Reile, I., Seinberg, L., Mikli, V. and Niidu, A., 2024. Deep Oxidative Desulphurization of Planar Compounds Over Functionalized Metal–Organic Framework UiO-66 (Zr): An Optimization Study. ACS omega, 9(22), pp.23329-23338.

ACS OMEGA

Open Access

This article is licensed under CC-BY 4.0

http://pubs.acs.org/journal/acsodf

Article

# Deep Oxidative Desulfurization of Planar Compounds Over Functionalized Metal−Organic Framework UiO-66(Zr): An Optimization Study

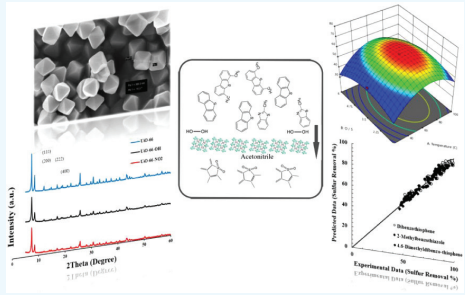
Bijan Barghi,* Tanel Mõistlik, Anastassia Raag, Maria Volokhova, Indrek Reile, Liis Seinberg, Valdek Mikli, and Allan Niidu

Cite This: *ACS Omega* 2024, 9, 23329−23338

Read Online

ACCESS | Metrics & More | Article Recommendations | * Supporting Information

**ABSTRACT:** This study aims to determine the catalytic activity and stability of ligand-modified UiO-66 with different functional groups (−$NO_2$, −OH) in deep oxidative desulfurization from a model fuel (MF). The planar sulfur compounds included dibenzothiophene (DBT), 2-methylbenzothiazole (2-MB), and 4,6-dimethyldibenzothiophene (4,6-DMDBT) in *n*-dodecane as the fuel phase. The synthesized functionalized metal−organic framework (MOF) samples were characterized by X-ray powder diffraction (XRD), Fourier transform infrared (FTIR), proton nuclear magnetic resonance ($^1$H NMR), scanning electron microscopy (SEM), thermogravimetric analysis (TGA), nitrogen adsorption−desorption analysis, and microwave plasma-atomic emission spectrometer (MP-AES). The experiment assessment and desulfurization reaction optimization were carried out by the central composite design methodology. Response surface methodology and analysis of variance were employed to evaluate the individual process factors, their interactions, and sulfur removal responses. The responses showed that the oxidation of the planar compounds declined following the sequence DBT > 2-MB 4,6-DMDBT for all the MOFs. The findings revealed that at 66.7 °C, 3.0 equiv of oxidative agent over sulfur and 9.7 of MOF over sulfur by weight achieved the highest removal efficiency of 98.68% DBT, 93.23% 2-MB, and 69.32% 4,6-DMDBT for UiO-66-$NO_2$ as a catalyst from the model fuel. It was also observed that UiO-66-$NO_2$ had a higher efficiency in deep oxidative desulfurization when compared to other UiO-66-based catalysts used in the current study. Under optimal conditions, all the MOFs showed acceptable catalytic activity and reusability after four runs, although gradual loss of activity was observed.




## 1. INTRODUCTION

One of the primary sources of air pollution is sulfur oxide emissions into the atmosphere from combustion of fossil fuels that leads to environmental and health problems, so improving deep desulfurization process is essential for producing ultraclean sulfur-free fuel.[1] Oxidative desulfurization (ODS) is a practical approach for removing planar sulfur compounds,[2] compared with hydrodesulfurization (HDS) reaction, which may be conducted under mild operating conditions.[3,4] ODS has a potential to reduce investments in equipment and hydrogen consumption.[5,6] There are other methods (e.g., photo-oxidation desulfurization (PODS) and oxidative-extractive desulfurization (OEDS)) employed for the deep desulfurization.[7,8]

The ODS process includes oxidation and extraction steps for sulfur compounds. The compounds are oxidized by an oxidant agent; the oxidized sulfurs may then be extracted from the fuel by using an appropriate polar solvent.[9] The oxidation of sulfur compounds is performed by different oxidant agents such as hydrogen peroxide, oxygen, or *tert*-butyl hydroperoxide.[10−12] Nevertheless, hydrogen peroxide is the most efficient oxidative agent among the others.[13,14] For fuel oxidative desulfurization reactions, a variety of catalysts have been applied, including porous materials with titanium,[15] metal oxides,[16] boron nitride,[17] reduced graphene oxide,[6] activated carbon,[18] zeolite,[19] and metal−organic frameworks (MOFs).[20] MOFs are three-dimensional coordination polymers containing organic linkers and metal nodes, forming an emerging class of porous materials for various applications. These substances exhibit both inorganic and organic flexibility. Additionally, groups that are attached to the linkers and metal node MOFs could be the catalytic active site for reactions.[21,22] Among MOFs, the porous zirconium terephthalate UiO-66 has been widely used as a catalyst because of its large surface area,

Received: December 13, 2023
Revised: May 9, 2024
Accepted: May 14, 2024
Published: May 23, 2024



© 2024 The Authors. Published by American Chemical Society



Downloaded from pubs.acs.org/acsodf/article-pdf/9/22/23329/4417267/ac3c09971.pdf by TALLINN TECHNICAL UNIV user on 25 September 2026

Table 1. Catalytic Oxidation of Planar Sulfur Compounds over MOFs by Using $H_2O_2$

| No. | MOF | sulfur compound (removal efficiency % in optimum temperature) | fuel base | temperature (°C) | time (minute) | reference |
|---|---|---|---|---|---|---|
| 1 | UiO-66 | DBT (55%) | *n*-octane | 60 | 120 | 23 |
| 2 | UiO-66-D[a] | DBT (78%) | *n*-octane | 60 | 120 | 23 |
| 3 | UiO-66 | Th[b] (47%), BT[c] (60%), DBT (98%), 4,6-DMDBT (69%) | *n*-octane | 30−70 | 60−180 | 24 |
| 4 | UiO-66 | DBT (93%) | *n*-octane | 50 | 240 | 25 |
| 5 | UiO-66-MW[d] | DBT (95%) | *n*-octane | 50 | 240 | 25 |
| 6 | UiO-66 | DBT (69%) | *n*-octane | 40−70 | 120 | 27 |
| 7 | UiO-66-$NH_2$ | DBT (38%) | *n*-octane | 40−70 | 120 | 27 |
| 8 | UiO-66-$NO_2$ | DBT (96%) | *n*-octane | 40−70 | 120 | 27 |
| 9 | UiO-66-Br | DBT (78%) | *n*-octane | 40−70 | 120 | 27 |
| 10 | UiO-66 | DBT (77%) | *n*-octane | 60 | 120 | 28 |
| 11 | UiO-66-$NH_2$ | DBT (68% | *n*-octane | 60 | 120 | 28 |
| 12 | UiO-66-$NO_2$ | DBT (90%) | *n*-octane | 60 | 120 | 28 |
| 13 | UiO-66-g[e] | DBT (96%), 4,6-DMDBT(95%) | *n*-octane | 60 | 120 | 28 |
| 14 | UiO-66-$NH_2$-g[e] | DBT (70%), 4,6-DMDBT(48%) | *n*-octane | 60 | 120 | 28 |
| 15 | UiO-66-$NO_2$-g[e] | DBT (97%), 4,6-DMDBT(96%) | *n*-octane | 60 | 120 | 28 |
| 16 | UiO-66-$NH_2$ | DBT (87.5%) | *n*-dodecane | 20−100 | 150 | 30 |
| 17 | UiO-66 | DBT (100%), 4-MDBT (100%), 4,6-DMDBT (100%) | *n*-octane | 50 | 60 | 31 |
| 18 | UiO-66 | DBT (84%), 4,6-DMDBT(50%) | *n*-octane | 60 | 120 | 32 |
| 19 | UiO-66-free[f] | DBT (100%), 4,6-DMDBT(100%) | *n*-octane | 60 | 120 | 32 |
| 20 | UiO-66 | BT (82%) | *n*-heptane | 40 | 20 | 33 |
| 21 | UiO-66 | BT (64%), DBT (82%), 4-MDBT (63%), 4,6-DMDBT (42%) | *n*-octane | 50 | 240 | 34 |
| 22 | UiO-66 | DBT (100%) | *n*-octane | 30 | 60 | 35 |

[a]With defect [b]Thiophene [c]Benzothiophene [d]Microwave advanced synthesis [e]Green [f]Solvent-free

tunable porosity, stability, and reusability.[23,24] Modification of UiO-66(Zr) by adding different ligands, in this case functionalized terephthalic acid, provided a promising route to modifying the chemical and physical characteristics of the MOF;[25−27] it also could increase the Lewis-basic sites in the structure and make functionalized UiO-66 an appropriate option for adsorption, drug delivery, and heterogeneous catalyst.[28,29]

In previous studies, several metal−organic frameworks have been found to be active catalysts for oxidative desulfurization; however, it was claimed that UiO-66 obtained high sulfur removal efficiency in a shorter period of the process.[30] Previous reports on adsorption and oxidation efficiency of pristine-, amino-, and nitro-modified UiO-66 are summarized in Table 1:

Thus, far, there has been one report in our previous work, employing UiO-66-$NH_2$ as a catalyst on reaction variable assessment in the ODS reaction;[30] this research employed a more electron-rich ligand, aminoterephthalic acid, to modulate the catalytic activity of nodes and increase the potential for hydrogen bonding in pores via the $NH_2$ group.

Currently, a range of diverse catalysts have been identified for ODS reactions, with limited studies involving functionalized MOF UiO-66. There have been no investigations on the process condition optimization of different functionalized UiO-66 (-$NO_2$, −OH) as in the ODS process. In this study, pristine UiO-66(Zr), UiO-66-$NO_2$, and UiO-66-OH were prepared by a solvothermal procedure for the oxidative desulfurization reaction. The synthesized MOFs were characterized and analyzed by X-ray powder diffraction (XRD), Fourier transform infrared (FTIR), proton nuclear magnetic resonance ($^1$H NMR), scanning electron microscopy (SEM), thermogravimetric analysis (TGA), nitrogen adsorption-desorption analysis, and microwave plasma-atomic emission spectrometer (MP-AES). The effect of individual and interaction of process variables were completely evaluated, which led to achieving the optimum values for all the MOFs in the ODS reaction. A polynomial quadratic model was designed to fully visualize the significance of the reaction temperature, oxidant agent mass ratio, and MOF amount, from which the response surface methodology (RSM) was adopted to determine the optimum values.

## 2. MATERIAL AND METHOD

**2.1. Material.** Zirconium(IV) chloride ($ZrCl_4$, 98%, Acros), terephthalic acid (99%, Acros), 2-hydroxyterephthalic acid (99%, Acros), nitroterephthalic acid (99%, Acros), hydrochloric acid (HCl, 36%, Honeywell), *N*,*N*-dimethylformamide (DMF, 99.5%, Fisher), ethanol ($C_2H_5OH$, 99.9%, Honeywell), acetonitrile (99.9%, Honeywell), *n*-dodecane (99%, Alfa Aesar), hydrogen peroxide ($H_2O_2$, 30%, Alfa Aesar), dibenzothiophene (98%, Acros), 2-methylbenzothiazole (99%, Acros), and 4,6-dimethyldibenzothiophene (97%, Alfa Aesar) were used without any further purification.

**2.2. MOF Synthesis.** MOFs were synthesized as originally described.[36] Shortly, 1 g of $ZrCl_4$ and the respective ligand (0.98 g terephthalic acid (BDC), 1.08 g 2-hydroxyterephthalic acid, and 1.25 g nitroterephthalic acid for UiO-66, UiO-66-OH, and UiO-66-$NO_2$, respectively) were dissolved in 120 mL DMF and 8 mL HCl 36% and then sonicated for 35 min. The prepared solution was heated at 80 °C in an oven for 24 h. After cooling to room temperature, the sample was washed with DMF and ethanol and dried by heating under a 600 mbar pressure at 80 °C on a rotary evaporator.

**2.3. Characterization Methods.** X-ray powder diffraction (XRD) results were recorded on a X'Pert3 Powder (Malvern Panalytical) with a detector Cu K$\alpha$ radiation with wavelength $\lambda$= 0.154 nm. Fourier transform infrared (FT-IR) spectra were recorded of the functional moieties of the samples on Nicolet iS50 FTIR spectrometric analyzer. The attenuated total reflectance (ATR-FTIR) sampling methodology was utilized for the direct examination of solid samples of UiO-66 derivate

Downloaded from pubs.acs.org/acsodf/article-pdf/9/22/23329/4417267/ac3c09971.pdf by TALLINN TECHNICAL UNIV user on 25 September 2026


https://doi.org/10.1021/acsomega.3c09971
ACS Omega 2024, 9, 23329−23338

Table 2. Independent Test Variables at Five Levels Were Used in the Central Composite Design for Three Different MOFs, UiO-66(Zr), UiO-66-OH, and UiO-66-$NO_2$[a]

| | | | coded variable levels | | | | |
|---|---|---|---|---|---|---|---|
| parameter | code | units | (-$\alpha$) | (−1) | (0) | (+1) | (+$\alpha$) |
| temperature | $X_1$ | °C | 20 | 36.21 | 60 | 83.78 | 100 |
| oxd./sul. mass ratio | $X_2$ | (mg/mg) | 0.5 | 1.61 | 3.25 | 4.89 | 6 |
| cat./sul. mass ratio | $X_3$ | (mg/mg) | 0.5 | 3.44 | 7.75 | 12.06 | 15 |

[a]UiO-66: $X_4[0]$, UiO-66-OH: $X_4[1]$ , UiO-66-NO2: $X_4[2]\alpha$: 1.68

MOFs. Scanning electron microscopy (SEM) images were measured on a Zeiss FEG-SEM Ultra-55. Thermogravimetric analysis (TGA) was carried out on a Mettler-Toledo TGA 1. An Agilent 4200 microwave plasma atomic emission spectrometer was utilized to measure the elemental ratios and purity of a sample using microwave plasma atomic emission spectroscopy (MP-AES). At a sample temperature of 25 °C, digested MOF samples were evaluated by proton NMR spectroscopy on a 500 MHz Agilent DD2 NMR spectrometer with a 5 mm ID PFG probe head. Nitrogen adsorption−desorption isotherms were measured at 87 K on a Quantachrome Autosorb-iq device after the samples were degassed at 408 K for 18 h under vacuum, and then, specific surface areas were calculated using Quantachrome AsiQwin 5.23 software and BET method.

**2.4. Catalyst Test.** ODS reactions were conducted in a 22 mL reactor. For the model fuel (MF), 1000 ppm of each sulfur compound (DBT, 2-MB, and 4,6-DMDBT) was dissolved in *n*-dodecane. To this solution in the reactor, acetonitrile (3 mL) was added as the polar phase in a 1:1 ratio by volume. According to the experimental design, the specified amount of MOF was added to the reactor; hydrogen peroxide was supplied after the reactor was heated to a predefined temperature. The polar and fuel phases were separated after the reaction had completed and then analyzed by a Shimadzu QP2010 plus GC to measure the sulfur compounds. The sulfur removal efficiency was calculated according to eq 1:

$$\text{Sulfur Removal}\ (\%) = (S_0 - S_t)/S_0 \quad (1)$$

where $S_0$ and $S_t$ correspond to the sulfur concentrations in MF at the beginning and end of the reaction, respectively.

**2.5. Design of Experiments.** The oxidative desulfurization efficiency was investigated with the response surface methodology employing the central composite design (CCD).[37] The parameters assessed were the reaction temperature (A), oxidative agent to sulfur mass ratio (B), MOF mass dosage (C), and selected MOF (D). The first three variables are designated at five levels as the numerical parameters and the fourth variable as a categorical parameter. The analysis of variance (ANOVA) was performed to evaluate the factors for the fitted quadratic model, and the fitness of the polynomial model was evaluated by the coefficient of determination $R^2$.[38] The F-test assessed the model and parameter significance, and the p-value with a specified confidence level was used to verify the model terms. The second-order polynomial equation is given in eq 2:

$$f(X) = \beta_0 + \sum_{i=1}^{3} \beta_i X_i + \sum_{i=1}^{3} \sum_{j=1}^{3} \beta_{ij} X_i X_j \quad (2)$$

$X_i$ and $X_j$ are the coded values of variables, and $\beta_0$, $\beta_i$, and $\beta_{ij}$ are the constant, linear, and interaction coefficients. Referring to the central composite design, 17 experimental runs were carried out including axial, factorial, and central runs. The oxidative sulfur removal reactions were conducted for each UiO-66 MOF. Table 2 summarizes the work domain classes for four parameters.

## 3. RESULTS AND DISCUSSION

**3.1. Characterization.** Figure 1 shows how XRD was employed to assess the crystallinity and structure of the MOFs.

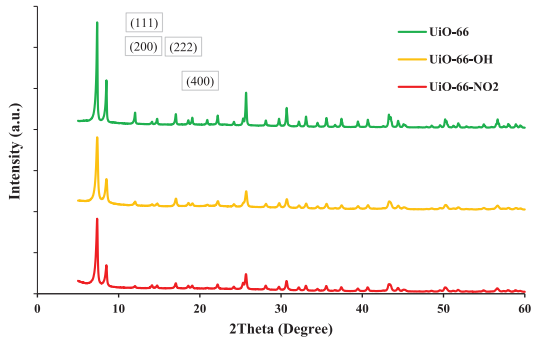



Figure 1. XRD powder patterns of UiO-66, UiO-66-OH, and UiO-66-$NO_2$.

The sample diffraction peaks of (111), (200), (022), (222), (400), (115), and (006) in the XRD patterns and indicates that the UiO-66, UiO-66-OH, and UiO-66-$NO_2$ had been synthesized successfully.[39] Synthesized UiO-66 derivatives were analyzed by FTIR, as shown in Figure 2. The IR bands for the three MOFs are in the same position at 660 $cm^{-1}$ (C−H vibrations in BDC aromatic ring), 766 $cm^{-1}$ (O−H

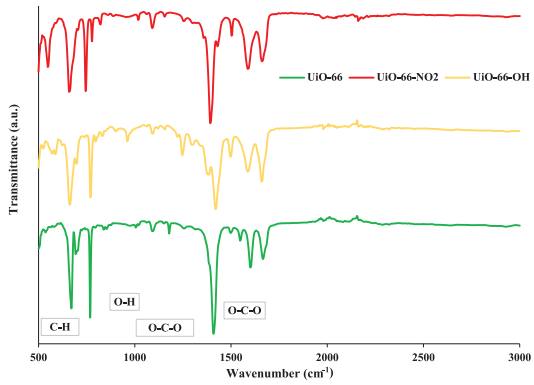



Figure 2. FT-IR spectrum of UiO-66, UiO-66-OH, and UiO-66-$NO_2$.



https://doi.org/10.1021/acsomega.3c09971
ACS Omega 2024, 9, 23329−23338

Downloaded from pubs.acs.org/acsodf/article-pdf/9/22/23329/4417267/ao3c09971.pdf by TALLINN TECHNICAL UNIV user on 25 September 2026

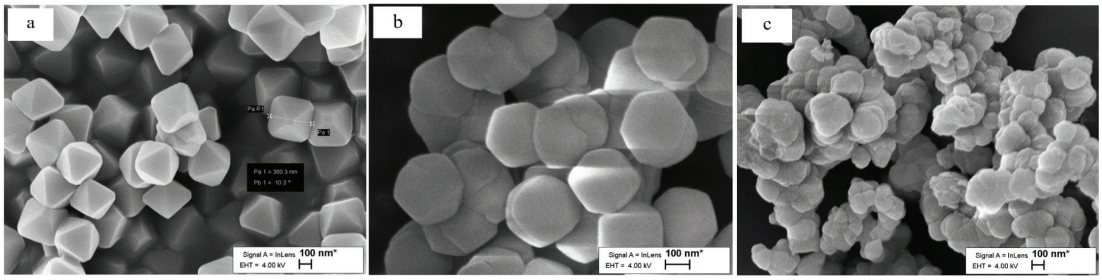



**Figure 3.** Typical SEM images of (a) UiO-66, (b) UiO-66-OH, and (c) UiO-66-$NO_2$.

vibrations in BDC aromatic ring), 1400 $cm^{-1}$ (O−C−O symmetric stretch), and 1570 $cm^{-1}$ (O−C−O asymmetric stretch).[40,41]

As illustrated in Figure 3, the SEM picture of the UiO-66 MOF exhibits a uniform octagonal shape. Based on the images, the particle sizes generally converged between 350 and 360 nm (Figure 3a). However, UiO-66-OH and UiO-66-$NO_2$ demonstrated a higher irregularity of octagonal morphology with a crystal size between 340 and 370 nm (Figure 3b,c).

Figure 4 demonstrates the $^1$H NMR characterization of the prepared UiO-66 after digestion with NaOD/$D_2O$. The peaks

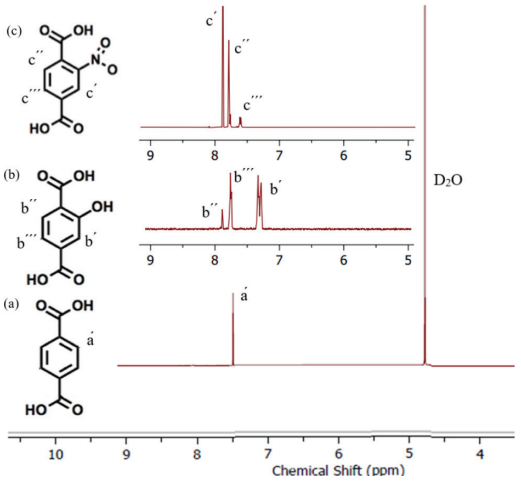



**Figure 4.** $^1$H NMR spectra of the prepared (a) UiO-66, (b) UiO-66-OH, and (c) UiO-66-$NO_2$ (NMR analyzed the bulk purity of solution after adding 650 uL of $D_2O$ to the digested solution of MOF sample in 10 drops of NaOD).

of UiO-66 show a signal at 7.48 ppm attributed to the BDC structure of the ligands.[42] NMR analysis of the other functionalized UiO-66 displays three signals related to the hydroxyterephthalic acid and nitroterephthalic acid linkers in UiO-66-OH and UiO-66-$NO_2$, respectively. The integrations of the NMR peaks for UiO-66 are illustrated in Figure S1.

Thermogravimetry analysis of UiO-66 derivates in Figure 5 shows a weight loss at 45−100 °C attributed to removing water and ethanol, and the other mass loss was related to eliminating *N*,*N*-dimethylformamide. At 520 °C, structure decomposition and (Zr) oxo-clusters dehydroxylation were the

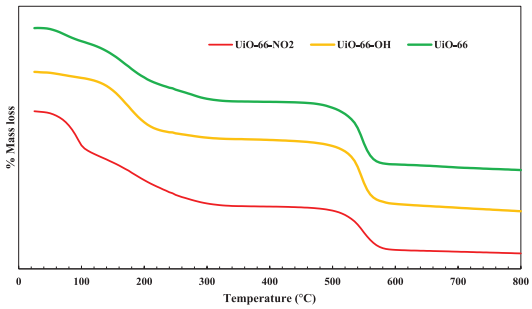



**Figure 5.** Thermogravimetry Curves of UiO-66, UiO-66-OH, and UiO-66-$NO_2$. First mass loss (<100 °C), second mass loss (100−520 °C), third mass loss (>520 °C), UiO-66:16.9%, 27.11%, and 20.8%, UiO-66-OH: 3.2%, 29.3%, and 31.0%, UiO-66-$NO_2$: 6.5%, 27.9%, and 30.4%, respectively.

reasons for final mass loss.[43] Table 3 indicates the summarized isotherm data and the amount of zirconium in MOFs, as

**Table 3. Zirconium Content and Textural Properties of Synthesized MOFs**

| MOF | amount of zirconium (wt %) | BET surface area ($m^2$/g) | total pore volume (cc/g) | pore width (nm) |
|---|---|---|---|---|
| UiO-66 | 26.2 | 1649 | 0.605 | 1.11 |
| UiO-66-OH | 25.1 | 852 | 0.286 | 1.38 |
| UiO-66-$NO_2$ | 24.2 | 776 | 0.429 | 1.63 |

measured by MP-AES. BET surface area of UiO-66 is 1649 $m^2$/g higher than UiO-66-OH and UiO-66-$NO_2$ (852 $m^2$/g and 776 $m^2$/g). Additionally, UiO-66-$NO_2$ observed a higher pore width of about 1.63 nm. Figure S2 summarizes the isotherm data for UiO-66 pristine and its derivatives.

**3.2. Effect of Parameters.** Based on the Response Surface Methodology, experiments were conducted according to the given experimental design (Table 2). For UiO-66, UiO-66-OH, and UiO-66-$NO_2$, the results of the defined factors, along with reaction temperature, oxidant over sulfur (Oxd./Sul. "mg/mg"), and MOF dosage over sulfur (cat./sul, mg/mg), were assessed at the given process time. As a result, Table S1 includes parameters, obtained values for the model, and experimental results. Three polynomial equations with coded factors for dibenzothiophene (DBT), 2-methylbenzothiazole (2-MB), and 4,6-dimethyldibenzothiophene (4,6-DMDBT) were derived by using multiple regression analysis to the

Downloaded from pubs.acs.org/acsodf/article-pdf/9/22/23329/4417267/ao3c09971.pdf by TALLINN TECHNICAL UNIV user on 25 September 2026


https://doi.org/10.1021/acsomega.3c09971
ACS Omega 2024, 9, 23329−23338

experimental responses, as indicated in eqs 3, 4, and 5, respectively.

$$\text{DBT Removal (wt\%)} = 95.66 + 5.16(X_1) + 0.86(X_2) + 1.59(X_3) - 2.13(X_4[1]) + 0.40(X_4[2]) - 3.22(X_1)(X_2) + 0.45(X_1)(X_3) - 1.28(X_2)(X_3) - 9.02(X_1)2 - 1.65(X_2)2 - 1.74(X_3)2 + 0.93(X_1)(X_4[1]) - 0.15(X_1)(X_4[2]) - 0.33(X_2)(X_4[1]) + 0.35(X_2)(X_4[2]) - 0.07(X_3)(X_4[1]) - 0.54(X_3)(X_4[2]) \quad (3)$$

$$\text{2-MB Removal (wt\%)} = 90.31 + 4.60(X_1) - 0.05(X_2) + 1.05(X_3) - 1.46(X_4[1]) - 0.18(X_4[2]) - 3.04(X_1)(X_2) - 0.04(X_1)(X_3) - 2.22(X_2)(X_3) - 7.53(X_1)2 - 0.67(X_2)2 - 1.10(X_3)2 + 0.16(X_1)(X_4[1]) + 0.26(X_1)(X_4[2]) + 0.39(X_2)(X_4[1]) + 0.07(X_2)(X_4[2]) - 0.26(X_3)(X_4[1]) + 0.14(X_3)(X_4[2]) \quad (4)$$

$$\text{4,6-DMDBT Removal (wt\%)} = 67.65 + 2.89(X_1) + 0.51(X_2) + 1.55(X_3) - 1.91(X_4[1]) + 0.53(X_4[2]) - 0.02(X_1)(X_2) + 0.55(X_1)(X_3) - 0.19(X_2)(X_3) - 5.86(X_1)2 - 4.25(X_2)2 - 2.14(X_3)2 + 0.31(X_1)(X_4[1]) - 0.23(X_1)(X_4[2]) - 0.28(X_2)(X_4[1]) + 0.72(X_2)(X_4[2]) + 0.24(X_3)(X_4[1]) + 0.28(X_3)(X_4[2]) \quad (5)$$

F-values and coefficient of determination ($R^2$) were assessed by multiple regression and polynomial model fitness, respectively. The mathematical quadratic model was fitted by ANOVA to calculate the efficiency of sulfur removal. F-values of 18.24, 19.81, and 66.42 were obtained for 2-methylbenzothiazole (2-MB), dibenzothiophene (DBT), and 4,6-dimethyldibenzothiophene (4,6-DMDBT), respectively, as summarized in Table S2, and imply that for all cases, there are less than 0.01% chances that the particular F-value could occur due to noise. Additionally, a P-value lower than 0.05 demonstrated that experimental design models for sulfur removals are statistically significant. The coefficient of determination values confirmed that the model is successfully fitted to the data. ($R^2$ values are 0.904, 0.911, and 0.921 for 2-MB, DBT, and 4,6-DMDBT, respectively).

The comparison between experimental and model values is shown in Figure 6; the curve demonstrates that model-predicted values are highly correlated with the obtained responses in the sulfur elimination yield. The root-mean-square deviation of the experimental results and predicted model was 3.4%.

The normal plot of the residuals in Figure S3 demonstrates the reliability of the model. The straight lines for DBT, 2-MB, and 4,6-DMDBT indicate that the residuals have a normal distribution. This study was carried out to determine the impact of individual factors and their interactions by employing the response surface methodology. The effect of reaction temperature, oxd./sul. ratio, and cat./sul. ratio for UiO-66, UiO-66-OH, and UiO-66-$NO_2$ on the efficiency of sulfur removal are displayed in 3D surface plots (Figures 7, S4, and S5, respectively). Figure 7a shows the effect of temperature and oxd./sul. on the ODS of 2-MB for UiO-66. The highest yield of 2-MB oxidation (89.96%) was obtained at the oxd./sul.

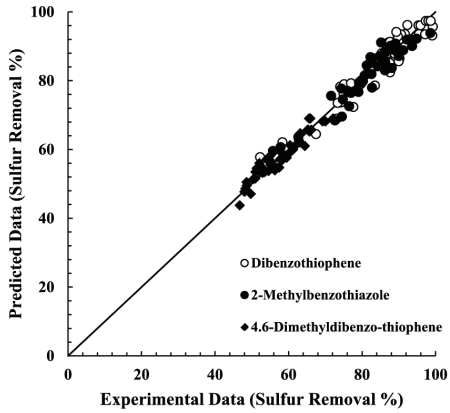



**Figure 6.** Comparison between model predicted and experimental values of sulfur removal efficiency.

mass ratio of 1.5:1.7 and a temperature range of 70−73 °C. Figure 7b shows 3D plots between the temperature and MOF dosage, illustrating that two factors have a significant impact on 2-MB oxidation. The results indicated that in the temperature range between 60 and 70 °C, the higher catalyst to sulfur mass ratio between 11.5 and 12.5 was in favor of 2-MB ODS efficiency.

Figure 8c,d demonstrate the effect of oxd./sul. and cat./sul. ratio versus temperature for the DBT ODS reaction. It shows that the three parameters have visible effects on oxidation. For the case of interaction between reaction temperature and oxd./sul. ratio (Figure 7c), at the oxd./sul. ratio of 0.5:2.3 and a temperature of 71 °C, the maximum efficiency of 4,6-dimethyldibenzothiophene removal was observed (95%). Furthermore, the calculated optimal amount of cat./sul. was 10.8 (mg/mg) for the highest DBT removal efficiency (Figure 7d).

At a particular oxidant over sulfur ratio range of 1.0:3.0, as shown in Figure 7e, an increased 4,6-DMDBT oxidation efficiency was observed when the temperature was raised from 65 to 72 °C. However, the removal yield of 4,6-DMDBT declined with temperature increase over 73 °C. Because the oxidative desulfurization process is endothermic,[44] raising the temperature promotes the sulfur removal rate by increasing the molecular mobility of reaction components. In contrast, at higher temperatures, the rate of oxygen peroxide decomposition also increases, and as a result, the oxidation reaction rate falls due to the oxidant concentration decrease.[45] When the oxd./sul. mass ratio grows from 2.4 to 3.3 at a specified temperature, the 4,6-DMDBT removal rate increases and then starts to decrease as the oxd./sul. ratio rises to 6 (Figure 7e). On the contrary, the removal of sulfur was more efficient if there was a higher amount of oxidant.[46,47]

According to the ANOVA analysis, oxd./sul = 3.0 was the optimum value, and Figure 7f illustrates the interaction between reaction temperature and cat./sul on the 4,6-DMDBT removal yield. Perceptibly, the highest sulfur removal efficiency (about 64%) was achieved at the temperature of 60−75 °C and cat./sul of 9.8−10.5. However, further rising cat./sul to 15, the removal efficiency is decreased because catalytic activity of the excessive MOF in the oxidation process is much lower due to aggregation.[48,49]

Downloaded from pubs.acs.org/acsodf/article-pdf/9/22/23329/4417267/ao3c09971.pdf by TALLINN TECHNICAL UNIV user on 25 September 2026


https://doi.org/10.1021/acsomega.3c09971
ACS Omega 2024, 9, 23329−23338

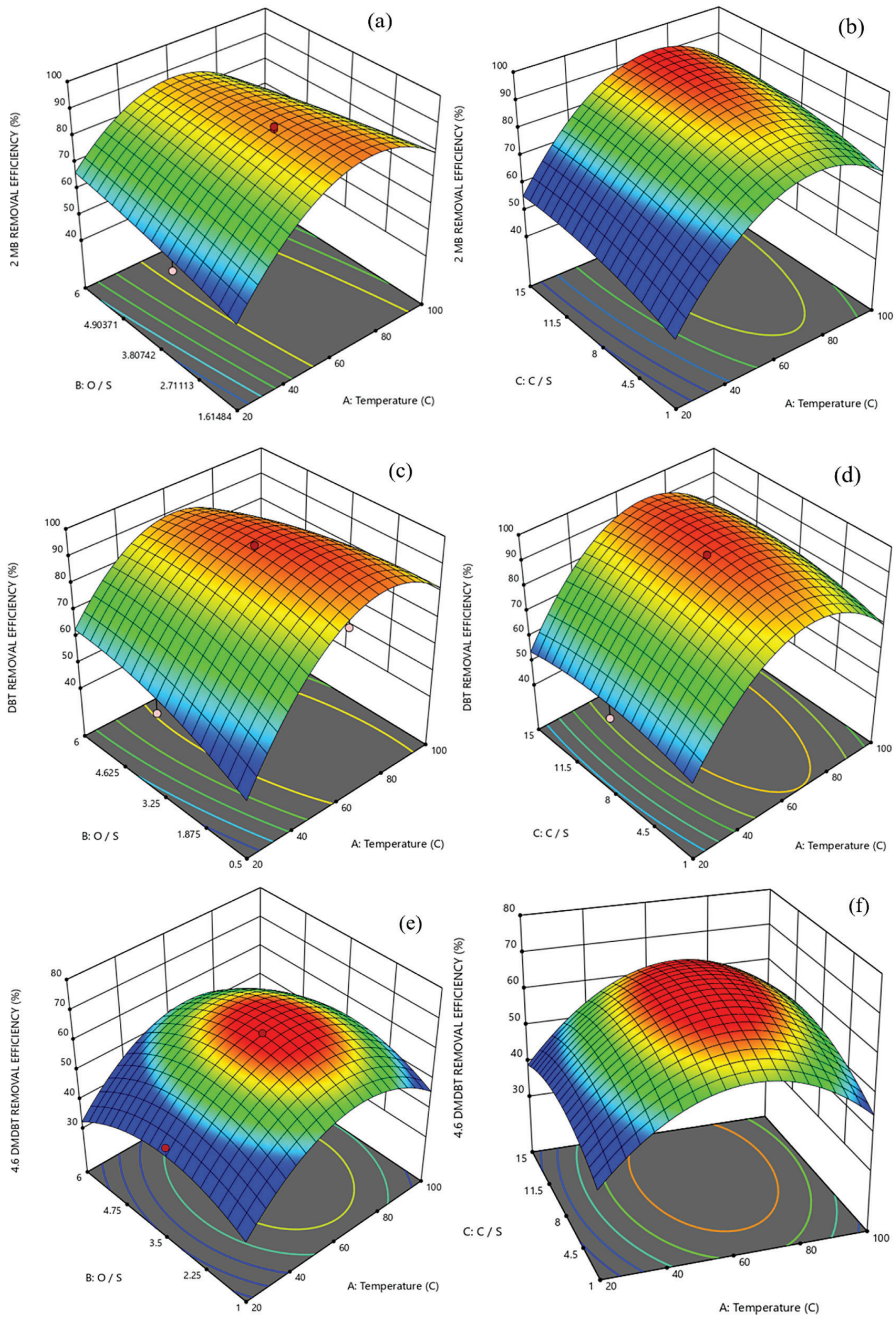



**Figure 7.** 3D plot presenting the performance of UiO-66 MOF on the removal of sulfur from the MF. (a) Sulfur removal efficiency: 2-MB. Constant parameter: Cat./Sul. mass ratio ($X_3$). Constant parameter value (mg/mg): 9.8. (b) Sulfur removal efficiency: 2-MB. Constant parameter: Oxd./Sul. mass ratio ($X_2$). Constant parameter value (mg/mg): 2.9. (c) Sulfur removal efficiency: DBT. Constant parameter: Cat./Sul. mass ratio ($X_3$). Constant parameter value (mg/mg): 9.8. (d) Sulfur removal efficiency: DBT. Constant parameter: Oxd./Sul. mass ratio ($X_2$). Constant parameter value (mg/mg): 2.9. (e) Sulfur removal efficiency: 4,6-DMDBT. Constant parameter: Cat./Sul. mass ratio ($X_3$). Constant parameter value (mg/mg): 9.8. (f) Sulfur removal efficiency: 4,6-DMDBT. Constant parameter: Oxd./Sul. mass ratio ($X_2$). Constant parameter value (mg/mg): 2.9.



https://doi.org/10.1021/acsomega.3c09971
*ACS Omega* 2024, 9, 23329−23338

Downloaded from pubs.acs.org/acsodf/article-pdf/9/22/23329/4417267/ao3c09971.pdf by TALLINN TECHNICAL UNIV user on 25 September 2026

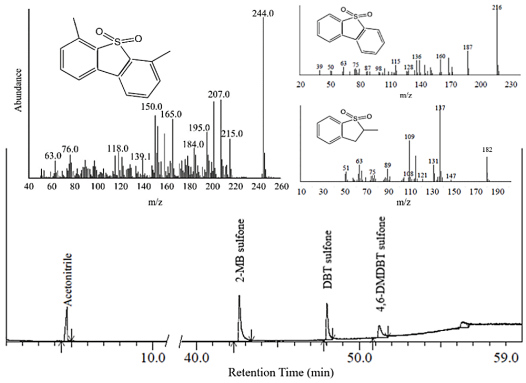



**Figure 8.** MS spectra of the oxidized products of 2-MB ($m/z$: 182), DBT ($m/z$: 216), and 4,6-DMDBT ($m/z$: 244).

Additionally, Figures S4 and S5 illustrate the 3D surface response graphs for UiO-66-OH and UiO-66-$NO_2$, respectively. As shown, UiO-66-$NO_2$ achieved higher sulfur removing (for three sulfur planar compounds) in 150 min of reaction time, and after UiO-66-OH, UiO-66, and UiO-66-$NH_2$,[31] respectively.

The prominent parameters in the desulfurization process are the electron density of the sulfur atoms and the steric hindrance surrounding the sulfur atoms. Oxidative desulfurization benefits from a greater electron density and a lower steric hindrance. Sulfur atoms in 4,6-dimethyldibenzothiophene, dibenzothiophene, and 2-methylbenzothiazole have electron densities of 5.760, 5.758, and 5.739, respectively.[50]

Because the electron densities on the sulfur atoms of 4,6-dimethyldibenzothiophene and dibenzothiophene are comparable, the steric hindrance surrounding the sulfur atom had a major role in the oxidation. As a result, dibenzothiophene indicated a larger conversion for derivatives of UiO-66 because there was less steric hindrance around the sulfur atom among the planar compounds. The low activity for 4,6-dimethyldibenzothiophene is due to the larger size, than DBT and 2-MB, which could mostly interact with the external surface of the MOFs.[51] Thus, the activity with UiO-66 and its derivatives followed the sequence DBT > 2-MB > 4,6-DMDBT.

**3.3. Parameter Optimization.** The optimum reaction conditions for the removal of sulfur-containing compounds from MF have been obtained using the response surface methodology in the CCD model. The optimal values of three parameters are summarized in Table 4 for achieving the maximum sulfur removal as well as the model desirability.

The impact of UiO-66 on DBT removal efficiency is summarized in Table 5. Regarding the extraction and oxidation (without MOF), the results indicated that the removal of sulfur

**Table 5. Catalytic Oxidative and Extractive Removal of Dibenzothiophene with and without UiO-66 in the Presence of $H_2O_2$ from the Model Fuel**

| | DBT removal at different temperatures (%) | | | |
|---|---|---|---|---|
| | 36 °C | 60 °C | 68 °C | 84 °C |
| UiO-66 | 75% | 94% | 95% | 91% |
| No catalyst[a] | 25% | 32% | 34% | 34% |

[a]Reaction condition: 3 mL of MF, 13.1 μL of $H_2O_2$ (oxd./sul. = 3.0), 3 mL of polar phase, for 150 min.

is significantly less efficient compared to the runs with catalysts when maintaining the oxd./sul. ratio at 3.0 in four different temperature runs. Compared to the previous study,[30] highest DBT removal efficiency achieved was 89.7% when UiO-66-$NH_2$ (in the conditions of 72.6 °C temperature, 1.62 O/S mass ratio mg/mg, and 12.1 C/S mass ratio mg/mg) was used as the catalyst, which is lower than the yields in the case of UiO-66.

Upon the oxidative process and separation of the polar phase, the oxidation product of 2-MB, DBT, and 4,6-DMDBT were analyzed by gas chromatography, as shown in Figure 8. From the analysis results, the sulfones of 2-MB, DBT, and 4,6-DMDBT have been detected.

**3.4. Reusability of MOF.** The recovery of the MOF is a factor in industrial utilization and economic issues. Reusability of the prepared MOFs was investigated by conducting four catalytic oxidation tests at 67 °C, cat./sul.= 9.8, and oxd./sul. = 3.0 in the optimum point. Centrifugation was utilized to separate the catalyst from the liquid phase and recover it following each experiment. The separated catalyst was washed with acetonitrile and dried at 100 °C for 12 h in the oven at atmospheric pressure and then employed in the following catalytic oxidation reaction. Sulfur removal efficiency for four multiple reactions demonstrates (Figure 9) that with a nearly

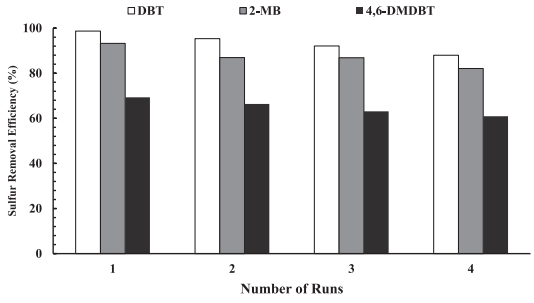



**Figure 9.** Sulfur removal yield on UiO-66-$NO_2$ catalyst in four cycles (3 mL of MF, 62 mg of catalyst (cat./sul.= 9.8), 13.1 μL of $H_2O_2$ (oxd./sul. = 3.0), 3 mL of polar phase, 150 min, at 67 °C).

**Table 4. Obtained Optimal Values for UiO-66, UiO-66-OH, and UiO-66-$NO_2$ in Achieving Highest Sulfur Removal, Standard Uncertainties (u) are u (T) = ± 1 °C; u (Oxd./Sul. Mass Ratio) = ± 0.01; u (Oxd./Sul. Mass Ratio) = ± 0.01 wt %; u (Yield) = ± 0.01 wt %**

| | optimum value | | | | | | |
|---|---|---|---|---|---|---|---|
| catalyst | temperature (°C) | oxd./sul.ratio (−) | cat./sul.ratio (−) | 2-MB removal (%) | DBT removal (%) | 4,6-DMDBT removal (%) | desirability |
| UiO-66 | 67.9 | 3.02 | 9.84 | 89.96 | 95.09 | 66.51 | 0.828 |
| UiO-66-OH | 66.8 | 3.21 | 9.71 | 91.26 | 96.94 | 68.90 | 0.883 |
| UiO-66-$NO_2$ | 66.7 | 2.97 | 9.75 | 93.23 | 98.68 | 69.33 | 0.916 |



https://doi.org/10.1021/acsomega.3c09971
ACS Omega 2024, 9, 23329−23338

Downloaded from pubs.acs.org/acsodf/article-pdf/9/22/23329/4417267/ao3c09971.pdf by TALLINN TECHNICAL UNIV user on 25 September 2026

10.8% decrease, the initial removal yield was retained, descending from 98.7 to 93.3%, 69.3 to 88.0%, and 82.1 to 61.0% for DBT, 2-MB, and 4,6-DMDBT, respectively. The deactivation mechanism of UiO-66 active sites for sequential cycles has been previously reported.[30,52] The reusability of UiO-66-OH and UiO-66 MOFs is shown in Figure S6.

## 4. CONCLUSION

Metal Organic Framework UiO-66 and its derivatives were prepared by solvothermal synthesis. The prepared catalysts were characterized by FTIR, proton NMR, XRD, SEM, TGA, BET, and MP-AES analyses. Response surface methodology and central composite design were employed to measure the impact of reaction conditions, temperature ($X_1$), oxidant mass ratio ($X_2$), MOF mass ratio ($X_3$), and UiO-66-x ($X_4$) on ODS efficiency. The obtained F-value and coefficient of determination ($R^2$) implied that experimental and predicted results by the model were fitted at an acceptable level. The sulfur removal efficiency could reach >95%, > 90%, and >67% of DBT, 2-MB and 4,6-DMDBT, respectively, in 66−68 °C, oxd./sul. ratio: 3.0−3.2, and cat./sul. ratio: 9.7−9.8 for MF (1000 ppm each sulfur content) for three employed MOFs. UiO-66-$NO_2$ exhibited higher catalytic activity in the deep oxidative desulfurization due to the presence of more electron-accepting group in its ligand structure. MOFs exhibited high reusability and maintained their activity over multiple runs in the oxidation of planar sulfur compounds.

## ■ ASSOCIATED CONTENT

### Supporting Information

The Supporting Information is available free of charge at https://pubs.acs.org/doi/10.1021/acsomega.3c09971.

Fundamental characterizations and analysis result of response surface methodology (Table S1); analysis of variance for the quadratic model of sulfur planal removal efficiency (Table S2); $^1$H-NMR spectrum of pristine UiO-66 (Integrations of the NMR peaks) (Figure S1); $N_2$ adsorption isotherms by the BET analysis of the UiO-66 derivate composite (Figure S2); externally studentized residuals versus normal probability of the model for (a) DBT, (b) 2-MB, and (c) 4,6-DMDBT removal efficiency (Figure S3); 3D plot presenting the performance of UiO-66-OH MOF on the removal of sulfur from the MF (Figure S4) (PDF)

## ■ AUTHOR INFORMATION


### Corresponding Author

**Bijan Barghi** − *Virumaa College School of Engineering, Tallinn University of Technology, Kohtla-Järve 30322, Estonia;* orcid.org/0000-0001-9577-3302; Email: bijan.barghi@taltech.ee

### Authors

**Tanel Mõistlik** − *Virumaa College School of Engineering, Tallinn University of Technology, Kohtla-Järve 30322, Estonia*

**Anastassia Raag** − *Virumaa College School of Engineering, Tallinn University of Technology, Kohtla-Järve 30322, Estonia*

**Maria Volokhova** − *National Institute of Chemical Physics and Biophysics, Tallinn 12618, Estonia;* orcid.org/0000-0002-6854-4042

**Indrek Reile** − *National Institute of Chemical Physics and Biophysics, Tallinn 12618, Estonia;* orcid.org/0000-0003-3278-7947

**Liis Seinberg** − *National Institute of Chemical Physics and Biophysics, Tallinn 12618, Estonia*

**Valdek Mikli** − *Department of Materials and Environmental Technology, Tallinn University of Technology, Tallinn 19086, Estonia*

**Allan Niidu** − *Virumaa College School of Engineering, Tallinn University of Technology, Kohtla-Järve 30322, Estonia;* orcid.org/0000-0003-3406-9869

Complete contact information is available at: https://pubs.acs.org/10.1021/acsomega.3c09971


### Notes

The authors declare no competing financial interest.

## ■ ACKNOWLEDGMENTS

The authors appreciate the support of the Faculty of Engineering, Virumaa College of Tallinn University of Technology, and are thankful to Stat-Ease, Minneapolis, MN, USA, for providing the Design-Expert 12 Package. The authors acknowledge financial support from European Regional Development Fund projects TK133, TK134, TK141 and Estonian Research Council Grants PRG4 and PRG1023. NMR spectra were acquired on the instrumentation of the Estonian Center of Analytical Chemistry (AKKI, TT4).

## ■ REFERENCES


(1) Toutov, A. A.; Salata, M.; Fedorov, A.; Yang, Y. -F.; Liang, Y.; Cariou, R.; Betz, K. N.; Couzijn, E. P. A.; Shabaker, J. W.; Houk, K. N.; Grubbs, R. H. A potassium tert-butoxide and hydrosilane system for ultra-deep desulfurization of fuels. *Nat. Energy* **2017**, *2* (3), 1−7.

(2) Kang, L.; Liu, H.; He, H.; Yang, C. Oxidative desulfurization of dibenzothiophene using molybdenum catalyst supported on Ti-pillared montmorillonite and separation of sulfones by filtration. *Fuel* **2018**, *234*, 1229−1237.

(3) Muhammad, Y.; Rashid, H. U.; Subhan, S.; Rahman, A. U.; Sahibzada, M.; Tong, Z. Boosting the hydrodesulfurization of dibenzothiophene efficiency of Mn decorated (Co/Ni)-Mo/$Al_2O_3$ catalysts at mild temperature and pressure by coupling with phosphonium based ionic liquids. *Chem. Eng. J.* **2019**, *375*, 121957.

(4) Shafiq, I.; Shafique, S.; Akhter, P.; Yang, W.; Hussain, M. Recent developments in alumina supported hydrodesulfurization catalysts for the production of sulfur-free refinery products: A technical review. *Catal. Rev.: Sci. Eng.* **2022**, *64*, 1−86.

(5) Rajendran, A.; Cui, T. Y.; Fan, H. X.; Yang, Z. F.; Feng, J.; Li, W. Y. A comprehensive review on oxidative desulfurization catalysts targeting clean energy and environment. *J. Mater. Chem. A* **2020**, *8* (5), 2246−2285.

(6) Gu, Q.; Wen, G.; Ding, Y.; Wu, K. H.; Chen, C.; Su, D. Reduced graphene oxide: a metal-free catalyst for aerobic oxidative desulfurization. *Green Chem.* **2017**, *19* (4), 1175−1181.

(7) Bagheri, M.; Yaser Masoomi, M.; Morsali, A. A MoO 3 −Metal−Organic Framework Composite as a Simultaneous Photocatalyst and Catalyst in the PODS Process of Light Oil. *ACS Catal.* **2017**, *7* (10), 6949−6956.

(8) Zhu, W.; Huang, W.; Li, H.; Zhang, M.; Jiang, W.; Chen, G.; Han, C. Polyoxometalate-based ionic liquids as catalysts for deep desulfurization of fuels. *Fuel Process. Technol.* **2011**, *92* (10), 1842−1848.

(9) Yu, X.; Han, P.; Li, Y. Oxidative desulfurization of dibenzothiophene catalyzed by $\alpha$-$MnO_2$ nanosheets on palygorskite using hydrogen peroxide as oxidant. *RSC Adv.* **2018**, *8* (32), 17938−17943.


Downloaded from pubs.acs.org/acsodf/article-pdf/9/22/23329/4417267/ac3c09971.pdf by TALLINN TECHNICAL UNIV user on 25 September 2026

(10) Gao, Y.; Gao, R.; Zhang, G.; Zheng, Y.; Zhao, J. Oxidative desulfurization of model fuel in the presence of molecular oxygen over polyoxometalate based catalysts supported on carbon nanotubes. *Fuel* **2018**, *224*, 261−270.
(11) Mokhtar, W. N. A. W.; Bakar, W. A. W. A.; Ali, R.; Kadir, A. A. A. Optimization of oxidative desulfurization of Malaysian Euro II diesel fuel utilizing tert-butyl hydroperoxide−dimethylformamide system. *Fuel* **2015**, *161*, 26−33.
(12) Jiang, X.; Li, H.; Zhu, W.; He, L.; Shu, H.; Lu, J. Deep desulfurization of fuels catalyzed by surfactant-type decatungstates using $H_2O_2$ as oxidant. *Fuel* **2009**, *88* (3), 431−436.
(13) Zheng, H. Q.; Zeng, Y. N.; Chen, J.; Lin, R. G.; Zhuang, W. E.; Cao, R.; Lin, Z. J. Zr-based metal−organic frameworks with intrinsic peroxidase-like activity for ultradeep oxidative desulfurization: mechanism of $H_2O_2$ decomposition. *Inorg. Chem.* **2019**, *58* (10), 6983−6992.
(14) Hao, L.; Hurlock, M. J.; Ding, G.; Zhang, Q. Metal−organic frameworks towards desulfurization of fuels. *Metal-Organic Framework* **2020**, *378*, 175−202.
(15) Leng, K.; Sun, Y.; Zhang, X.; Yu, M.; Xu, W. Ti-modified hierarchical mordenite as highly active catalyst for oxidative desulfurization of dibenzothiophene. *Fuel* **2016**, *174*, 9−16.
(16) Shi, Y.; Liu, G.; Zhang, B.; Zhang, X. Oxidation of refractory sulfur compounds with molecular oxygen over a Ce−Mo−O catalyst. *Green Chem.* **2016**, *18* (19), 5273−5279.
(17) Wu, P.; Zhu, W.; Chao, Y.; Zhang, J.; Zhang, P.; Zhu, H.; Dai, S. A template-free solvent-mediated synthesis of high surface area boron nitride nanosheets for aerobic oxidative desulfurization. *Chem. Commun.* **2016**, *52* (1), 144−147.
(18) Jung, B. K.; Jhung, S. H. Adsorptive removal of benzothiophene from model fuel, using modified activated carbons, in presence of diethylether. *Fuel* **2015**, *145*, 249−255.
(19) Serrano, D. P.; Sanz, R.; Pizarro, P.; Moreno, I.; Medina, S. Hierarchical TS-1 zeolite as an efficient catalyst for oxidative desulphurization of hydrocarbon fractions. *Appl. Catal., B* **2014**, *146*, 35−42.
(20) Piscopo, C. G.; Granadeiro, C. M.; Balula, S. S.; Bošković, D. Metal-Organic Framework-Based Catalysts for Oxidative Desulfurization. *Chem. Catal. Chem.* **2020**, *12* (19), 4721−4731.
(21) Bhadra, B. N.; Jhung, S. H. Oxidative desulfurization and denitrogenation of fuels using metal-organic framework-based/-derived catalysts. *Appl. Catal., B* **2019**, *259*, 118021.
(22) Smolders, S.; Willhammar, T.; Krajnc, A.; Sentosun, K.; Wharmby, M. T.; Lomachenko, K. A.; Bals, S.; Mali, G.; Roeffaers, M. B. J.; De Vos, D. E.; Bueken, B. A Titanium(IV)-Based Metal−Organic Framework Featuring Defect-Rich Ti-O Sheets as an Oxidative Desulfurization Catalyst. *Angew. Chem.* **2019**, *131* (27), 9258−9263.
(23) Ye, G.; Qi, H.; Li, X.; Leng, K.; Sun, Y.; Xu, W. Enhancement of oxidative desulfurization performance over UiO-66 (Zr) by titanium ion exchange. *Chem. Phys. Chem.* **2017**, *18* (14), 1903−1908.
(24) Zhang, X.; Huang, P.; Liu, A.; Zhu, M. A metal−organic framework for oxidative desulfurization: UiO-66 (Zr) as a catalyst. *Fuel* **2017**, *209*, 417−423.
(25) Viana, A. M.; Ribeiro, S. O.; Castro, B. D.; Balula, S. S.; Cunha-Silva, L. Influence of UiO-66 (Zr) preparation strategies in its catalytic efficiency for desulfurization process. *Materials* **2019**, *12* (18), 3009.
(26) Zhang, X. F.; Wang, Z.; Feng, Y.; Zhong, Y.; Liao, J.; Wang, Y.; Yao, J. Adsorptive desulfurization from the model fuels by functionalized UiO-66 (Zr). *Fuel* **2018**, *234*, 256−262.
(27) Liao, X.; Wang, X.; Wang, F.; Yao, Y.; Lu, S. Ligand Modified Metal Organic Framework UiO-66: A Highly Efficient and Stable Catalyst for Oxidative Desulfurization. *J. Inorg. Organomet. Polym. Mater.* **2021**, *31* (2), 756−762.
(28) Ye, G.; Qi, H.; Zhou, W.; Xu, W.; Sun, Y. Green and scalable synthesis of nitro-and amino-functionalized UiO-66 (Zr) and the effect of functional groups on the oxidative desulfurization performance. *Inorg. Chem. Front.* **2019**, *6* (5), 1267−1274.
(29) Ahmed, I.; Jhung, S. H. Effective adsorptive removal of indole from model fuel using a metal-organic framework functionalized with amino groups. *J. Hazard. Mater.* **2015**, *283*, 544−550.
(30) Barghi, B.; Jürisoo, M.; Volokhova, M.; Seinberg, L.; Reile, I.; Mikli, V.; Niidu, A. Process Optimization for Catalytic Oxidation of Dibenzothiophene over UiO-66-$NH_2$ by Using a Response Surface Methodology. *ACS Omega* **2022**, *7* (19), 16288−16297.
(31) Granadeiro, C. M.; Ribeiro, S. O.; Karmaoui, M.; Valença, R.; Ribeiro, J. C.; de Castro, B.; Cunha-Silva, L.; Balula, S. S. Production of ultra-deep sulfur-free diesels using a sustainable catalytic system based on UiO-66 (Zr). *Chem. Commun.* **2015**, *51* (72), 13818−13821.
(32) Ye, G.; Zhang, D.; Li, X.; Leng, K.; Zhang, W.; Ma, J.; Sun, Y.; Xu, W.; Ma, S. Boosting Catalytic Performance of Metal−Organic Framework by Increasing the Defects via a Facile and Green Approach. *ACS Appl. Mater. Interfaces* **2017**, *9* (40), 34937−34943.
(33) Wu, J.; Gao, Y.; Zhang, W.; Tan, Y.; Tang, A.; Men, Y.; Tang, B. Deep desulfurization by oxidation using an active ionic liquid-supported Zr metal−organic framework as catalyst. *Appl. Organomet. Chem.* **2015**, *29* (2), 96−100.
(34) Viana, A. M.; Julião, D.; Mirante, F.; Faria, R. G.; de Castro, B.; Balula, S. S.; Cunha-Silva, L. Straightforward activation of metal-organic framework UiO-66 for oxidative desulfurization processes. *Catal. Today* **2021**, *362*, 28−34.
(35) Hao, L.; Stoian, S. A.; Weddle, L. R.; Zhang, Q. Zr-Based MOFs for oxidative desulfurization: what matters? *Green Chem.* **2020**, *22* (19), 6351−6356.
(36) Katz, M. J.; Brown, Z. J.; Colón, Y. J.; Siu, P. W.; Scheidt, K. A.; Snurr, R. Q.; Hupp, J. T.; Farha, O. K. A facile synthesis of UiO-66, UiO-67 and their derivatives. *Chem. Commun.* **2013**, *49* (82), 9449−9451.
(37) Barghi, B.; Niidu, A.; Karimzadeh, R. The effect of water and zinc loading on LPG catalytic cracking for light olefin production using Response Surface Methodology. *Proc. Est. Acad. Sci.* **2021**, *70* (2), 135−147.
(38) Bezerra, M. A.; Santelli, R. E.; Oliveira, E. P.; Villar, L. S.; Escaleira, L. A. Response surface methodology (RSM) as a tool for optimization in analytical chemistry. *Talanta* **2008**, *76* (5), 965−977.
(39) Cavka, J. H.; Jakobsen, S.; Olsbye, U.; Guillou, N.; Lamberti, C.; Bordiga, S.; Lillerud, K. P. A new zirconium inorganic building brick forming metal organic frameworks with exceptional stability. *J. Am. Chem. Soc.* **2008**, *130* (42), 13850−13851.
(40) Vermoortele, F.; Vandichel, M.; Van de Voorde, B.; Ameloot, R.; Waroquier, M.; Van Speybroeck, V.; De Vos, D. E. Electronic effects of linker substitution on Lewis acid catalysis with metal−organic frameworks. Angew. *Angew. Chem., Int. Ed.* **2012**, *51* (20), 4887−4890.
(41) Vo, T. K.; Le, V.N.; Nguyen, V.C.; Song, M.; Kim, D.; Yoo, K. S.; Park, B. J.; Kim, J. Microwave-assisted continuous-flow synthesis of mixed-ligand UiO-66 (Zr) frameworks and their application to toluene adsorption. *J. Ind. Eng. Chem.* **2020**, *86*, 178−185.
(42) Kim, J. Y.; Kang, J.; Cha, S.; Kim, H.; Kim, D.; Kang, H.; Choi, I.; Kim, M.; et al. Stability of Zr-Based UiO-66 Metal−Organic Frameworks in Basic Solutions. *Nanomater* **2024**, *14* (1), 110.
(43) Yang, Q.; Zhang, H. Y.; Wang, L.; Zhang, Y.; Zhao, J. Ru/UiO-66 catalyst for the reduction of nitroarenes and tandem reaction of alcohol oxidation/Knoevenagel condensation. *ACS Omega* **2018**, *3* (4), 4199−4212.
(44) Abbaslou, R. M. M.; Tavassoli, A.; Soltan, J.; Dalai, A. K. Iron catalysts supported on carbon nanotubes for Fischer−Tropsch synthesis: Effect of catalytic site position. *Appl. Catal., A* **2009**, *367* (1−2), 47−52.
(45) Akbari, A.; Omidkhah, M.; Towfighi, D. J. Optimization of operating conditions in oxidation of dibenzothiophene in the light hydrocarbon model. *Chem. Ind. Chem. Eng. Q* **2014**, *20* (3), 315−323.
(46) Saleh, T. A. Simultaneous adsorptive desulfurization of diesel fuel over bimetallic nanoparticles loaded on activated carbon. *J. Cleaner Prod.* **2018**, *172*, 2123−2132.

Downloaded from pubs.acs.org/acsodf/article-pdf/9/22/23329/4417267/ac3c09971.pdf by TALLINN TECHNICAL UNIV user on 25 September 2026

(47) Fox, B. R.; Brinich, B. L.; Male, J. L.; Hubbard, R. L.; Siddiqui, M. N.; Saleh, T. A.; Tyler, D. R. Enhanced oxidative desulfurization in a film-shear reactor. *Fuel* **2015**, *156*, 142−147.
(48) Kargar, H.; Ghahramaninezhad, M.; Shahrak, M. N.; Balula, S. S. An effective magnetic catalyst for oxidative desulfurization of model and real fuels: $Fe_3O_4$/ZIF-8/$TiO_2$. *Microporous Mesoporous Mater.* **2021**, *317*, 110992.
(49) Li, J.; Yang, Z.; Hu, G.; Zhao, J. Heteropolyacid supported MOF fibers for oxidative desulfurization of fuel. *Chem. Eng. J.* **2020**, *388*, 124325.
(50) Ghahramaninezhad, M.; Pakdel, F.; Shahrak, M. N. Boosting oxidative desulfurization of model fuel by POM-grafting ZIF-8 as a novel and efficient catalyst. *Polyhedron* **2019**, *170*, 364−372.
(51) Wang, X. S.; Li, L.; Liang, J.; Huang, Y. B.; Cao, R. Boosting oxidative desulfurization of model and real gasoline over phosphotungstic acid encapsulated in metal−organic frameworks: the window size matters. *Chem. Catal. Chem.* **2017**, *9* (6), 971−979.
(52) Wei, S.; He, H.; Cheng, Y.; Yang, C.; Zeng, G.; Qiu, L. Performances, kinetics and mechanisms of catalytic oxidative desulfurization from oils. *RSC Adv.* **2016**, *6* (105), 103253−103269.

Downloaded from pubs.acs.org/acsodf/article-pdf/9/22/23329/4417267/ac3c09971.pdf by TALLINN TECHNICAL UNIV user on 25 September 2026



https://doi.org/10.1021/acsomega.3c09971
*ACS Omega* 2024, 9, 23329−23338

**Publication III**

**Barghi, B**., Mõistlik, T., Panov, D., Raag, A., Järvik, O. and Niidu, A., 2025. Kinetic Modeling of Deep Oxidative Desulphurization over Functionalized UiO-66 from a Model Fuel Using Complex Reaction Theory. ACS Omega. 2025, 10 (16), pp. 15947–15958.

ACS OMEGA

Open Access
This article is licensed under CC-BY 4.0
http://pubs.acs.org/journal/acsodf

Article

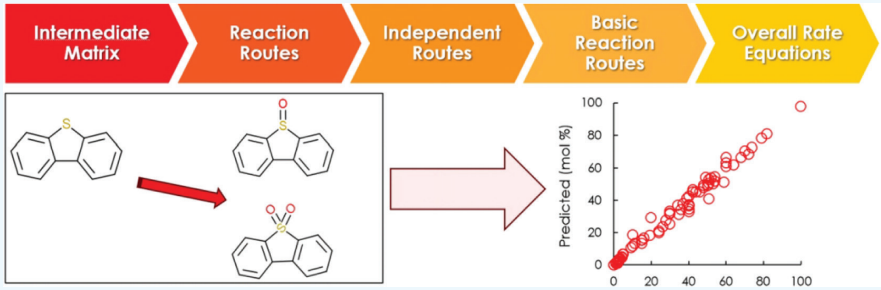
# Kinetic Modeling of Deep Oxidative Desulfurization over Functionalized UiO-66 from a Model Fuel Using Complex Reaction Theory

Bijan Barghi,* Tanel Mõistlik, Deniss Panov, Anastassia Raag, Oliver Järvik, and Allan Niidu

Cite This: *ACS Omega* 2025, 10, 15947−15958

Read Online

ACCESS | Metrics & More | Article Recommendations




**ABSTRACT:** This study proposes a systematic and straightforward approach for determining basic reaction routes and overall reactions using the theory of complex kinetics for an oxidative desulfurization (ODS) reaction using solvothermally synthesized metalorganic framework (MOF), UiO-66-$NO_2$ as a catalyst to remove the dibenzothiophene (DBT) from a model fuel in the temperature range of 20−100 °C. The intermediates are organized in a "matrix of intermediates" that simplifies the elementary reactions combination to form overall reactions. Adsorption, oxidation, and desorption were taken into consideration in 11 basic reaction steps that comprised the suggested ODS mechanism. The model's kinetic parameters were optimized by MATLAB program and described by the reparametrized Arrhenius equation. Markov chain Monte Carlo (MCMC) modeling was used to investigate the dependability of the estimated parameters and model predictions. The experimental results were satisfactorily in agreement with the model predictions, as the complex reaction was utilized for the first time to investigate the ODS reaction over MOFs.

## 1. INTRODUCTION

The growth of the global population, along with advancements in economic activities, has led to a rise in the demand for fossil fuels across multiple sectors. This includes the need for energy inputs in industrial sectors.[1−6] Various fuels, such as diesel and gasoline, which are produced from crude oil, contain different sulfur-containing compounds, such as thiophenes. The combustion of fossil fuels results in the release of sulfur oxides, causing environmentally harmful pollution.[7,8] The hydrodesulfurization process, which uses chromium/molybdenum catalysts, is the conventional technology for removing organic sulfur from liquid fuels; however, as a byproduct, this process produces undesired $H_2S$ gas. Nevertheless, this method is only financially viable when eliminating specific sulfur compounds, such as dibenzothiophene.[9] The approach is not capable of entirely removing aromatic sulfur-containing compounds. To address this issue, alternative methodologies e.g., ODS, selective adsorption,[9,10] and biodesulfurization[11] have been studied. One of the techniques mentioned, ODS, is acknowledged as a green approach for the desulphurization of benzothiophene derivatives.[12] It has gained considerable attention because of its simple and straightforward operating conditions and its positive impact on the economy and the environment.[13]

Metal−organic frameworks (MOFs) have gained significant attention due to their unique properties that could be tailored according to specific needs.[14] These materials consist of metal centers bonded to organic ligands, resulting in a flexible structure with chemical tunability, high specific surface area, and high porosity.[15] Due to their tunability and diverse chemical compositions, MOFs find applications in various fields.[16−21] $ZrO_2$ forms $Zr_6$ clusters ($Zr_6O_4(OH)_4$) composed of six zirconium atoms arranged in an octahedral geometry, which

**Received:** July 21, 2024
**Revised:** March 24, 2025
**Accepted:** April 8, 2025
**Published:** April 15, 2025



ACS Publications

© 2025 The Authors. Published by American Chemical Society



Downloaded from pubs.acs.org/acsodf/article-pdf/10/16/15947/4082097/9/ac4c06722.pdf by TALLINN TECHNICAL UNIV user on 25 September 2026

are interconnected by eight $\mu_3$-oxygen atoms.[22] These clusters can be reversibly reconfigured without breaking connecting oxygen bridges leading to extraordinary robustness of Zr-based MOFs.[22] For instance, UiO-66(Zr) as a zirconium-based MOF, where the hexanuclear zirconium clusters are connected to terephthalic acid ($H_2$BDC) organic linkers,[23,24] exhibits high thermal stability.

Different functional organic linkers in UiO-66 have been reported to offer a strong affinity toward various environmental contaminants and to have the potential to significantly impact chemical activity.[25−27] Nitro-modified UiO-66 (UiO-66-$NO_2$) exhibited high catalytic activity in the deep ODS due to the more electron-accepting group in its ligand structure.[28,29] Recent advancements have led to the development of MOFs with enhanced stability against oxidants like $H_2O_2$ and oxygen, addressing previous concerns with prior MOFs.[30,31] Because of its high effective oxygen content, $H_2O_2$ has been used extensively as an oxidizing agent during oxidative desulfurization producing water, as a byproduct,[32] an environmentally benign compound, making it an oxidant of choice in the current work. The oxidation of dibenzothiophene (DBT) proceeds through two primary stages, first yielding dibenzothiophene sulfoxide (DBTO) and then dibenzothiophene sulfone ($DBTO_2$). DBTO, also known as mono-oxy DBT or sulfoxide, is formed when a single oxygen atom is added to the sulfur atom in the DBT molecule, representing the initial step in the oxidation process. Further oxidation results in $DBTO_2$, or dioxygen DBT, where two oxygen atoms are attached to the sulfur atom, marking the final stage of this oxidation pathway.

It is evident that ODS stands out as a highly promising technique for fuel desulfurization.[9−11] While numerous studies have reported catalytic data on various catalysts in sulfur oxidation reactions, there is a significant scarcity of a proper kinetic study.[33−37] Most studies contained a kinetic modeling with a first-order kinetic study[33−36] and kinetics employing Langmuir−Hinshelwood and Eley−Rideal mechanisms.[37] Complex reaction methodology[38] employs reaction route networks to construct a kinetic approach for the mechanisms through an intermediate matrix.[3,4] The intermediate matrix represents the stoichiometric relationships between chemical species and elementary reactions.[38] ODS illustrates a reaction network including multiple reactions, which made it necessary to develop a practical procedure for calculating the rate of complex multistep reactions. Previous studies discussed the kinetics of the ODS; however, oxidation products were not reported.[39,40] The theory of complex reactions allows for a more detailed understanding of multistep reaction mechanisms rather than relying solely on the concept of a single rate-determining step. The idea of a rate-determining step (RDS) procedure is not suitable for the reactions with multiple steps, reported before the ODS case.[41] Instead of focusing on a single RDS that can oversimplify complex mechanisms, complex reaction theory considers the interplay between different steps and how they contribute to the overall reaction rate. Researchers have invested significant effort in developing a systematic approach to address complex reaction networks. When reaction mechanisms are described, stoichiometric relationships between the chemical species involved are essential, particularly in complex reactions. Horiuti and Nakamura[42] formulated the comprehensive theory of stoichiometric numbers for elementary reactions, proposing the concept of overall reactions. Following that, Horiuti and Nakamura[43] and Temkin[44] introduced the theory of complex reactions, which facilitated the development of a kinetic model for multiple mechanisms,[45] particularly on the catalyst surface, as it provided an efficient algorithm for estimating the rates of complex multistep reactions. In such procedures that Murzin reported, a singular rate-limiting step may be absent, and the prevalent practice of incorporating such stages primarily results from the convenience of using simpler expressions.[46] Markov chain Monte Carlo (MCMC) method is employed to model the kinetics of reactions accompanied by parameters.[47] MCMC provides a complete picture of parameter uncertainties and their dependencies, which is a core aspect of Bayesian inference. This methodology is applicable for the case with chemical kinetics models that are typically described by systems of differential equations representing reaction rates and species concentrations, in various kinetic study cases, cell culture process in a bioreactor,[47] isobutane dehydrogenation,[48] catalytic oxidation,[49] and lactose hydrogenation over ruthenium.[50]

Previously, to the best of our knowledge, no report has been presented describing a straightforward mathematical procedure for ODS to obtain the overall rate reaction of a standard reactant/product involved in the elementary steps based on the theory of complex reactions. The aim of this study is to create a comprehensive kinetic model using the complex reaction methodology to analyze the ODS mechanism. The dependability of the estimated parameters and model predictions is investigated by the application of Markov chain Monte Carlo (MCMC) techniques.

## 2. EXPERIMENTAL SECTION

**2.1. Materials.** Zirconium(IV) chloride ($ZrCl_4$, 98%, Acros), nitroterephthalic acid (99%, Acros), hydrochloric acid (HCl, 36%, Honeywell), *N*,*N*-dimethylformamide (DMF, 99.5%, Fisher), ethanol ($C_2H_5OH$, 99.9%, Honeywell), acetonitrile (99.9%, Honeywell), n-dodecane (99%, Alfa Aesar), hydrogen peroxide ($H_2O_2$, 30%, Alfa Aesar), and dibenzothiophene (98%, Acros) were used without any further purification.

**2.2. Synthesis of MOF.** MOFs were synthesized as originally described.[51] 1 g of $ZrCl_4$ and 1.25 g of nitro terephthalic acid were dissolved in 120 mL of DMF and 8 mL of 36% and then sonicated for 35 min. In an oven, the prepared solution was heated at 80 °C for 24 h. Upon cooling to room temperature, the sample was washed using DMF and ethanol and dried by heating under 600 mbar pressure at 80 °C on a rotary evaporator. The characterization of the synthesized UiO-66-$NO_2$ MOF was previously reported.[52]

**2.3. Oxidative Desulfurization Test.** ODS reactions were conducted in a 22 mL glass vial reactor. For the model fuel (MF), 1000 ppm of DBT was dissolved in n-dodecane (3 mL). To this solution in the reactor, acetonitrile (3 mL) was added as the polar phase in a 1:1 ratio by volume (3 mL of MF and 3 mL of acetonitrile). Upon oxidation, the polarity of sulfur-containing compounds is increased, enabling their extraction (DBTO and $DBTO_2$) into acetonitrile as the polar phase. 62 mg of UiO-66-$NO_2$ was added to the reactor; then 13.1 mL of hydrogen peroxide (aq. 30%) was added after heating the reactor to a predefined temperature (at 20, 36, 60, 84, and 100 °C) under atmospheric pressure. The polar and fuel phases were separated after the reaction had completed (60 min) and then analyzed by a Shimadzu QP2010 Plus GC to measure the sulfur compounds. The DBT conversion, $X_{DBT}$ [mol %], selectivity, $S_i$ [mol %], and product (DBTO and $DBTO_2$) yield, $Y_i$ [mol %], were calculated by the following eqs 13):

Downloaded from pubs.acs.org/acsodf/article-pdf/10/16/15947/4082097/9/ao4c06722.pdf by TALLINN TECHNICAL UNIV user on 25 September 2026


https://doi.org/10.1021/acsomega.4c06722
ACS Omega 2025, 10, 15947−15958

**Table 1. Rate Equations of Elementary Surface Reactions Proposed for ODS**

| Elementary reaction route | Rate equations | Rate constant unit |
|---|---|---|
| (1) | $r_1 = k_1[\mathrm{DBT}][\mathrm{Z}] - k_{-1}[\mathrm{DBTZ}]$ | $k_1 \equiv [\mathrm{m^3.\ mol^{-1}.\ s^{-1}}]$<br>$k_{-1} \equiv [\mathrm{s^{-1}}]$ |
| (2) | $r_2 = k_2[\mathrm{H_2O_2}][\mathrm{Z}] - k_{-2}[\mathrm{H_2O_2Z}]$ | $k_2 \equiv [\mathrm{m^3.\ mol^{-1}.\ s^{-1}}]$<br>$k_{-2} \equiv [\mathrm{s^{-1}}]$ |
| (3) | $r_3 = k_3[\mathrm{DBTZ}][\mathrm{H_2O_2}] - k_{-3}[\mathrm{DBTOZ}][\mathrm{H_2O}]$ | $k_3 \equiv [\mathrm{m^3.\ mol^{-1}.\ s^{-1}}]$<br>$k_{-3} \equiv [\mathrm{m^3.\ mol^{-1}.\ s^{-1}}]$ |
| (4) | $r_4 = k_4[\mathrm{H_2O_2Z}][\mathrm{DBT}] - k_{-4}[\mathrm{DBTOZ}][\mathrm{H_2O}]$ | $k_4 \equiv [\mathrm{m^3.\ mol^{-1}.\ s^{-1}}]$<br>$k_{-4} \equiv [\mathrm{m^3.\ mol^{-1}.\ s^{-1}}]$ |
| (5) | $r_5 = k_5[\mathrm{DBTOZ}][\mathrm{H_2O_2}] - k_{-5}[\mathrm{DBTO_2Z}][\mathrm{H_2O}]$ | $k_5 \equiv [\mathrm{m^3.\ mol^{-1}.\ s^{-1}}]$<br>$k_{-5} \equiv [\mathrm{m^3.\ mol^{-1}.\ s^{-1}}]$ |
| (6) | $r_6 = k_6[\mathrm{DBTOZ}][\mathrm{H_2O_2}] - k_{-6}[\mathrm{DBTO_2Z}][\mathrm{H_2O}]$ | $k_6 \equiv [\mathrm{m^3.\ mol^{-1}.\ s^{-1}}]$<br>$k_{-6} \equiv [\mathrm{m^3.\ mol^{-1}.\ s^{-1}}]$ |
| (7) | $r_7 = k_7[\mathrm{DBTOZ}][\mathrm{H_2O_2Z}] - k_{-7}[\mathrm{DBTO_2Z}][\mathrm{H_2OZ}]$ | $k_7 \equiv [\mathrm{m^3.\ mol^{-1}.\ s^{-1}}]$<br>$k_{-7} \equiv [\mathrm{m^3.\ mol^{-1}.\ s^{-1}}]$ |
| (8) | $r_8 = k_8[\mathrm{DBTZ}][\mathrm{H_2O_2Z}] - k_{-8}[\mathrm{DBTOZ}][\mathrm{H_2OZ}]$ | $k_8 \equiv [\mathrm{m^3.\ mol^{-1}.\ s^{-1}}]$<br>$k_{-8} \equiv [\mathrm{m^3.\ mol^{-1}.\ s^{-1}}]$ |
| (9) | $r_9 = k_9[\mathrm{DBTO_2Z}] - k_{-9}[\mathrm{DBTO_2}][\mathrm{Z}]$ | $k_9 \equiv [\mathrm{s^{-1}}]$<br>$k_{-9} \equiv [\mathrm{m^3.\ mol^{-1}.\ s^{-1}}]$ |
| (10) | $r_{10} = k_{10}[\mathrm{DBTOZ}] - k_{-10}[\mathrm{DBTO}][\mathrm{Z}]$ | $k_{10} \equiv [\mathrm{s^{-1}}]$<br>$k_{-10} \equiv [\mathrm{m^3.\ mol^{-1}.\ s^{-1}}]$ |
| (11) | $r_{11} = k_{11}[\mathrm{H_2OZ}] - k_{-11}[\mathrm{H_2O}][\mathrm{Z}]$ | $k_{11} \equiv [\mathrm{s^{-1}}]$<br>$k_{-11} \equiv [\mathrm{m^3.\ mol^{-1}.\ s^{-1}}]$ |

$$X_{\mathrm{DBT}}(\%) = (C_0 - C_t)/C_0 \times 100 \quad (1)$$

$$S_i(\%) = M_i/(C_0 - C_t) \times 100 \quad (2)$$

$$Y_i(\%) = X_{\mathrm{DBT}}(\%) \times S_i(\%) = M_i/C_0 \times 100 \quad (3)$$

$C_0$ [mol.m$^{-3}$] and $C_t$ [mol.m$^{-3}$] correspond to the DBT concentration in MF at the beginning and end of the reaction, respectively, and $M_i$ [mol.m$^{-3}$] denotes the concentration of component $i$.

**2.4. Kinetic Study.** The ODS mechanism was presented, along with the number of monomolecular and bimolecular reactions. The product stream constitutes of water, mono-oxy DBT (DBTO or sulfoxide), dioxygen DBT ($DBTO_2$ or sulfone), and DBT. The proposed ODS mechanism of DBT over MOF involves 11 elementary steps illustrating the production of primary sulfone (dioxygen sulfur) and sulfoxide (mono-oxy sulfur) in subsequent reaction stages:

Adsorption of the reactant and oxidant:

$$\mathrm{DBT} + \mathrm{Z} \underset{k_{-1}}{\overset{k_1}{\rightleftarrows}} \mathrm{DBTZ} \quad (4)$$

$$\mathrm{H_2O_2} + \mathrm{Z} \underset{k_{-2}}{\overset{k_2}{\rightleftarrows}} \mathrm{H_2O_2Z} \quad (5)$$

Surface reactions:

$$\mathrm{DBTZ} + \mathrm{H_2O_2} \underset{k_{-3}}{\overset{k_3}{\rightleftarrows}} \mathrm{DBTOZ} + \mathrm{H_2O} \quad (6)$$

$$\mathrm{H_2O_2Z} + \mathrm{DBT} \underset{k_{-4}}{\overset{k_4}{\rightleftarrows}} \mathrm{DBTOZ} + \mathrm{H_2O} \quad (7)$$

$$\mathrm{DBTOZ} + \mathrm{H_2O_2} \underset{k_{-5}}{\overset{k_5}{\rightleftarrows}} \mathrm{DBTO_2Z} + \mathrm{H_2O} \quad (8)$$

$$\mathrm{DBTO} + \mathrm{H_2O_2Z} \underset{k_{-6}}{\overset{k_6}{\rightleftarrows}} \mathrm{DBTO_2Z} + \mathrm{H_2O} \quad (9)$$

$$\mathrm{DBTOZ} + \mathrm{H_2O_2Z} \underset{k_{-7}}{\overset{k_7}{\rightleftarrows}} \mathrm{DBTO_2Z} + \mathrm{H_2OZ} \quad (10)$$

$$\mathrm{DBTZ} + \mathrm{H_2O_2Z} \underset{k_{-8}}{\overset{k_8}{\rightleftarrows}} \mathrm{DBTOZ} + \mathrm{H_2OZ} \quad (11)$$

Desorption:

$$\mathrm{DBTO_2Z} \underset{k_{-9}}{\overset{k_9}{\rightleftarrows}} \mathrm{DBTO_2} + \mathrm{Z} \quad (12)$$

$$\mathrm{DBTOZ} \underset{k_{-10}}{\overset{k_{10}}{\rightleftarrows}} \mathrm{DBTO} + \mathrm{Z} \quad (13)$$

$$\mathrm{H_2OZ} \underset{k_{-11}}{\overset{k_{11}}{\rightleftarrows}} \mathrm{Z} + \mathrm{H_2O} \quad (14)$$

Downloaded from pubs.acs.org/acsodf/article-pdf/10/16/15947/4082079/ao4c06722.pdf by TALLINN TECHNICAL UNIV user on 25 September 2026



https://doi.org/10.1021/acsomega.4c06722
ACS Omega 2025, 10, 15947−15958

**Table 2. Matrix of Surface Species in DBT ODS Reaction Steps**

| Reaction no. | Reactions | Z | DBTZ | DBTOZ | $DBTO_2Z$ | $H_2O_2Z$ | $H_2OZ$ |
|---|---|---|---|---|---|---|---|
| 1 | $DBT + Z \underset{k_{-1}}{\overset{k_1}{\rightleftarrows}} DBTZ$ | −1 | +1 | 0 | 0 | 0 | 0 |
| 2 | $H_2O_2 + Z \underset{k_{-2}}{\overset{k_2}{\rightleftarrows}} H_2O_2Z$ | −1 | 0 | 0 | 0 | +1 | 0 |
| 3 | $DBTZ + H_2O_2 \underset{k_{-3}}{\overset{k_3}{\rightleftarrows}} DBTOZ + H_2O$ | 0 | −1 | +1 | 0 | 0 | 0 |
| 4 | $H_2O_2Z + DBT \underset{k_{-4}}{\overset{k_4}{\rightleftarrows}} DBTOZ + H_2O$ | 0 | 0 | +1 | 0 | −1 | 0 |
| 5 | $DBTOZ + H_2O_2 \underset{k_{-5}}{\overset{k_5}{\rightleftarrows}} DBTO_2Z + H_2O$ | 0 | 0 | −1 | +1 | 0 | 0 |
| 6 | $DBTO + H_2O_2Z \underset{k_{-6}}{\overset{k_6}{\rightleftarrows}} DBTO_2Z + H_2O$ | 0 | 0 | 0 | +1 | −1 | 0 |
| 7 | $DBTOZ + H_2O_2Z \underset{k_{-7}}{\overset{k_7}{\rightleftarrows}} DBTO_2Z + H_2OZ$ | 0 | 0 | −1 | +1 | −1 | +1 |
| 8 | $DBTZ + H_2O_2Z \underset{k_{-8}}{\overset{k_8}{\rightleftarrows}} DBTOZ + H_2OZ$ | 0 | −1 | +1 | 0 | −1 | +1 |
| 9 | $DBTO_2Z \underset{k_{-9}}{\overset{k_9}{\rightleftarrows}} DBTO_2 + Z$ | −1 | 0 | 0 | +1 | 0 | 0 |
| 10 | $DBTOZ \underset{k_{-10}}{\overset{k_{10}}{\rightleftarrows}} DBTO + Z$ | −1 | 0 | +1 | 0 | 0 | 0 |
| 11 | $H_2OZ \underset{k_{-11}}{\overset{k_{11}}{\rightleftarrows}} Z + H_2O$ | −1 | 0 | 0 | 0 | 0 | +1 |

**Table 3. Rearranged Matrix for Elementary Steps of DBT Oxidative Desulfurization**

| Reaction no. | Reactions | Z | DBTZ | DBTOZ | $DBTO_2Z$ | $H_2O_2Z$ | $H_2OZ$ |
|---|---|---|---|---|---|---|---|
| 1 | $DBT + Z \underset{k_{-1}}{\overset{k_1}{\rightleftarrows}} DBTZ$ | −1 | +1 | 0 | 0 | 0 | 0 |
| 10 | $DBTOZ \underset{k_{-10}}{\overset{k_{10}}{\rightleftarrows}} DBTO + Z$ | −1 | 0 | +1 | 0 | 0 | 0 |
| 9 | $DBTO_2Z \underset{k_{-9}}{\overset{k_9}{\rightleftarrows}} DBTO_2 + Z$ | −1 | 0 | 0 | +1 | 0 | 0 |
| 2 | $H_2O_2 + Z \underset{k_{-2}}{\overset{k_2}{\rightleftarrows}} H_2O_2Z$ | −1 | 0 | 0 | 0 | +1 | 0 |
| 11 | $H_2OZ \underset{k_{-11}}{\overset{k_{11}}{\rightleftarrows}} Z + H_2O$ | −1 | 0 | 0 | 0 | 0 | +1 |
| 3 | $DBTZ + H_2O_2 \underset{k_{-3}}{\overset{k_3}{\rightleftarrows}} DBTOZ + H_2O$ | 0 | −1 | +1 | 0 | 0 | 0 |
| 8 | $DBTZ + H_2O_2Z \underset{k_{-8}}{\overset{k_8}{\rightleftarrows}} DBTOZ + H_2OZ$ | 0 | −1 | +1 | 0 | −1 | +1 |
| 5 | $DBTOZ + H_2O_2 \underset{k_{-5}}{\overset{k_5}{\rightleftarrows}} DBTO_2Z + H_2O$ | 0 | 0 | −1 | +1 | 0 | 0 |
| 7 | $DBTOZ + H_2O_2Z \underset{k_{-7}}{\overset{k_7}{\rightleftarrows}} DBTO_2Z + H_2OZ$ | 0 | 0 | −1 | +1 | −1 | +1 |
| 4 | $H_2O_2Z + DBT \underset{k_{-4}}{\overset{k_4}{\rightleftarrows}} DBTOZ + H_2O$ | 0 | 0 | +1 | 0 | −1 | 0 |
| 6 | $DBTO + H_2O_2Z \underset{k_{-6}}{\overset{k_6}{\rightleftarrows}} DBTO_2Z + H_2O$ | 0 | 0 | 0 | +1 | −1 | 0 |

It is noted that Z is the MOF metal node catalytic site, and RZ (R: reactant/products) denote different surface species, also $k_i$ is the intrinsic kinetic constant of elementary step *i*. Table 1 displays 11 surface reactions for the investigation of reaction kinetics. Additionally, Table 2 illustrates the matrix of surface species in the DBT oxidative desulfurization steps. The rate equations were formulated according to the concentration of the reaction participants.

For the extraction oxidation of DBT, an irreversible first-order reaction is considered.[53] The lump kinetic model equations in the final section of the ODS can be obtained by deriving them from the continuity equation and reaction rate equation, assuming:

$$r_{Ex1} = \frac{d[DBTO]}{dt} = k_{ex1}[DBT] \quad (15)$$



https://doi.org/10.1021/acsomega.4c06722
ACS Omega 2025, 10, 15947−15958

Downloaded from pubs.acs.org/acsodf/article-pdf/10/16/15947/4082097/9/ao4c06722.pdf by TALLINN TECHNICAL UNIV user on 25 September 2026

$$r_{Ex2} = \frac{d[DBTO_2]}{dt} = k_{ex2}[DBT] \quad (16)$$

The present study considers the comprehensive scenario of a chemical reaction system, which is explained by a reaction mechanism comprising $\rho$ elementary reaction steps $s_\rho$ ($\rho$ = 1,2,⋯,$p$). The components participating in these elementary reaction steps are categorized into $k$ = 1 to $l$ intermediates, referred to as surface species, labeled as $I_1$, $I_2$, $I_3$, and so forth, and $n$ molecular reactants/products, represented as $T_1$, $T_2$, $T_3$, and so forth. It should be noted that elementary reaction steps can be denoted as follows:[3]

$$s_\rho: \sum_{l}^{k=1} \alpha_{\rho k} I_k + \sum_{n}^{i=1} \beta_{\rho i} T_i (\rho = 1, 2 \ldots p) \quad (17)$$

It is widely acknowledged that the stoichiometric coefficients of the molecular reactants/products $\beta_{\rho i}$ and the intermediates $\alpha_{\rho k}$ possess negative values for reactants and positive values for products. The combination of stages is employed to eliminate the intermediates and achieve the formation of overall reactions. To accomplish this, a procedure is established that relies on the surface species. During the initial phase, the intermediates are collected in a separate matrix called "intermediates matrix".[4] The stoichiometry and intermediate matrix has been proposed as a tool to directly determine the structure of reaction routes in Bray−Liebhafsky reaction,[54] homogeneous organic reaction system,[55] liquified petroleum gas catalytic cracking,[3,4] Prins condensation of isopulegol over zeolite,[56] and the other studies.[38,57−59]

Disregarding the second term within the expression (17) and focusing solely on $\sum_{k=1}^{l} \alpha_{\rho k} I_k$, we can represent the intermediates and their respective stoichiometric coefficients in a three-dimensional matrix referred to as $IM(s_\rho, I_l, \alpha_{\rho l})$. This matrix is structured such that the primary dimension, $s_\rho$, delineates a reaction step or stage $\rho$, the secondary dimension, $I_l$, signifies an intermediate involved in the reaction. Lastly, the third dimension, $\alpha_{\rho l}$, denotes the corresponding stoichiometric coefficient of $I_l$ in the reaction step $s_\rho$. The presence of an intermediate within a particular reaction stage $s_\rho$ is denoted by a value of 1 in the matrix, whereas its absence is represented by a value of 0, also for all molecules (reactant and product molecules, e.g., DBT) the coefficient value is considered zero.

Ultimately, the intermediate matrix (Table 3) undergoes a rearrangement process utilizing the sparse equation solving method due to the prevalent presence of numerous zero elements within the intermediate matrix. The intermediates with higher frequencies are shifted to the former columns and rows. Supposing that the most repeated intermediate (MRI) appears 11 times in the mechanism (surface reaction steps). Consequently, the first column in the table is dedicated to the MRI, and the primary rows represent the stages that involve this intermediate.

Overall reactions are the linear combinations of surface reaction steps produced by multiplying reaction equations of stages by stoichiometric coefficients; these coefficients have to be selected so that there are no surface species in the overall reaction. A reaction route consists of a set of stoichiometric steps and must be unique. However, individual overall reactions can be the same, and it is impossible to derive a single reaction route by multiplying another route by a number. $P$, the number of entire reaction pathways, is ascertained as follows.[3,4]

$$P = S - B + Q \quad (18)$$

The variables $S$, $B$, and $Q$ represent the elementary step number, the number of governing equations between adsorbed intermediates, and the intermediate number, respectively. Six fundamental pathways are anticipated due to the proposed mechanism's 11 steps, six surface species (intermediates), and one equation between adsorbed intermediate (eq 39). At this point, the user identifies the reaction routes on the basis of these routes, as shown in Table 4.

**Table 4. Reaction Routes and Overall Reactions and Basis of Reaction Routes**

| Reaction route | Expression | Overall reaction | |
|---|---|---|---|
| 1 | S1−S3+S10 | DBT + $H_2O_2$ ↔ DBTO + $H_2O$ | $N^{(1)}$ |
| 2 | S9−S5+S10 | DBTO + $H_2O_2$ ↔ $DBTO_2$ + $H_2O$ | $N^{(2)}$ |
| 3 | S4−S9+S10-S6 | DBT + $DBTO_2$ ↔ 2DBTO | $N^{(3)}$ |
| 4 | S3−S5+S7-S8 | - | $N^{(4)}$ |
| 5 | S2+S4+S10 | DBT + $H_2O_2$ ↔ DBTO + $H_2O$ | $N^{(5)}$ |
| 6 | S11+S7−S5+S2 | - | $N^{(6)}$ |

The basic routes were used to derive the stoichiometric matrix of reaction routes, $n$, given in Table 5.

**Table 5. Stoichiometric Matrix of Reaction Routes**

| No. | $N^{(1)}$ | $N^{(2)}$ | $N^{(3)}$ | $N^{(4)}$ | $N^{(5)}$ | $N^{(6)}$ |
|---|---|---|---|---|---|---|
| 1 | +1 | 0 | 0 | 0 | 0 | 0 |
| 2 | 0 | 0 | 0 | 0 | +1 | +1 |
| 3 | −1 | 0 | 0 | +1 | 0 | 0 |
| 4 | 0 | 0 | +1 | 0 | +1 | 0 |
| 5 | 0 | −1 | 0 | −1 | 0 | −1 |
| 6 | 0 | 0 | −1 | 0 | 0 | 0 |
| 7 | 0 | 0 | 0 | +1 | 0 | +1 |
| 8 | 0 | 0 | 0 | −1 | 0 | 0 |
| 9 | 0 | +1 | −1 | 0 | 0 | 0 |
| 10 | +1 | +1 | +1 | 0 | +1 | 0 |
| 11 | 0 | 0 | 0 | 0 | 0 | +1 |

The concentration of an intermediate remains constant over time due to the equilibrium between the rates of formation and consumption in different elementary reactions. Each pathway can be expressed as a linear combination of its basic routes. The rate for basic route $N^{(P)}$ (as shown in Table 5) is considered $r^{(P)}$, according to its definition, there are $\vartheta_s^{(P)} r_s^{(P)}$ runs of the $S^{th}$ stage. $\vartheta_s^{(P)}$ is the stoichiometric number of the $S^{th}$ step along the route $N^{(P)}$, $r_s$ and $r_{-s}$ are the rates of the forward and reverse elementary reactions comprising the "$S$" stage. The total number of runs of $S^{th}$ is obtained by summation over all "$P$" basic routes (eq 18). The relationship between the rate of elementary steps and the reaction routes was explained as $\sum_{p=1}^{P} \vartheta_s^{(p)} r_s^{(p)} = r_{|s|} = r_s - r_{-s}$:

$$r_1 = r^{(1)} \quad (19)$$

$$r_2 = r^{(5)} + r^{(6)} \quad (20)$$

$$r_3 = -r^{(1)} + r^{(4)} \quad (21)$$



https://doi.org/10.1021/acsomega.4c06722
ACS Omega 2025, 10, 15947−15958

Downloaded from pubs.acs.org/acsodf/article-pdf/10/16/15947/4082079/ao4c06722.pdf by TALLINN TECHNICAL UNIV user on 25 September 2026

$$r_4 = r^{(3)} + r^{(5)} \quad (22)$$

$$r_5 = -r^{(2)} - r^{(4)} - r^{(6)} \quad (23)$$

$$r_6 = -r^{(3)} \quad (24)$$

$$r_7 = r^{(4)} + r^{(6)} \quad (25)$$

$$r_8 = -r^{(4)} \quad (26)$$

$$r_9 = r^{(2)} - r^{(3)} \quad (27)$$

$$r_{10} = r^{(1)} + r^{(2)} + r^{(3)} + r^{(5)} \quad (28)$$

$$r_{11} = r^{(6)} \quad (29)$$

A quasi-steady-state governing system is thought to exist for this set of reactions. The following relations will be present in the system of equations that the stoichiometric matrix generates:

$$r_7 + r_8 - r_{11} = 0 \quad (30)$$

$$r_1 + r_3 + r_8 = 0 \quad (31)$$

$$r_2 - r_{11} - r_4 - r_6 = 0 \quad (32)$$

$$r_5 + r_9 + r_{11} - r_8 - r_6 = 0 \quad (33)$$

$$r_{10} - r_4 - r_1 + r_5 - r_8 + r_{11} = 0 \quad (34)$$

By providing the individual rates of reaction steps following the mass action law, we can derive the following mathematical eq 3539 and balance eq 40:

$$k_7[\mathrm{DBTOZ}][\mathrm{H_2O_2Z}] - k_{-7}[\mathrm{DBTO_2Z}][\mathrm{H_2OZ}] + k_8[\mathrm{DBTZ}][\mathrm{H_2O_2Z}] - k_{-8}[\mathrm{DTOZ}][\mathrm{H_2OZ}] - k_{11}[\mathrm{H_2OZ}] + k_{-11}[\mathrm{Z}][\mathrm{H_2O}] = 0 \quad (35)$$

$$k_1[\mathrm{DBT}][\mathrm{Z}] - k_{-1}[\mathrm{DBTZ}] + k_3[\mathrm{DBTZ}][\mathrm{H_2O_2}] - k_{-3}[\mathrm{DBTOZ}][\mathrm{H_2O}] + k_8[\mathrm{DBTZ}][\mathrm{H_2O_2Z}] - k_{-8}[\mathrm{DBTOZ}][\mathrm{H_2OZ}] = 0 \quad (36)$$

$$k_2[\mathrm{H_2O_2}][\mathrm{Z}] - k_{-2}[\mathrm{H_2O_2Z}] - k_{11}[\mathrm{H_2OZ}] + k_{-11}[\mathrm{Z}][\mathrm{H_2O}] - k_4[\mathrm{H_2O_2Z}][\mathrm{DBT}] + k_{-4}[\mathrm{DBTOZ}][\mathrm{H_2O}] - k_6[\mathrm{DBTO}][\mathrm{H_2O_2Z}] + k_{-6}[\mathrm{DBTO_2Z}][\mathrm{H_2O}] = 0 \quad (37)$$

$$k_5[\mathrm{DBTOZ}][\mathrm{H_2O_2}] - k_{-5}[\mathrm{DBTO_2Z}][\mathrm{H_2O}] + k_9[\mathrm{DBTO_2Z}] - k_{-9}[\mathrm{DBTO_2}][\mathrm{Z}] + k_{11}[\mathrm{H_2OZ}] - k_{-11}[\mathrm{Z}][\mathrm{H_2O}] - k_8[\mathrm{DBTZ}][\mathrm{H_2O_2Z}] + k_{-8}[\mathrm{DBTOZ}][\mathrm{H_2OZ}] - k_6[\mathrm{DBTO}][\mathrm{H_2O_2Z}] + k_{-6}[\mathrm{DBTO_2Z}][\mathrm{H_2O}] = 0 \quad (38)$$

$$k_{10}[\mathrm{DBTOZ}] - k_{-10}[\mathrm{Z}][\mathrm{DBTO}] - k_4[\mathrm{H_2O_2Z}][\mathrm{DBT}] + k_{-4}[\mathrm{DBTOZ}][\mathrm{H_2O}] - k_1[\mathrm{DBT}][\mathrm{Z}] + k_{-1}[\mathrm{DBTZ}] + k_5[\mathrm{DBTOZ}][\mathrm{H_2O_2}] - k_{-5}[\mathrm{DBTO_2Z}][\mathrm{H_2O}] - k_8[\mathrm{DBTZ}][\mathrm{H_2O_2Z}] + k_{-8}[\mathrm{DBTOZ}][\mathrm{H_2OZ}] + k_{11}[\mathrm{H_2OZ}] - k_{-11}[\mathrm{Z}][\mathrm{H_2O}] = 0 \quad (39)$$

$$[\mathrm{Z}] + [\mathrm{DBTZ}] + [\mathrm{DBTOZ}] + [\mathrm{DBTO_2Z}] + [\mathrm{H_2O_2Z}] + [\mathrm{H_2OZ}] = C_T \quad (40)$$

eq 40 presents the site balance equation, indicating that the sum of all intermediates and free sites is equal to the total number of sites, $C_T$. At this point, the equations below can be used to derive the relationship between the reaction stages and the formation of compounds involved.

$$r_{\mathrm{DBTS}} = -r_1 - r_{\mathrm{Ex1}} - r_{\mathrm{Ex2}} \quad (41)$$

$$r_{\mathrm{DBTSO}} = r_9 + r_{\mathrm{Ex1}} \quad (42)$$

$$r_{\mathrm{DBTSO_2}} = r_{10} + r_{\mathrm{Ex2}} \quad (43)$$

**2.5. Modeling and Parameter Estimation.** The kinetic study was performed on UiO-66-$NO_2$ using a complex reaction methodology. The kinetic rate parameters were calculated by minimizing the objective function that compares the model predicted values with the experimental data. The determination of kinetic coefficients in heterogeneous catalytic reactions contains the analysis of nonlinear equations to assess the kinetic study. In this study, the governing differential equation for a batch reactor is presented in eq 44:

$$r_j = \frac{dC_i}{dt},\ C\text{: [mol. m}^{-3}\text{]} \quad (44)$$

$j$: DBT, DBTSulfoxide(DBTO), DBTSulfone($DBTO_2$)

The molar production rate of component $j$, denoted as $r_j$, is determined by the rate equations of reaction steps; $C_i$ is the concentration of species $i$. The system eqs (eqs 40, 42, and 43) were solved simultaneously using the ODE45 function in MATLAB programming software to obtain the yields, a function used for solving differential equations. ODE45 is appropriate mainly for solving first-order equations that are time-dependent.[60] The optimum parameter estimation was obtained using the experimental species yield data by minimizing the root-mean-square error (RMSE) for the component yield defined by eq 45.

$$\mathrm{RMSE} = \sqrt{\frac{1}{l}\sum_{i}^{m}\left(\frac{Y_{\mathrm{exp.}} - Y_{\mathrm{model}}}{Y_{\mathrm{exp.}}}\right)^2} \quad (45)$$

Here $l$ is the experimental point numbers, $m$ is the number of experimental points at each temperature setting, and $Y_i$ is the component yield in an experiment and predicted by the model. The optimization process utilized the genetic algorithm toolbox provided by MATLAB. The activation energy and pre-exponential factor of reactions were tracked through the reparameterized Arrhenius equation in terms of kinetic parameters, as follows:[61]

Downloaded from pubs.acs.org/acsodf/article-pdf/10/16/15947/4082097/ao4c06722.pdf by TALLINN TECHNICAL UNIV user on 25 September 2026



https://doi.org/10.1021/acsomega.4c06722
ACS Omega 2025, 10, 15947−15958

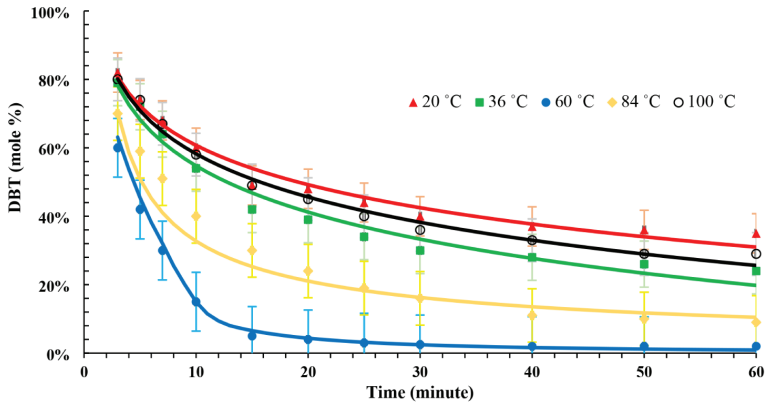



**Figure 1.** DBT (mol %) for the ODS reaction (pressure: atmospheric, temperatures: 20, 36, 60, 84, and 100 °C) "experimental data: dots, predicted results: lines".

**Table 6. Experimental Results and Predicted Model Data of DBT (Mol %) for Oxidative Desulfurization Reaction in Atmospheric Pressure and Different Temperatures**[a]

| | 20° C | | 36° C | | 60° C | | 84° C | | 100° C | |
|---|---|---|---|---|---|---|---|---|---|---|
| Time (min) | Exp. | Pred. | Exp. | Pred. | Exp. | Pred. | Exp. | Pred. | Exp. | Pred. |
| 5 | 74.2% | (72.2 ± 3.0)% | 72.0% | (68.2 ± 3.5)% | 42.1% | (45.4 ± 3.1)% | 59.4% | (50.8 ± 2.7)% | 74.3% | (70.8 ± 2 .1)% |
| 10 | 60.3% | (60.7 ± 2.5)% | 54.1% | (54.7 ± 3.0)% | 15.1% | (15.0 ± 2.5)% | 40.4% | (32.7 ± 2.2)% | 58.2% | (58.2±0.7)% |
| 15 | 49.2% | (54.0 ± 2.3)% | 42.3% | (46.8 ± 2.7)% | 5.2% | (6.6 ± 2.1)% | 30.3% | (25.3 ± 1.9)% | 49.3% | (50.9±0.3)% |
| 20 | 48.0% | (49.2 ± 2.1)% | 39.2% | (41.2 ± 2.4)% | 4.3% | (4.4 ± 1.9)% | 24.6% | (21.1 ± 1.7)% | 45.1% | (45.6±0.2)% |
| 25 | 44.0% | (45.5 ±1.9)% | 34.4% | (36.9 ± 2.2)% | 3.4% | (3.2 ± 1.7)% | 19.1% | (18.3 ± 1.5)% | 40.0% | (41.6±0.2)% |
| 30 | 40.1% | (42.5 ± 1.8)% | 30.6% | (33.3 ± 2.1)% | 2.5% | (2.4 ± 1.5)% | 16.1% | (16.3 ± 1.3)% | 36.2% | (38.2 ±0.1)% |
| 40 | 37.4% | (37.7 ± 1.6)% | 28.1% | (27.7 ± 1.9)% | 2.4% | (1.6 ± 1.3)% | 11.1% | (13.5 ± 1.1)% | 33.1% | (33.0 ±0.1)% |
| 50 | 36.0% | (34.0 ± 1.4)% | 26.0% | (23.3 ± 1.7)% | 2.1% | (1.2 ± 1.1)% | 10.4% | (11.8 ± 0.9)% | 29.3% | (28.9 ± 0.1)% |
| 60 | 35.2% | (31.0 ± 1.3)% | 24.3% | (19.8 ± 1.5)% | 2.0% | (0.9 ± 0.9)% | 9.3% | (10.5 ± 0.8)% | 29.1% | (25.6 ± 0.0)% |

[a]Standard uncertainties ($U$) are $U$ ($T$) = ± 1 °C; $U$ (time) = ± 1 min

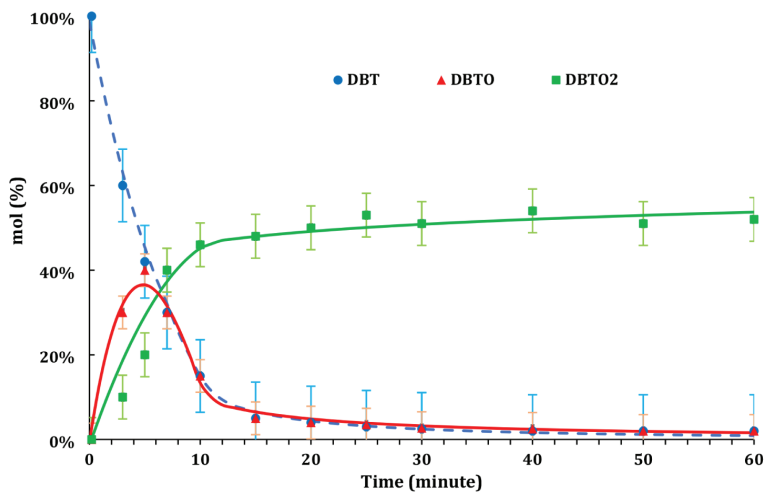



**Figure 2.** Yield (mol %) of DBTO, $DBTO_2$, and DBT mole fraction (mol %) for the ODS reaction (pressure: atmospheric, temperature: 60 °C) "experimental data: dots, predicted results: lines".

Downloaded from pubs.acs.org/acsodf/article-pdf/10/16/15947/4082097/ao4c06722.pdf by TALLINN TECHNICAL UNIV user on 25 September 2026



https://doi.org/10.1021/acsomega.4c06722
ACS Omega 2025, 10, 15947−15958

**Table 7. Experimental Results and Predicted Model Data of DBT, DBTO, and $DBTO_2$ Yield (mol %) Oxidative Desulfurization of the Model Fuel over UiO-66-$NO_2$ at Temperature: 60 °C[a]**

| | DBT | | DBTO | | $DBTO_2$ | |
|---|---|---|---|---|---|---|
| Time | Exp. | Pred. | Exp. | Pred. | Exp. | Pred. |
| 0 | 100% | (98.7 ± 6.3)% | 0 | (0.3 ± 0.0)% | 0 | (1.4 ± 0.1)% |
| 5 | 42.0% | (45.4 ± 4.3)% | 40.0% | (36.5 ± 1.2)% | 20.7% | (29.1 ± 1.4)% |
| 10 | 15.4% | (15.0 ± 1.4)% | 15.3% | (13.4 ± 0.4)% | 46.0% | (45.1 ± 2.2)% |
| 15 | 5.5% | (6.6 ± 0.6)% | 5.0% | (6.5 ± 0.2)% | 48.1% | (48.0 ± 2.4)% |
| 20 | 4.4% | (4.4 ± 0.4)% | 4.3% | (4.9 ± 0.2)% | 50.1% | (49.2 ± 2.4)% |
| 25 | 3.2% | (3.2 ± 0.3)% | 3.5% | (3.9 ± 0.1)% | 53.3% | (50.1 ± 2.5)% |
| 30 | 2.5% | (2.4 ± 0.2)% | 2.7% | (3.2 ± 0.1)% | 51.1% | (50.8 ± 2.5)% |
| 40 | 2.4% | (1.6 ± 0.2)% | 2.5% | (2.4 ± 0.1)% | 54.2% | (52.0 ± 2.6)% |
| 50 | 2.2% | (1.2 ± 0.1)% | 2.3% | (1.9 ± 0.1)% | 51.3% | (52.9 ± 2.6)% |
| 60 | 2.1% | (0.9 ± 0.1)% | 2.0% | (1.6 ± 0.1)% | 52.1% | (53.7 ± 2.6)% |

[a]Standard uncertainties ($U$) are $U$ ($T$) = ± 1 °C; $U$ (time) = ± 1 min

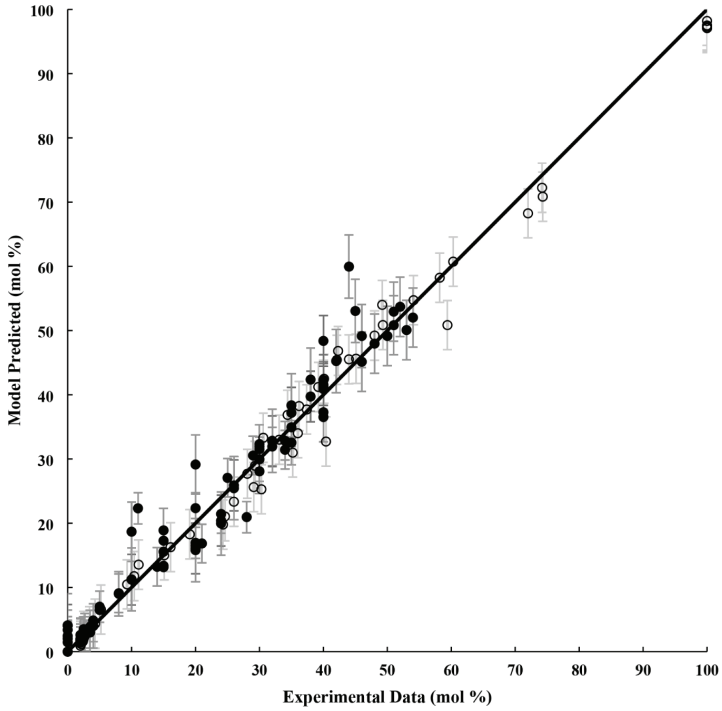



**Figure 3.** Comparison between experimental data and predicted product yields (mol %) "filled circle" and DBT mole fraction (mol %) "unfilled circle" for the ODS at different temperatures 20, 36, 60, 84, 100 °C.

$$k = k_0 \exp\left(-\frac{E}{R}\left(\frac{1}{T} - \frac{1}{T_{ref}}\right)\right), \ln k = \ln k_0 - \left(\frac{E}{R}\left(\frac{1}{T} - \frac{1}{T_{ref}}\right)\right) \quad (46)$$

The reaction rate constant, denoted as $k$, pre-exponential factor, denoted as $k_0$, activation energy $E$ (kJ $mol^{-1}$), denoted as universal gas constant $R$ (kJ $mol^{-1}{\cdot}K^{-1}$), and the reaction temperature, denoted as $T$(K) and $T_{ref}$ (K), 298.15.

## 3. RESULTS AND DISCUSSION

**3.1. Effect of Temperature over ODS.** The reactions were conducted at five temperatures in 1 h. Experimental data and the model predicted DBT mole fraction are demonstrated in Figure 1 and reported in Table 6. The dibenzothiophene oxidation yield is increased by raising the reaction temperature from 20 °C. However, the efficiency of dibenzothiophene oxidation decreases when the temperature exceeds an optimum temperature.[52] Since the oxidative desulfurization reaction is endothermic, raising the temperature promotes the conversion rate of DBT and enhances the molecular mobility of the reaction components. Nevertheless, raising the temperature causes the

Downloaded from pubs.acs.org/acsodf/article-pdf/10/16/15947/4082097/ao4c06722.pdf by TALLINN TECHNICAL UNIV user on 25 September 2026


https://doi.org/10.1021/acsomega.4c06722
ACS Omega 2025, 10, 15947−15958

decomposition of hydrogen peroxide, and therefore, the rate of the ODS reaction decreases as the concentration of the oxidant is reduced.[52]

The component yields obtained from the experiment and the calculations are illustrated in Figure 2. The product distribution results showed that the DBT oxidized to sulfoxide (DBTO) and sulfone ($DBTO_2$) in the presence of UiO-66-$NO_2$. The experimental and kinetic predicted results for the DBT mole fraction and oxidized products yield are reported in Table 7.

A parity plot in Figure 3 demonstrates satisfactory agreement between the experimental and predicted values across the various operating conditions investigated in this study. The optimal kinetic parameters were determined with an RMSE value of 10.5%.

**3.2. Estimation of Kinetic Parameters.** Table 8 presents the results of kinetic optimization, showcasing the activation energy and pre-exponential factor. These results were derived by plotting a linear trendline of $\ln(k_i)$ against $1/T$ $(1/K)$. The slope of the trendline determined the activation energy, and the intercept provided the expression "$\ln(k_0) + \frac{E}{RT_{ref}}$" for the pre-exponential factor "$k_0$" calculation. The results depict that five elementary and one lumped reaction illustrate higher kinetic rates, including DBT adsorption (reaction 1), first DBT oxidation (reaction 3), second DBT oxidation (reaction 5), DBTO desorption (reaction 9), $DBTO_2$ desorption (reaction 10), and $DBTO_2$ extraction to the polar phase (eq 15) which contained three monomolecular reactions, two bimolecular reactions, and one extraction lumped. First, DBT oxidation (reaction step 5) is 1.5 times higher than second DBT oxidation (reaction step 3); also, DBT adsorption is (reaction step 1) 1.8 times higher than second DBT oxidation. Moreover, the DBT adsorption kinetic is greater than $DBTO_2$ desorption. The other stages of reactions were disregarded from the reaction mechanism, while maintaining a high level of precision. It is noted that for the mentioned routes, the reversible reactions were not significant and were ignored. Kinetic parameters were obtained while maintaining the absence of the MOF deactivation.

**Table 8. Optimized Kinetic Parameters, Including Activation Energy and Pre-Exponential Factor for the Proposed Model of DBT Oxidation**

| Item | Unit | Value | Item | Value (kJ mol$^{-1}$) | $R^2$ |
|---|---|---|---|---|---|
| $k_{01}$ | ($m^3.mol^{-1}.s^{-1}$) | $7.48 \times 10^3$ | $E_1$ | 13.1 | 0.954 |
| $k_{02}$ | ($m^3.mol^{-1}.s^{-1}$) | $1.84 \times 10^2$ | $E_2$ | 16.3 | 0.939 |
| $k_{03}$ | ($m^3.mol^{-1}.s^{-1}$) | $7.96 \times 10^2$ | $E_3$ | 15.1 | 0.921 |
| $k_{04}$ | ($m^3.mol^{-1}.s^{-1}$) | $2.53 \times 10^2$ | $E_4$ | 14.3 | 0.993 |
| $k_{05}$ | ($m^3.mol^{-1}.s^{-1}$) | $1.82 \times 10^4$ | $E_5$ | 16.1 | 0.981 |
| $k_{06}$ | ($m^3.mol^{-1}.s^{-1}$) | $3.04 \times 10^2$ | $E_6$ | 20.3 | 0.916 |
| $k_{07}$ | ($m^3.mol^{-1}.s^{-1}$) | $2.08 \times 10^2$ | $E_7$ | 16.9 | 0.947 |
| $k_{08}$ | ($m^3.mol^{-1}.s^{-1}$) | $2.84 \times 10$ | $E_8$ | 12.5 | 0.912 |
| $k_{09}$ | ($s^{-1}$) | $1.48 \times 10^4$ | $E_9$ | 21.4 | 0.939 |
| $k_{010}$ | ($s^{-1}$) | $7.80 \times 10^3$ | $E_{10}$ | 20.1 | 0.930 |
| $k_{011}$ | ($s^{-1}$) | $2.19 \times 10^2$ | $E_{11}$ | 18.5 | 0.951 |
| $k_{0-1}$ | ($s^{-1}$) | $1.10 \times 10$ | $E_{-1}$ | 91.7 | 0.976 |
| $k_{0-2}$ | ($s^{-1}$) | $7.94 \times 10$ | $E_{-2}$ | 92.4 | 0.966 |
| $k_{0-3}$ | ($m^3.mol^{-1}.s^{-1}$) | $5.64 \times 10$ | $E_{-3}$ | 95.3 | 0.955 |
| $k_{0-4}$ | ($m^3.mol^{-1}.s^{-1}$) | $8.42 \times 10^2$ | $E_{-4}$ | 75.3 | 0.965 |
| $k_{0-5}$ | ($m^3.mol^{-1}.s^{-1}$) | 1.82 | $E_{-5}$ | 37.3 | 0.952 |
| $k_{0-6}$ | ($m^3.mol^{-1}.s^{-1}$) | $5.64 \times 10$ | $E_{-6}$ | 89.1 | 0.953 |
| $k_{0-7}$ | ($m^3.mol^{-1}.s^{-1}$) | $3.19 \times 10$ | $E_{-7}$ | 58.7 | 0.963 |
| $k_{0-8}$ | ($m^3.mol^{-1}.s^{-1}$) | 2.91 | $E_{-8}$ | 46.6 | 0.925 |
| $k_{0-9}$ | ($m^3.mol^{-1}.s^{-1}$) | 3.87 | $E_{-9}$ | 55.3 | 0.944 |
| $k_{0-10}$ | ($m^3.mol^{-1}.s^{-1}$) | 3.50 | $E_{-10}$ | 61.7 | 0.938 |
| $k_{0-11}$ | ($m^3.mol^{-1}.s^{-1}$) | 3.74 | $E_{-11}$ | 51.1 | 0.933 |
| $k_{0ex1}$ | ($s^{-1}$) | $1.87 \times 10^3$ | $E_{ex1}$ | 33.7 | 0.929 |
| $k_{0ex2}$ | ($s^{-1}$) | $1.70 \times 10^{-2}$ | $E_{ex2}$ | 31.3 | 0.954 |

**3.3. MCMC Analysis.** The dependability of the six main reaction kinetics was assessed by Markov chain Monte Carlo (MCMC). The findings from the MCMC technique, which employs the Bayesian approach for analysis, are illustrated in Figure 4. The results highlight the existence of potential numerical correlations among the main significant parameters. By considering all uncertainties in the data and the modeling as statistical distributions, the MCMC method offers a means to assess the dependability of the model parameters. The contour plots illustrating the results of parameter estimation show the interrelation between the parameters. The accumulation of the points in each part corresponds to the probability when the circle indicates the regions of the parameter with a 95% probability. The analysis of Figure 4 emphasizes that all parameters are appropriately defined and exhibit no correlation. The presence of well-centered round probability distributions in the projected distributions is proof of this.

## 4. CONCLUSION

Catalytic processes create a complex structure of reaction steps containing reactants, products, and intermediates. One of the complementing strategies proposed to describe the characteristics of complex kinetic networks is the reaction route approach, which provides a more comprehensive framework for understanding multistep reaction mechanisms, moving beyond the limitations of the single rate-determining step (RDS) concept. This approach is particularly valuable for reactions with multiple steps. Rather than simplifying complex mechanisms by focusing on a single RDS, the theory examines the intricate interplay between various steps and their collective impact on the overall reaction rate. Identifying basic reaction routes, and hence the comprehensive rate equation of any reactant/product, is a suitable method for analyzing the reaction pathways. A kinetic study employing complex reaction theory was conducted to investigate the oxidative desulfurization of DBT using UiO-66-$NO_2$ at varying temperatures (20, 36, 60, 84, and 100 °C). Eleven elementary reactions were postulated in this study to describe the rates of formation or consumption of molecular components. In addition, the removal rate of DBT to the polar phase was based on the assumption of two lumped reactions. The kinetic parameters of DBT ODS reactions have been optimized, and the rate constants were determined through utilizing a simultaneous code connection to model the reactor with the MATLAB software. The activation energy and rate coefficients were determined by linear reparametrized Arrhenius plots. DBTO showed higher oxidation rate than DBT oxidation, DBT adsorption kinetic is greater than $DBTO_2$ desorption. Ultimately, this investigation proposed a procedure for the integration of complex theory and multiple reactants, products, and surface step reactions. The model accurately identifies the kinetics of the reactions through the results obtained from parameter estimation. The kinetic parameters were adjusted to minimize error, resulting in an RMSE of 10.5%. All of the model parameters were identified with a 95% probability and were devoid of cross-correlation, according to the MCMC analysis.

Downloaded from pubs.acs.org/acsodf/article-pdf/10/16/15947/4082097/ao4c06722.pdf by TALLINN TECHNICAL UNIV user on 25 September 2026



https://doi.org/10.1021/acsomega.4c06722
ACS Omega 2025, 10, 15947−15958

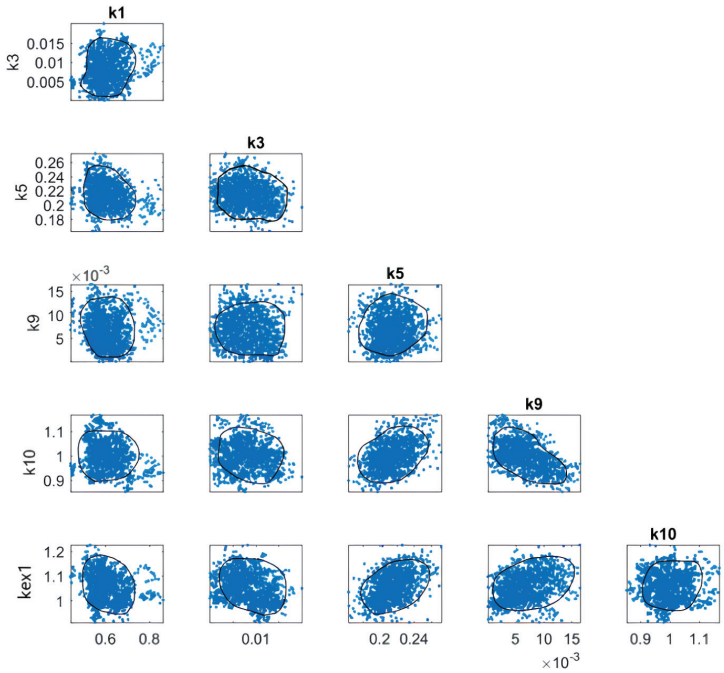



**Figure 4.** Correlation matrix of the parameters using the MCMC method (the density of the dots in each subfigure represents probability, and the circles represent 95% probability regions of the parameter).

## AUTHOR INFORMATION


### Corresponding Author

**Bijan Barghi** − *Virumaa College, School of Engineering, Tallinn University of Technology, Kohtla-Järve 30322, Estonia;* orcid.org/0000-0001-9577-3302; Email: bijan.barghi@taltech.ee

### Authors

**Tanel Mõistlik** − *Virumaa College, School of Engineering, Tallinn University of Technology, Kohtla-Järve 30322, Estonia*

**Deniss Panov** − *Virumaa College, School of Engineering, Tallinn University of Technology, Kohtla-Järve 30322, Estonia*

**Anastassia Raag** − *Virumaa College, School of Engineering, Tallinn University of Technology, Kohtla-Järve 30322, Estonia*

**Oliver Järvik** − *Department of Energy Technology, Tallinn University of Technology, Tallinn 19086, Estonia*

**Allan Niidu** − *Virumaa College, School of Engineering, Tallinn University of Technology, Kohtla-Järve 30322, Estonia;* orcid.org/0000-0003-3406-9869

Complete contact information is available at: https://pubs.acs.org/10.1021/acsomega.4c06722


### Notes

The authors declare no competing financial interest.

## ACKNOWLEDGMENTS

This work was conducted with financial support from the Tallinn University of Technology.

## REFERENCES


(1) Li, S. S.; Li, Y. X.; Jin, M.-M.; Miao, K. J.; Gu, M.-X.; Liu, X.; Sun, L.-B. Controllable fabrication of cuprous sites in confined spaces for efficient adsorptive desulfurization. *Fuel* **2020**, *259*, 116221.

(2) Shafiq, I.; Shafique, S.; Akhter, P.; Yang, W.; Hussain, M. Recent Developments in Alumina Supported Hydrodesulfurization Catalysts for the Production of Ultra-Low Sulfur -free refinery products: A technical review Fuels. *Catal. Rev.* **2022**, *64*, 1.

(3) Barghi, B.; Karimzadeh, R. Kinetic modeling based on complex reaction theory for n-butane catalytic cracking over HZSM-5. *React. Kinet., Mech. Catal.* **2015**, *116*, 507.

(4) Barghi, B.; Karimzadeh, R. Modeling of ZnZSM-5 deactivation during liquefied petroleum gas catalytic cracking in the presence of steam. *React. Kinet., Mech. Catal.* **2017**, *120*, 753.

(5) Barghi, B.; Fattahi, M.; Khorasheh, F. The Modeling of Kinetics and Catalyst Deactivation in Propane Dehydrogenation Over Pt-Sn/$\gamma$-$Al_2O_3$ in Presence of Water as an Oxygenated Additive. *Pet. Sci. Technol.* **2014**, *32*, 1139.

(6) Barghi, B.; Fattahi, M.; Khorasheh, F. Kinetic modeling of propane dehydrogenation over an industrial catalyst in the presence of oxygenated compounds. *React. Kinet., Mech. Catal.* **2012**, *107*, 141.

(7) Liu, Y.; Wang, H.; Zhao, J.; Liu, Y.; Liu, C. Ultra-deep desulfurization by reactive adsorption desulfurization on copper-based catalysts. *J. Energy Chem.* **2019**, *29*, 8.

(8) Rajendran, A.; Cui, T. Y.; Fan, H. X.; Yang, Z. F.; Feng, J.; Li, W. Y. A comprehensive review on oxidative desulfurization catalysts targeting clean energy and environment. *J. Mater. Chem. A* **2020**, *8*, 2246.

(9) Barghi, B.; Jürisoo, M.; Volokhova, M.; Seinberg, L.; Reile, I.; Mikli, V.; Niidu, A. Process Optimization for Catalytic Oxidation of Dibenzothiophene over UiO-66-NH2 by Using a Response Surface Methodology. *ACS Omega* **2022**, *7*, 16288.

(10) Kang, L.; Liu, H.; He, H.; Yang, C. Oxidative desulfurization of dibenzothiophene using molybdenum catalyst supported on Ti-pillared


Downloaded from pubs.acs.org/acsodf/article-pdf/10/16/15947/4082079/ao4c06722.pdf by TALLINN TECHNICAL UNIV user on 25 September 2026

montmorillonite and separation of sulfones by filtration. *Fuel* **2018**, *234*, 1229.
(11) Sadare, O. O.; Daramola, M. O. Bio-catalytic degradation of dibenzothiophene (DBT) in petroleum distillate (diesel) by Pseudomonas spp. *Sci. Re.* **2023**, *13*, 6020.
(12) Miao, G.; Huang, D.; Ren, X.; Li, X.; Li, Z.; Xiao, J. Visible-light induced photocatalytic oxidative desulfurization using $BiVO_4/C_3N_4$@ $SiO_2$ with air/cumene hydroperoxide under ambient conditions. *Appl. Catal., B* **2016**, *192*, 72.
(13) Srivastava, V. C. An evaluation of desulfurization technologies for sulfur removal from liquid fuels. *RSC Adv.* **2012**, *2*, 759.
(14) Chamack, M.; Ifires, M.; Akbar Razavi, S. A.; Morsali, A.; Addad, A.; Larimi, A.; Szunerits, S.; Boukherroub, R. Photocatalytic Performance of Perovskite and Metal−Organic Framework Hybrid Material for the Reduction of N2 to Ammonia. *Inorg. Chem.* **2022**, *61*, 1735.
(15) Jiao, L.; Seow, J. Y. R.; Skinner, W. S.; Wang, Z. U.; Jiang, H. L. Metal−organic frameworks: Structures and functional applications. *Mater. Today* **2019**, *27*, 43.
(16) Sun, Y.; Wang, L.; Amer, W. A.; Yu, H.; Ji, J.; Huang, L.; Shan, J.; Tong, R. Hydrogen Storage in Metal-Organic Frameworks. *J. Inorg. Organomet. Polym. Mater.* **2013**, *23*, 270.
(17) Leelasree, T.; Selamneni, V.; Akshaya, T.; Sahatiya, P.; Aggarwal, H. MOF based flexible, low-cost chemiresistive device as a respiration sensor for sleep apnea diagnosis. *J. Mater. Chem. B* **2020**, *8*, 10182.
(18) Liu, M.; Wu, J.; Hou, H. Metal−Organic Framework (MOF)-Based Materials as Heterogeneous Catalysts for C−H Bond Activation. *Chem.—eur. J.* **2019**, *25*, 2935.
(19) Poonia, K.; Patial, S.; Raizada, P.; Ahamad, T.; Khan, A. A. P.; Le, Q. V.; Nguyen, V.-H.; Hussain, C. M.; Singh, P. Recent advances in Metal Organic Framework (MOF)-based hierarchical composites for water treatment by adsorptional photocatalysis: A review. *Environ. Res.* **2023**, *222*, 115349.
(20) Wu, T.; Prasetya, N.; Li, K. Recent advances in aluminium-based metal-organic frameworks (MOF) and its membrane applications. *J. Membr. Sci.* **2020**, *615*, 118493.
(21) Lawson, H. D.; Walton, S. P.; Chan, C. Metal−Organic Frameworks for Drug Delivery: A Design Perspective. *ACS Appl. Mater. Interfaces* **2021**, *13*, 7004.
(22) Wu, H.; Yildirim, T.; Zhou, W. Exceptional Mechanical Stability of Highly Porous Zirconium Metal−Organic Framework UiO-66 and Its Important Implications. *J. Phys. Chem. Lett.* **2013**, *4*, 925.
(23) Bozbiyik, B.; Duerinck, T.; Lannoeye, J.; De Vos, D. E.; Baron, G. V.; Denayer, J. F. Adsorption and separation of n-hexane and cyclohexane on the UiO-66 metal−organic framework. *Microporous Mesoporous Mater.* **2014**, *183*, 143.
(24) Kandiah, M.; Nilsen, M. H.; Usseglio, S.; Jakobsen, S.; Olsbye, U.; Tilset, M.; Larabi, C.; Quadrelli, E. A.; Bonino, F.; Lillerud, K. P. Synthesis and Stability of Tagged UiO-66 Zr-MOFs. *Chem. Mater.* **2010**, *22*, 6632.
(25) Moghaddam, Z. S.; Kaykhaii, M.; Khajeh, M.; Oveisi, A. R. Synthesis of UiO-66-OH zirconium metal-organic framework and its application for selective extraction and trace determination of thorium in water samples by spectrophotometry. *Spectrochim. Acta, Part A* **2018**, *194*, 76.
(26) Rada, Z. H.; Abid, H. R.; Shang, J.; Sun, H.; He, Y.; Webley, P.; Liu, S.; Wang, S. Functionalized UiO-66 by Single and Binary $(OH)_2$ and $NO_2$ Groups for Uptake of $CO_2$ and $CH_4$. *Ind. Eng. Chem. Res.* **2016**, *55*, 7924.
(27) Li, M.; Liu, X.; Che, Y.; Xing, H.; Sun, F.; Zhou, W.; Zhu, G. Angew. Controlled Partial Linker Thermolysis in Metal-Organic Framework UiO-66-$NH_2$ to Give a Single-Site Copper Photocatalyst for the Functionalization of Terminal Alkynes. *Chem., Int. Ed.* **2023**, *62*, No. e202308651.
(28) Tang, X.; Luo, Y.; Zhang, Z.; Ding, W.; Liu, D.; Wang, J.; Guo, L.; Wen, M. Effects of functional groups of $-NH_2$ and $-NO_2$ on water adsorption ability of Zr-based MOFs (UiO-66). *Chem. Phys.* **2021**, *543*, 111093.
(29) Wang, C.; Jiang, A.; Liu, X.; Koh, K. Y.; Yang, Y.; Chen, J. P.; Li, K. Amorphous metal-organic framework UiO-66-$NO_2$ for removal of oxyanion pollutants: Towards improved performance and effective reusability. *Sep. Purif. Technol.* **2022**, *295*, 121014.
(30) Viana, A. M.; Ribeiro, S. O.; Castro, B. D.; Balula, S. S.; Cunha-Silva, L. Influence of UiO-66(Zr) Preparation Strategies in Its Catalytic Efficiency for Desulfurization Process. *Materials* **2019**, *12* (18), 3009.
(31) Liao, X.; Wang, X.; Wang, F.; Yao, Y.; Lu, S. Ligand Modified Metal Organic Framework UiO-66: A Highly Efficient and Stable Catalyst for Oxidative Desulfurization. *J. Inorg. Organomet. Polym. Mater.* **2021**, *31*, 756.
(32) Jones, C. W. Applications of Hydrogen Peroxide and Derivatives. *RSC Adv.* **1999**, 2.
(33) Safa, M. A.; Bouresli, R.; Al-Majren, R.; Al-Shamary, T.; Ma, X. Oxidative desulfurization kinetics of refractory sulfur compounds in hydrotreated middle distillates. *Fuel* **2019**, *239*, 24.
(34) Kayedi, N.; Samimi, A.; Bajgirani, M. A.; Bozorgian, A. Enhanced oxidative desulfurization of model fuel: A comprehensive experimental study. *S. Afr. J. Chem. Eng.* **2021**, *35*, 153.
(35) De Filippis, P.; Scarsella, M. Oxidative Desulfurization: Oxidation Reactivity of Sulfur Compounds in Different Organic Matrixes. *Energy Fuels* **2003**, *17*, 1452.
(36) Zhao, D.; Sun, Z.; Li, F.; Liu, R.; Shan, H. Oxidative Desulfurization of Thiophene Catalyzed by (C4H9)4NBr·2C6H11NO Coordinated Ionic Liquid. *Energy Fuels* **2008**, *22*, 3065.
(37) Wei, S.; He, H.; Cheng, Y.; Yang, C.; Zeng, G.; Qiu, L. Performances, kinetics and mechanisms of catalytic oxidative desulfurization from oils. *RSC Adv.* **2016**, *6*, 103253.
(38) Murzin, D. Y.; Salmi, T. *Catalytic Kinetics*; Elsevier, 2005. .
(39) Sengupta, A.; Kamble, P. D.; Basu, J. K.; Sengupta, S. Kinetic study and optimization of oxidative desulfurization of benzothiophene using mesoporous titanium silicate-1 catalyst. *Ind. Eng. Chem. Res.* **2012**, *51* (1), 147.
(40) Nawaf, A. T.; Jarullah, A. T.; Gheni, S. A.; Mujtaba, I. M. Development of kinetic and process models for the oxidative desulfurization of light fuel, using experiments and the parameter estimation technique. *Ind. Eng. Chem. Res.* **2015**, *54* (50), 12503.
(41) Dhir, S.; Uppaluri, R.; Purkait, M. K. Oxidative desulfurization: Kinetic modelling. *J. Hazard. Mater.* **2009**, *161* (2−3), 1360.
(42) Horiuti, J.; Nakamura, T. Stoichiometric number and the theory of steady reaction. *J. Phys. Chem.* **1957**, *11* (5), 358.
(43) Horiuti, J.; Nakamura, T. On the theory of heterogeneous catalysis. *Adv. Catal.* **1967**, *17*, 1.
(44) Temkin, M. I. The kinetics of some industrial heterogeneous catalytic reactions. *Adv. Catal.* **1979**, *28*, 173.
(45) Masuda, M. The general theory of stoichiometric number by Juro Horiuti—application to the analysis of the stoichiometries of chemical oscillation systems. *J. Mol. Catal. A: chem.* **2003**, *199*, 175.
(46) Murzin, D. Requiem for the rate-determining step in complex heterogeneous catalytic reactions? *Reactions* **2020**, *1* (1), 37−46.
(47) Xing, Z.; Bishop, N.; Leister, K.; Li, Z. J. Modeling kinetics of a large-scale fed-batch CHO cell culture by Markov chain Monte Carlo method. *Biotechnol. Prog.* **2010**, *26* (1), 208.
(48) Matveyeva, A. N.; Wärnå, J.; Pakhomov, N. A.; Murzin, D. Kinetic modeling of isobutane dehydrogenation over $Ga_2O_3/Al_2O_3$ catalyst. *Chem. Eng. J.* **2020**, *381*, 122741.
(49) Murzin, D. Y.; Saleem, F.; Warnå, J.; Salmi, T. Kinetic modelling of heterogeneous catalytic oxidation of furfural with hydrogen peroxide to succinic acid. *Chem. Eng. J.* **2020**, *382*, 122811.
(50) Doluda, V. Y.; Wärnå, J.; Aho, A.; Bykov, A.; Sidorov, A.; Sulman, E. M.; Bronstein, L. M.; Salmi, T.; Murzin, D. Kinetics of lactose hydrogenation over ruthenium nanoparticles in hypercrosslinked polystyrene. *Ind. Eng. Chem. Res.* **2013**, *52*, 14066.
(51) Katz, M. J.; Brown, Z. J.; Colón, Y. J.; Siu, P. W.; Scheidt, K. A.; Snurr, R. Q.; Hupp, J. T.; Farha, O. K. A facile synthesis of UiO-66, UiO-67 and their derivatives. *Chem. Commun.* **2013**, *49*, 9449.
(52) Barghi, B.; Mõistlik, T.; Raag, A.; Volokhova, M.; Reile, I.; Seinberg, L.; Mikli, V.; Niidu, A. Deep Oxidative Desulfurization of Planar Compounds Over Functionalized Metal−Organic Framework UiO-66(Zr): An Optimization Study. *ACS Omega* **2024**, *9* (22), 23329.

Downloaded from pubs.acs.org/acsodf/article-pdf/10/16/15947/4082097/ao4c06722.pdf by TALLINN TECHNICAL UNIV user on 25 September 2026

(53) Chen, R.; Yu, X.; Ye, X.; Li, J.; Hu, B. Extractive−oxidative desulfurization of model fuels using imidazole-based dicationic ionic liquids as extractants. *React. Chem. Eng.* **2022**, *7*, 877.
(54) Kolar-Anić, L.; Čupić, Ž.; Schmitz, G.; Anić, S. Improvement of the stoichiometric network analysis for determination of instability conditions of complex nonlinear reaction systems. *Chem. Eng. Sc.* **2010**, *65* (12), 3718.
(55) Xing, Y.; Dong, Y.; Zhou, W.; Du, J.; Meng, Q. Optimization-based simultaneous modelling of stoichiometries and kinetics in complex organic reaction system. *Chem. Eng. Sc.* **2023**, *276*, 118758.
(56) Murzin, D. Y. Acid site density as a kinetic descriptor of catalytic reactions over zeolites. *Chem* **2022**, *4* (4), 1609−1623.
(57) Sultan, F.; Shahzad, M.; Ali, M.; Adnan, W.; Khan, W. A. Balancing the chemical equations and their steady-state approximations in the complex reaction mechanism: Linear algebra techniques. *Appl. Nanosci.* **2020**, *10*, 5247.
(58) Toby, S.; Tobias, I. What is the overall stoichiometry of a complex reaction? *J. Chem. Educ.* **2003**, *80* (5), 520.
(59) Fromer, J.; Georgakis, C.; Mustakis, J. Toward the Identification of Stoichiometric Models for Complex Reaction Mixtures. *Ind. Eng. Chem. Res.* **2023**, *62* (5), 2225.
(60) Nehra, V. MATLAB/Simulink based study of different approaches using mathematical model of differential equations. *Int. J. Intell. Syst. Appl.* **2014**, *6* (5), 1.
(61) Schwaab, M.; Pinto, J. C. Optimum reference temperature for reparameterization of the Arrhenius equation. Part 1: Problems involving one kinetic constant. *Chem. Eng. Sci.* **2007**, *62* (10), 2750.

Downloaded from pubs.acs.org/acsodf/article-pdf/10/16/15947/4082097/ao4c06722.pdf by TALLINN TECHNICAL UNIV user on 25 September 2026


https://doi.org/10.1021/acsomega.4c06722
*ACS Omega* 2025, 10, 15947−15958

# Curriculum vitae

**Personal data**

| | |
|---|---|
| Name: | Bijan Barghi |
| Date of birth: | 21-03-1986 |
| Place of birth: | Sirjan, Iran |
| Citizenship: | Iranian |

**Contact data**


| | |
|---|---|
| E-mail: | bijan.barghi@taltech.ee; Bijan.barghi@gmail.com |


**Education**

| | |
|---|---|
| 2020–2026 | Tallinn University of Technology, PhD |
| 2008–2011 | Sharif University of Technology, MSc |
| 2004–2008 | Sharif University of Technology, BSc |

**Language competence**

| | |
|---|---|
| Persian | Native |
| English | Fluent |

## Elulookirjeldus

**Isikuandmed**

| | |
|---|---|
| Nimi: | Bijan Barghi |
| Sünniaeg: | 21-03-1986 |
| Sünnikoht: | Sirjan, Iran |
| Kodakondsus: | Iraanlane |

**Kontaktandmed**

| | |
|---|---|
| E-post: | bibarg@taltech.ee |

**Hariduskäik**

| | |
|---|---|
| 2020–2026 | Tallinna Tehnikaülikool, PhD |
| 2008–2011 | MSc, Sharif University of Technology |
| 2004–2008 | BSc, Sharif University of Technology |

**Keelteoskus**

| | |
|---|---|
| Pärsia keel | Emakeel |
| Inglise keel | Kõrgtase |

ISSN 2585-6901
ISBN 978-9916-80-604-3